Iron Fluoride-Based Positive Electrode Materials for Secondary Batteries Using Ionic Liquid Electrolytes

Yayun Zheng

2022

Table of Contents

Chapter 1 General Introduction 1

1.1 Electrochemical energy storage systems 1

1.2 Lithium and sodium secondary batteries 2

1.3 Positive electrodes 5

1.4 Metal fluoride positive electrodes 9

1.4.1 Binary iron fluorides 9

1.4.2 Iron-based ternary and quaternary fluorides 15

1.5 Aims of this study 17

References 27

Chapter 2 Experimental 40

2.1 Apparatus and material handling 40

2.2 Synthesis of active materials 41

2.3 Characterization techniques 42

2.3.1 X-ray diffraction (XRD) 42

2.3.2 Field emission scanning electron microscopy (SEM) and energy dispersive X-ray spectroscopy (EDX) 43

2.3.3 Specific surface area measurement with Brunauer−Emmett−Teller (BET) method 43

2.3.4 Atomic absorption spectrometry (AAS) and inductively coupled plasma−atomic emission spectrometry (ICP-AES) 43
2.3.5 X-ray absorption fine structure (XAFS) measurement 44
2.3.6 X-ray photoelectron spectroscopy (XPS) 44
2.4 Electrochemical measurements 44
2.4.1 Electrode preparation and cell configurations 44
2.4.2 Galvanostatic charge-discharge test 45
2.4.3 Cyclic voltammetry (CV) and electrochemical impedance spectroscopy (EIS) 46
References 53

Chapter 3 Exploration on the Reaction Mechanism of Trirutile $LiFe_2F_6$ in Li-ion Batteries 54
3.1 Introduction 54
3.2 Experimental 56
3.3 Results and discussion 59
3.4 Conclusions 72
References 86

Chapter 4 Li-storage Mechanism of Rutile $Li_{1.2}MnFe_{1.2}F_{6.8}$ *via* Two Redox Reactions.90
4.1 Introduction 90

4.2 Experimental 92

4.3 Results and discussion 93

4.4 Conclusions 100

References 113

Chapter 5 Structural Evolution of Trirutile-derived FeF_3 during Continuous Sodiation and Desodiation 117

5.1 Introduction 117

5.2 Experimental 118

5.3 Results and discussion 120

5.4 Conclusions 128

References 141

Chapter 6 Phase Transformation of Orthorhombic $NaFeF_3$ in Na-ion Batteries 145

6.1 Introduction 145

6.2 Experimental 146

6.3 Results and discussion 149

6.4 Conclusions 156

References 169

Chapter 7 General Conclusions 173

List of Publications.....177

Acknowledgements 179

Chapter 1

General Introduction

1.1 Electrochemical energy storage systems

The rapid development of global industry promotes the continuous rise of energy demands. Renewable energy sources such as solar, wind, and tidal energy have been developed and applied in some industrial countries. However, these renewable energy sources are intermittent, which greatly limits their application in equipment requiring continuous energy supply. Therefore, the application of energy storage systems (ESSs) plays a vital role in the development of the whole energy field by helping to store those renewable energy sources [1-6].

With the advancement of energy storage technologies, various available ESSs have been developed based on scale and application in the past few decades, such as pumped-storage hydropower, compressed air energy storage, batteries (Li-ion batteries (LIBs), lead-acid batteries, redox flow batteries), and flywheels [7]. It is worth noting that batteries are extensively employed as power sources in a wide range of applications. Among all the different types of batteries, LIBs have emerged as a versatile option covering a wide application range owing to their high energy densities, high coulombic efficiencies, low self-discharge features, and accessibility of diverse electrode designs [8-10].

The commercial production of LIBs began in the 1990s. Sony in Japan launched the first commercial LIBs with the $LiCoO_2$ positive electrode and graphite negative electrode, followed by the development of the compound $LiNiO_2$ as the positive electrode material [8, 10-13]. In 1996, Goodenough *et al*. reported the olivine-type phosphate compound of $LiFePO_4$ as the positive electrode material for LIBs, which has higher safety performance than oxide-based positive electrode materials [14, 15]. In the past two decades, LIBs have become the preferred power supply equipment for various small electronic products (such as laptop computers, smartphones, smartwatches, and digital cameras) [9, 16].

The developments of sodium-ion batteries (SIBs) and LIBs proceeded simultaneously since the 1970s, but the commercial application of SIBs has been almost completely overshadowed by LIBs [12, 17-19]. Nowadays, a huge amount of Li metal required for large-scale applications gives prominence to SIBs as sodium resources are abundant and widely distributed in the earth crust and seawater [19]. Moreover, the similarity of sodium in the chemical properties to lithium, makes its battery application to be one of the most potent alternatives to LIBs for large-scale energy storage applications [19-21].

1.2 Lithium and sodium secondary batteries

Secondary batteries work based on the mutual conversion between chemical and electrical energy [22, 23]. Compared with conventional secondary batteries (such as lead-

acid, nickel-cadmium (Ni-Cd), and nickel-metal hydride (Ni-MH) cells), LIBs and SIBs have distinct advantages including high working voltage, high energy density, and long cycle life [12, 24, 25].

In LIBs and SIBs, the energy is stored through redox reaction based on the reversible insertion/extraction of Li or Na ions to/from active host materials at the specific electrochemical potentials [24, 26]. These types of batteries are also considered to be "rocking-chair" batteries composed of a positive electrode, a negative electrode, a separator, and an electrolyte (the schematic diagram shown in Figure 1-1) [27, 28]. The positive electrode materials are usually transition metal compounds with open frameworks, and Li or Na ions are extracted under the action of an external electric field during the charging process [29, 30]. The negative electrode materials are carbon, carbon-silicon composites, and metal oxides, etc., which are combined with alkali metal ions through an insertion process during charging [31, 32]. On the contrary, Li or Na ions are extracted from the negative electrodes and then inserted into the positive electrodes through the separator during discharging process [28, 29, 32, 33]. The amounts of Li^+ insertion/extraction into/from the electrodes determine the capacity of the corresponding material. In other words, the performance of LIBs and SIBs (i.e., energy density, operation life, safety, and cost) highly depends on the positive and negative electrode materials [20, 34]. Further details on positive electrodes will be discussed in Section 1.3 below.

The electrolytes and the interface between the electrolyte and the electrode materials are also important factors that affect performance of batteries [35-38]. The electrolytes are composed of conductive salt(s) (Li(Na)ClO_4, Li(Na)BF_4, Li(Na)PF_6, etc.) and organic solvent(s) (ethylene carbonate (EC), propylene carbonate (PC), diethylene carbonate (DEC), dimethyl carbonate (DMC), etc.) [30, 38-40]. However, the flammability and volatility of the organic solvents sometimes limit their use in applications that require LIBs and SIBs to operate stably at elevated temperatures [41-43]. In recent years, thermally stable ionic liquids (ILs) have also been examined as electrolytes in LIBs and SIBs owing to their low volatility, low flammability, wide electrochemical windows, wide liquid temperature ranges, and high thermal, chemical, and electrochemical stability [44-48]. In particular, bis(fluorosulfonyl)amide ($[FSA]^-$) anion (Figure 1-2a) is regarded as a "magic anion", and ILs based on $[FSA]^-$ are considered as promising electrolytes for rechargeable battery systems owing to their reasonably high ionic conductivity and ability to form stable solid electrolyte interphases [49-52]. The IL electrolytes based on 1-ethyl-3-methylimidazolium ($[C_2C_1im]^+$) cation (Figure 1-2b) exhibit high ionic conductivity at ambient temperatures which is enhanced at elevated temperatures and are compatible with a variety of electrode materials [38, 53, 54]. The physicochemical and electrochemical properties of the traditional organic electrolytes and IL electrolytes consisting of A[FSA] (A^+ = Li and Na) and $[C_2C_1im]$[FSA] are summarized in Table 1-1.

1.3 Positive electrodes

Up to now, unceasing efforts have been devoted to exploring appropriate positive electrode materials in pursuit of increasing energy density. For example, the developments of layered transition metal oxides, polyanionic compounds, and transition metal fluorides as positive electrodes have brought excellent performance to LIBs and SIBs [16, 55-57]. Insertion-type materials are dominant so far both in practical use and research levels, although some conversion-type materials are also known [34, 58]. The insertion positive materials are classified into several groups including spinel compounds, layered compounds, polyanion-type compounds and so on [55-57]. Table 1-2 summarizes the electrochemical properties of selected positive electrode materials in IL electrolytes.

Spinel-type $LiMn_2O_4$ ($Fd\bar{3}m$) is one of the most representative positive electrode materials for LIBs [59]. In the $LiMn_2O_4$ crystal structure, the Li−O tetrahedra and Mn−O octahedra are coplanar to form an interconnected three-dimensional tunnel structure, which allows Li^+ are freely de-embedded [60]. At present, partially substituted spinel materials $Li[M_xMn_{2-x}]O_4$ (M = Co, Cr, Ni, Fe, etc) have been also developed and widely used as positive electrode materials for LIBs. Lee *et al*. [61] investigated the electrochemical properties of the high-voltage (4.7 V vs. Li/Li^+) $LiNi_{0.5}Mn_{1.5}O_4$ with hollow-structure using 1 mol dm^{-3} Li[FSA]-[C_3C_1pyrr][FSA]. Compared to the commercial organic electrolyte (1 mol dm^{-3} $LiPF_6$/EC:DMC (1:1, v:v)), the advantages of IL electrolytes are highlighted by the superior cycle performance and higher coulombic efficiency of $LiNi_{0.5}Mn_{1.5}O_4$ at an elevated temperature. In addition, an improved rate

capability (106.2 mAh g^{-1} at 5C) was also achieved with the IL electrolyte at 65 °C. These excellent electrochemical properties of spinel $LiNi_{0.5}Mn_{1.5}O_4$ in IL electrolyte were proved to be the result of the formation of a robust, LiF rich cathode-electrolyte interphase (CEI) layer. In SIBs system, the spinel-type compounds containing a larger radius of Na^+ are inactive and structurally unstable. Therefore, there are still no reports on spinel compounds used in SIBs.

For layered compounds, $LiMO_2$ (M = Mn, Co, Ni, etc.) and Na_xMO_2 (M = Mn, Fe, Co, Ni, etc.) were widely studied [18, 62-64]. Their crystal lattices are composed of edge-sharing MO_6 octahedra, which form $(MO_2)_n$ sheets between alkali ions inserted into the octahedral (O), tetrahedral (T) or prismatic (P) environments [65]. At present, $LiNi_{0.5}Mn_{0.5}O_2$ [66, 67], $LiNi_{1-x-y}Co_xMn_yO_2$ ($0 < x, y < 1$) [68], $NaNi_{0.5}Mn_{0.5}O_2$ [69], $NaFe_x(Ni_{0.5}Mn_{0.5})_{1-x}O_2$ [70, 71], and $Na[Ni_{0.32}Fe_{0.13}Co_{0.15}Mn_{0.40}]O_2$ [72] were also developed as the positive electrode materials for secondary ion batteries. Heist *et al*. [73] demonstrated outstanding energy density and cycling stability of the $LiNi_{0.8}Mn_{0.1}Co_{0.1}O_2$ (an average discharge potential of ~ 3.8 V vs. Li/Li^+) with 1.2 mol dm^{-3} Li[FSA]-$[C_3C_1pyrr][FSA]$ IL electrolyte compared to that with the conventional organic electrolyte. This pyrrolidinium-based IL electrolyte is effective to form the stable electrode-electrolyte interfacial layer, thereby protecting the active material from the structural degradation commonly observed in nickel rich cathode. In SIBs, the systematic study on the application of $[FSA]^-$-based IL electrolytes was conducted by employing P2-$Na_{0.6}Ni_{0.22}Al_{0.11}Mn_{0.66}O_2$ as the positive electrode [47]. The half-cell with the

[C_4C_1pyrr][FSA]-based IL electrolyte was superior to other analogs, providing a reversible capacity approaching 140 mAh g^{-1} and a capacity retention of about 100% at 200 cycles.

For polyanion-type compounds, olivine $LiFePO_4$ and $NaFePO_4$ are the most widely studied polyanion inserts hosts [74]. In the case of olivine $NaFePO_4$, there are two polymorphs called triphylite and maricite. The triphylite $NaFePO_4$ belongs to the space group of *Pnma*, which is isostructural to the so-called olivine $LiFePO_4$. The crystal structure of the triphylite $NaFePO_4$ phase contains the corner-sharing FeO_6 octahedra, which are connected to the PO_4 tetrahedron by edge-sharing, thereby resulting in slight distortion in FeO_6 units and leaving 1D pathways for Na^+ diffusion along the *b*-axis. The IL electrolytes of [C_4C_1pyrr][TFSA] containing Na[TFSA] was applied in the electrochemical investigation of the Na/triphylite $NaFePO_4$ half-cell, which delivered optimal performance with respect to the reversible capacity, rate performance, and cyclability at 50 °C [75]. Maricite $NaFePO_4$ is built from edge-sharing FeO_6 octahedra, which are abridged to PO_4 tetrahedra by corner-sharing, leaving no channels for Na^+ migration [3]. Therefore, maricite-type $NaFePO_4$ had been regarded as an electrochemically inactive electrode for SIBs. This general perception was broken by the report of the nano-sized maricite $NaFePO_4$ [76] and the investigation of the crystalline maricite $NaFePO_4$ in IL electrolyte [77]. Moreover, NASICON-type $Li_3Fe_2(PO_4)_3$ [78], $Na_3Fe_2(PO_4)_3$ [79], $Na_3V_2(PO_4)_3$ [80], and pyrophosphate $Li_2FeP_2O_7$ [81] have also been widely investigated as the positive electrodes. The application of NASICON-type

$Na_3V_2(PO_4)_3$ in a wide temperature range was reported with the combination of 0.4 mol dm^{-3} Na[FSA]-[C_2C_1im][FSA] IL electrolyte [82]. This work recorded the outstanding performance of $Na_3V_2(PO_4)_3$ in terms of high capacity and excellent cycle performance at 25 °C and 90 °C, suggesting a high safety over a wide temperature range. The electrochemical activity of $Li_2FeP_2O_7$ with an average potential of ~ 3.5 V vs. Li/Li^+ was extracted in a wide temperature range from 25 °C to 60 °C and 90 °C with the aid of imidazolium-based IL electrolyte, 30 mol% Li[FSA]-[C_2C_1im][FSA] [83]. Furthermore, the intermediate temperature of 90 °C realized the optimal performance, including the highest capacity (105 mAh g^{-1} at 110 mA g^{-1}), improved rate capability (82% of capacity retention at 3300 mA g^{-1}) and stable cycle performance (99.1% after 200 cycles at 110 mA g^{-1}). This work prompts the Li[FSA]-[C_2C_1im][FSA] system to be a potential electrolyte for LIBs operating at wide temperatures.

These positive electrode materials with the spinel, layered, and olivine structures work based on the insertion/extraction mechanism. However, the amount of alkali ions extracted from the crystal lattice in the process of charge-discharge is limited in order to maintain the structural frame, thereby restricting the capacity and energy density [84]. In recent years, a new type of positive materials that transport electrons based on the conversion reaction has attracted wide attention. These conversion-type materials utilize all possible redox in the charge-discharge process, thereby providing higher discharge capacity than that of insertion-type positive materials [85].

1.4 Metal fluoride positive electrodes

The conversion-type materials can be formalized as MX_n species (M = transition metals and X = H, N, O, F, P or S), in which M is reduced to the species at a lower oxidation state (sometimes pure metal) with the formation of LiX (NaX) [84, 85]. Although several conversion materials have been reported, only metal fluorides serve as the positive electrodes with high working potential for both LIBs and SIBs. The general formula of metal difluoride and metal trifluorides can be expressed as MF$_2$ and MF$_3$ (M = Mn, Fe, Co, Ni). Among them, iron fluorides are reasonable positive electrode materials with low cost, environmental benignity, and high specific capacity [85, 86]. The feasibility of operating an iron binary fluoride, FeF$_2$, at elevated temperatures was confirmed in LIBs with the aid of IL electrolyte (Table 1-2) [87]. However, the electrochemical researches of iron-based ternary and quaternary fluorides as positive electrodes for LIBs and SIBs in combination with IL electrolytes as well as elevated temperatures are still limited.

1.4.1 Binary iron fluorides

Iron(II) difluoride is one of the most promising candidates for positive electrodes due to the high thermodynamic reduction potential (2.66 V vs. Li/Li$^+$), high theoretical specific capacity (571 mAh g^{-1}), low cost, and low toxicity [88, 89]. The rutile-type structure of FeF$_2$ belongs to a tetragonal structure with the $P4_2/mnm$ space group, being composed of a hexagonal close-packed (hcp) anion lattice with cations occupying half of the octahedral sites (Figure 1-3a) [90]. In LIBs, the reaction of FeF$_2$ with Li was confirmed to form

metallic iron and LiF phases through a direct conversion process without an intercalation step as follows [91-93]:

$$Fe(II)F_2 + 2Li^+ + 2e^- \rightarrow 2LiF + Fe\ (4.0–1.5\ V\ vs.\ Li/Li^+) \quad (1)$$

The comprehensive conversion mechanism of monodisperse single-crystalline FeF_2 nanorods was further studied in 1 mol dm^{-3} Li[FSA]-[C_3C_1pyrr][FSA] IL electrolyte [87]. In this work, Fe/LiF was confirmed to be directly formed at the surface through conversion, and then a coherent trirutile and rocksalt phases were formed throughout the interior with the concomitant formation of a double-layered Fe/LiF shell. The fully discharged state contained iron particles nucleated at the low-energy interface in the fluoride matrix. Moreover, excellent electrochemical properties were also achieved with an initial discharge capacity of 570 mAh g^{-1} (close to the theoretical capacity) and capacity retention of 90% after 50 cycles at 28.5 mA g^{-1}. This cycling stability was solely superior to that measured in an organic electrolyte (1 mol dm^{-3} $LiPF_6$/EC:DMC). Such excellent performance of FeF_2 was considered to arise from the contribution of a stable IL-derived SEI which prevents the fusion of active particles.

FeF_2 were also studied in SIBs [94-96]. Different reaction pathways of FeF_2 in SIBs were clarified in a work of FeF_2-reduced graphene oxide (rGO) nanocomposite [95], where the discharged products containing Fe metal, NaF, and Na_3FeF_6 were confirmed to

be anchored on rGO through conversion reaction (eq. (2)) and a disproportionation reaction (eq. (3)) as follows:

$$Fe(II)F_2 + 2Na^+ + 2e^- \rightarrow 2NaF + Fe\ (4.5–1.5\ V\ vs.\ Na/Na^+) \quad (2)$$

$$Fe(II)F_2 + Na^+ + e^- \rightarrow 1/3Na_3FeF_6 + 2/3Fe\ (4.5–1.5\ V\ vs.\ Na/Na^+) \quad (3)$$

The nanocomposite of LiF-FeF_2 [97, 98] and NaF-FeF_2 [99] were also reported to provide a further understanding of the reaction mechanisms in the Li-Fe-F and Na-Fe-F systems. The reversal conversion reaction of LiF-FeF_2 to ReO_3-type FeF_3 was confirmed during the charging process. During discharging, an intermediate phase of Li_xFeF_3 ($0 < x < \sim 0.8$) was also clarified by inserting Li^+ into the ReO_3-type FeF_3 framework before the recovery of LiF-FeF_2 [98]. In SIBs, the decomposition of NaF induced the gradual transformation of FeF_2 into a FeF_3-like structure from the surface to the core during the charging process. However, NaF-FeF_2 was not recovered during the subsequent discharge process. Instead, the $NaFeF_3$-like structure was formed with the diffusion of Na^+ in the FeF_3-like structure, which was reversible during the subsequent cycles [99].

Iron(III) fluorides (FeF_3) has a distorted ReO_3 cubic structure in the space group of $R\bar{3}c$ (Figure 1-3b) and works as a positive electrode material based on both insertion/extraction and conversion reactions [100]. In principle, FeF_3 can be converted into the corresponding Fe metal and LiF (or NaF) mixture *via* three-electron transfer, thereby delivering a high theoretical capacity of 712 mAh g^{-1} at an average potential of

~ 2.7 V vs. Li/Li^+. This is over three times higher than that of insertion-type positive electrode materials [86]. As the most stable MF_3 compounds, FeF_3 is considered to be the suitable positive electrode material for LIBs and SIBs and has been extensively studied in electrochemical properties and reaction mechanisms.

Badway *et al*. synthesized nano-sized composites of FeF_3/C by ball-milled FeF_3 with conductive materials (expanded graphite, carbon black and activated carbon) and investigated its electrochemical properties as positive electrode material for LIBs in detail [101, 102]. These works revealed a reversible specific capacity of approximately 600 mAh g^{-1} of FeF_3 at 70 °C with the $LiPF_6$/EC:DMC organic electrolyte. They also reported the reaction pathway of FeF_3 as the positive electrode material for LIBs as follows:

$$Fe(III)F_3 + Li^+ + e^- \rightarrow LiFe(II)F_3 \text{ (4.5–2.5 V vs. } Li/Li^+) \quad (4)$$

$$LiFe(II)F_3 + 2Li^+ + 2e^- \rightarrow Fe(0) + 3LiF \text{ (2.5–1.5 V vs. } Li/Li^+) \quad (5)$$

The Li^+ insertion in the first process occurred in the voltage range of 4.5–2.5 V, in which an intermediate phase compound of $Li_{0.5}FeF_3$ was formed through a two-phase reaction, followed by the formation of $LiFe(II)F_3$ through a single-phase reaction. This one-electron transfer delivered a theoretical capacity of 237 mAh g^{-1}. During the subsequent discharge to 1.5 V, $LiFe(II)F_3$ and Li^+ further reacted in the second step with two-electron transfer (theoretical capacity of 485 mAh g^{-1}), which triggered the conversion reaction to lithium fluoride (LiF) and α-Fe metal.

First-principle calculations of the Li−Fe−F phase diagram [103] suggested that an intermediate phase of $Li_{0.25}FeF_3$ was formed upon the initial Li^+-insertion into FeF_3, which was classified as a perovskite structure with the occupancy of 0.25 Li^+ in the A site. Additional Li^+ insertion induced a structural transformation from the perovskite to trirutile structure accompanied by the formation of $Li_{0.5}FeF_3$. However, the subsequent reactions between Li^+ and trirutile $Li_{0.5}FeF_3$ engendered a conversion to the formation of LiF and Fe instead of the aforementioned experimental path that would entail the further insertion of Li^+ into the trirutile structure to form Li_xFeF_3 ($0.5 < x < 1$) through a single-phase reaction. Yamakawa *et al*. [104] identified that the intermediate $Li_{0.5}FeF_3$ phase was first formed heterogeneously *via* an insertion reaction, followed by a single-phase intercalation reaction in the range of $0.5 < x < 1$ in Li_xFeF_3. Moreover, through pair distribution function (PDF) analysis, they demonstrated the resemblance between the intermediate product $Li_{0.5}FeF_3$ and the trirutile structure. Later, Li and co-workers combined the results of in-situ synchrotron X-ray absorption spectroscopy (XAS), transmission electron microscopy (TEM), and PDF analysis to elucidate the asymmetric reaction pathway of FeF_3 with Li^+, in which trirutile $Li_{0.25}FeF_3$ and $Li_{0.5}FeF_3$ were calculated as the most stable intermediate phases (reaction pathway in Figure 1-4) [105].

A comprehensive structural investigation of the FeF_3 positive electrode material for LIBs was further reported by Hua *et al*. [106]. Initial lithiation of FeF_3 formed the FeF_2 phase on the particle surface and a cation-ordered but stacking-disordered phase A-$Li_xFe_yF_3$ whose structure is related to α-/β-$LiMnFeF_6$. Topotactic transformation to B-

(Fe being completely reduced to Fe^{2+}) and then C-$Li_xFe_yF_3$ with the high symmetry (*R*3*c*) subsequently occurred *via* an insertion-type reaction, prior to the formation of two-phase mixture of LiF and Fe.

At the same time, the study of FeF_3 in SIBs has also attracted great interest. Nishijima *et al*. [107] investigated the reversible Fe^{3+}/Fe^{2+} redox reaction in FeF_3 corresponding to Na insertion/extraction, which delivered a reversible capacity of 100 mAh g^{-1} in the cut-off voltage of 1.5–4.0 V. Fluoride-based open framework of $FeF_3 \cdot 0.33H_2O$ (*Cmcm*) was also synthesized through a solid-solid breakdown method in a typical IL $C_4C_1BF_4$ (tetrafluoroborate), which releases an initial discharge capacity of 130 mAh g^{-1} at 1.2 V for SIBs [108]. Ma *et al*. [109] synthesized a composite of FeF_3-Fe-rGO as positive electrode material for SIBs, in which FeF_3 was evenly distributed in the conductive substrate of Fe by generating FeF_3 *via* in-situ electrochemical reaction on the rGO surface. The results showed a high discharge capacity of 150 mAh g^{-1} at the current density of 50 mA g^{-1}, and excellent cycle performance. This work also proposed a Na^+ storage mechanism in the composite of FeF_3-Fe-rGO as follows:

$$FeF_3 + Na^+ \rightleftharpoons NaFeF_3 \text{ (1.5–4.5 V vs. Na/Na}^+\text{)} \quad (6)$$

The reduction of Fe^{3+} to Fe^{2+} was implemented through a classical insertion process between FeF_3 and $NaFeF_3$, but their structure and the existence of the Na_xFeF_3

intermediate phase have not been explored yet. Therefore, further studies are necessary on the reaction mechanism of FeF_3 in the Na system.

1.4.2 Iron-based ternary and quaternary fluorides

Except for FeF_2 and FeF_3, iron-based ternary and quaternary fluorides, such as $LiFe_2F_6$ (also referred as $Li_{0.5}FeF_3$ during the lithiation process of FeF_3 described above) [110], Li_3FeF_6 [111, 112], $LiNiFeF_6$ [113], $LiMnFeF_6$ [114], $NaFeF_3$ [115], Na_3FeF_6 [116], and $Na_2Fe_2F_7$ [117], were also investigated as the positive electrodes for LIBs and SIBs, respectively.

Most Li*M*(II)*M*(III)F_6–type fluorides (where *M*(II) = Fe, Co, Mg, Ni, Cu; *M*(III) = Fe, Cr, Ga) have been reported to embody the trirutile structure, such as trirutile $LiCoCrF_6$, $LiCoFeF_6$, and $LiFe_2F_6$ [118, 119]. Trirutile $LiFe_2F_6$ and $LiNiFeF_6$ were calculated to possess a stable crystal structure in the space group of $P4_2/mnm$ (Figure 1-5a) [120, 121]. Although the preparation and structural characterization of trirutile $LiFe_2F_6$ were systematically described in the literature in the early 1970s [118, 119], its application as a LIB positive material was only limited to the disordered rutile $LiFe_2F_6$ published in 2010 [110, 120]. Within the voltage range of 2.0–4.5 V, the stoichiometric $LiFe_2F_6$ exhibited an initial discharge capacity of 126 mAh g^{-1} in a LIB with $LiPF_6$:EC/DEC organic electrolyte [110]. In-situ XRD data proved that Li can be reversibly inserted/extracted into/from the disordered rutile $LiFe_2F_6$ to form Li-rich phase $Li_{1+x}Fe_2F_6$ ($0 < x < 0.6$) and Li-poor phase $Li_{1-y}Fe_2F_6$ ($0 < y < 0.5$) in a single-phase region.

It is worth noting that lithium transition metal fluorides do not exclusively crystallize in the trirutile structure. Depending on the arrangement of the different valence metal cations in the octahedral sites, the trigonal colquiriite-type $LiCaFeF_6$ ($P\bar{3}1c$) was synthesized by a solid-state reaction [122]. This colquiriite-type structure was reported to have spatially distributed cations occupying distorted octahedral environments between planes of closest-packed fluoride anions extending in the *ab* plane (Figure 1-5b). The colquiriite-type $LiCaFeF_6$ with an organic electrolyte was reported to achieve a discharge capacity of 112 mAh g^{-1} in the voltage range of 2.0–4.5 V and exhibited a capacity retention of 83.9% for 20 cycles. The charge-discharge process corresponded to a reversible response to Li extraction/insertion based on the electrochemically active redox couple of Fe^{3+}/Fe^{2+}.

Iron-based ternary fluorides containing Na^+ have also been discussed as the positive electrode materials of SIBs for a long time. $NaFeF_3$ indexed to be an orthorhombic structure in the space group of *Pnma* (Figure 1-5c) was found to be the only electrochemically active compound during the Na*M*(II)F_3 series (*M*(II) = Mn, Fe, Co, Ni, Cu) [123, 124]. The electrochemical properties of $NaFeF_3$ were discussed by controlling the particle size through changing the composition of the synthetic solution, in which the discharge capacity of 170 mAh g^{-1} was achieved for the optimal $NaFeF_3$ in the voltage range of 1.5–4.5 V (theoretical capacity of 197 mAh g^{-1}) [125, 126].

Trigonal $Na_2Fe_2F_7$ ($P3_121$) exhibited good electrochemical properties and cycle performance as the positive electrode of SIBs [117, 127]. The trigonal $Na_2Fe_2F_7$ was

reported to possess three-dimensionally connected FeF_6 octahedra (Figure 1-5d), thereby creating the large three-dimensional pathways for Na^+ diffusion and achieving high structural stability during the charge-discharge processes. High discharge capacity close to the theoretical capacity of 184 mAh g^{-1} (corresponding to 2 mol Na^+ per formula unit), excellent power-capability (~ 70% of the theoretical capacity at 5C), as well as excellent cycling performance (~ 88% capacity retention for 1000 cycles at 2C) were demonstrated in a work reported by Park *et al.* [127]. The structural change of trigonal $Na_2Fe_2F_7$ during charge-discharge was verified to be a single-phase reaction without any phase transition between the fully charged $Na_1Fe_2F_7$ and fully discharged $Na_3Fe_2F_7$ in the trigonal structure, accompanied by negligible volume change below ~ 1% during Na^+ extraction/insertion.

1.5 Aims of this study

The development of novel electrode materials with high capacity and energy density, as well as the investigation of electrolytes that contribute to performance and safety is urgent topics for current LIBs and SIBs. Iron fluorides, as one of the conversion-type positive materials, have become a research hotspot because of their advantages including low toxicity, abundant iron resources, high redox potential, and large theoretical capacity. However, their application as energy-dense positive electrode materials for LIBs and SIBs has been encumbered due to insufficient understanding of their electrochemical capabilities and limitations. Clearly, it is necessary to deeply understand the phase

evolution of the electrochemical reaction process that occurs in the Li-Fe-F and Na-Fe-F systems in order to make progress in their electrochemical and structural studies. Therefore, the aims of this study are to conduct a systematic exploration on the electrochemical reaction mechanisms of iron fluoride-based materials in IL electrolytes containing $[C_2C_1im]^+$ cation and $[FSA]^-$ anion at elevated temperatures. A brief summary of the aims regarding each chapter is given below:

Chapter 2 provides general information about the experimental methods, characterization techniques, and test conditions followed in Chapters 3 to 6.

In Chapter 3, ordered trirutile $LiFe_2F_6$ was prepared and investigated at elevated temperature of 90 °C with the aid of a thermally stable IL electrolyte. The comprehensive analysis of the phase evolution is rationalized by synchrotron X-ray diffraction combined with the Rietveld refinement (XRD) and X-ray absorption fine structure (XAFS) analyses.

In Chapter 4, lithium-storage mechanism of rutile $Li_{1.2}MnFe_{1.2}F_{6.8}$ containing two active transition metals is explored in details using synchrotron XRD and X-ray photoelectron spectroscopy (XPS).

In Chapter 5, two different charge-discharge processes of trirutile-derived FeF_3 and its complicated structural evolution during continuous sodiation and desodiation are explicated by synchrotron XRD and the Rietveld refinement.

In Chapter 6, multi-phase transformation of orthorhombic $NaFeF_3$ as the positive electrode material for SIBs is explored in IL electrolyte with the combination of

galvanostatic intermittent titration technique (GITT) and synchrotron XRD measurements.

Chapter 7 summarizes the entire thesis and describes prospects related to this work.

Table 1-1 Physiochemical and electrochemical properties of selected carbonate-based organic and imidazolium-based IL electrolytes.

Organic or Ionic liquid electrolytes	σ (mS cm^{-1}) @Temp. (°C)	η (mPa s) @Temp. (°C)	T_1 (°C)	T_2 (°C)	Electro-chemical Window (V)	Ref.
1 mol dm^{-3} $LiBF_4$:EC/DEC (3:7 in wt.)	2.1@25	-	-	-	-	[128]
1 mol dm^{-3} $LiBF_4$:PC	3.5@25	-	-	-	-	[128]
1 mol dm^{-3} $LiPF_6$:EC/DEC (1:1 in wt.)	7.56@25	-	-	-	-	[128]
1 mol dm^{-3} $LiPF_6$:EC/DEC (3:7 in wt.)	7.24@25	3.66@25	-	-	-	[129]
1 mol dm^{-3} $LiPF_6$:EC/DMC (1:1 in wt.)	10.1@20 11.4@25	3.2@30	-	-	-	[130, 131]
1 mol dm^{-3} $LiPF_6$:EC/DMC (3:7 in wt.)	11.14@20	1.96@25	-	-	-	[129, 132]
1 mol dm^{-3} $NaClO_4$-PC	6.0 @25	-	-	-	-	[133]
1 mol dm^{-3} $NaPF_6$:EC/DMC (1:1 in wt.)	10.5@20 12.14@25	2.3@30	-	-	-	[131]
10 mol% Li[FSA]-[C_2C_1im][FSA]	12.6@25 42.5@85	25.3@25 5.9@85	–16	–6	-	[134]
20 mol% Li[FSA]-[C_2C_1im][FSA]	10.1@25 36.9@85	36.3@25 7.4@85	–49	–19	-	[134]
30 mol% Li[FSA]-[C_2C_1im][FSA]	7.2@25 30.3@85	53.1@25 9.7@85	-	-	-	[134]
40 mol% Li[FSA]-[C_2C_1im][FSA]	4.6@25 22.8@85	87.4@25 13.1@85	-	-	-	[134]
10 mol% Na[FSA]-[C_2C_1im][FSA]	12.2@25	28.9@25	–24	–10	-	[135]
20 mol% Na[FSA]-[C_2C_1im][FSA]	8.5@25	43.4@25	-	–22	-	[135]
30 mol% Na[FSA]-[C_2C_1im][FSA]	5.4@25 31@90	78.0@25 9.2@90	-	-	5.1	[135, 136]
40 mol% Na[FSA]-[C_2C_1im][FSA]	2.9@25	157.8@25	-	-	-	[135]
50 mol% Na[FSA]-[C_2C_1im][FSA]	1.2@25	343.7@25	-	-	-	[135]

σ: ionic conducitivty, η: viscosity, t_{M^+}: transference number, T_1: the onset temperature of melting, T_2: the ending temperature of melting

Table 1-2 Selected positive electrode materials for LIBs and SIBs using IL electrolytes.

Cell configration	Electrolytes	Temp. / °C	1st cycle discharge capacity@rate / mAh g^{-1}@mA g^{-1}	Rate capability@rate / mAh g^{-1}@mA g^{-1}	Cyclability (cycle number@rate / cycles@mA g^{-1})	Battery system	Ref.
Li/$LiNi_{0.5}Mn_{1.5}O_4$	1 mol dm^{-3} Li[TFSA]-[C_6C_1pyrr][FSA]	25	120@14.7	–	70.2% (55)	LIBs	[137]
Li/$LiNi_{0.5}Mn_{1.5}O_4$	2.4 mol dm^{-3} Li[TFSA]-[C_3C_1pyrr][FSA]	25	135@14.7	100@294	88% (200@147)	LIBs	[138]
Li/$LiNi_{0.5}Mn_{1.5}O_4$	1 mol dm^{-3} Li[FSA]-[C_3C_1pyrr][FSA]	65	122@292	106.2@730	85.3% (300)	LIBs	[61]
Li/$LiNi_{0.8}Mn_{0.1}Co_{0.1}O_2$	1.2 mol dm^{-3} Li[FSA]-[C_1C_3pyrr][FSA]	25	200@10	30@1000	95% (150)	LIBs	[73]
Li/$Li_{1.2}Ni_{0.2}Mn_{0.6}O_2$	20 mol% Li[TFSA]-[C_4C_1pyrr][FSA]	20	163@125 150@250	30@2500	99.6% (2000@125) 81.1% (500@250)	LIBs	[139]
Na/O′3-type $NaMnO_2$	1 mol dm^{-3} Na[TFSA]-[C_4C_1im][TFSA]	25	191@10	–	76% (100)	SIBs	[140]
Na/P2-$Na_{0.6}Ni_{0.22}Al_{0.11}Mn_{0.66}O_2$	10 mol% Na[FSA]-[C_4C_1pyrr][FSA]	20	140@30	–	100% (200)	SIBs	[47]
Na/P2-$Na_{2/3}Mn_{0.8}Fe_{0.1}Ti_{0.1}O_2$	0.35 mol dm^{-3} Na[FSA]-[C_4C_1pyrr][FSA]	20	138@0.1C	–	97.1% (100@0.1C) 93.6% (300@1C)	SIBs	[141]
Na/P3-$Na_{2/3}Ni_{1/3}Mg_{1/6}Mn_{1/2}O_2$	3 mol dm^{-3} Li[TFSA]-[[C_4C_1pyrr]][FSA]	40	135@0.1C	115@0.2C	93% (20)	Hybrid L/SIBs	[142]
Li/$Li_2FeP_2O_7$	30 mol% Li[FSA]-[C_2C_1im][FSA]	90	70@110	70@5500	99.1% (200)	LIBs	[83]
Na/$Na_4Ni_3(PO_4)_2(P_2O_7)$	10 mol% Na[TFSA]:[C_3C_1pyrr][FSA]	20	63@10	–	~ 79% (10)	SIBs	[143]
Na/$NaFePO_4$	0.5 mol dm^{-3} Na[TFSA]-[C_4C_1pyrr][TFSA]	50	125@7.7	81.25@154	–	SIBs	[75]
Na/$NaFePO_4$	1 mol dm^{-3} Na[TFSA]-[C_4C_1pyrr][TFSA]	50	–	–	87% (100@46.2)	SIBs	[75]
Na/$NaFePO_4$	30 mol% Na[FSA]-[C_2C_1im][FSA]	90	107@15.5	5@1550	67.2% (100@155)	SIBs	[144]
Na/$Na_3V_2(PO_4)_3$	0.4 mol dm^{-3} Na[FSA]-[C_2C_1im][FSA]	25 90	~ 100@117	50.1@58500	99% (300@117) 89.2% (5000@2340)	SIBs	[82]
Na/$Na_3V_2(PO_4)_3$	1 mol dm^{-3} Na[FSA]-[C_3C_1pyrr][FSA]	25	89@5.85	60@1170	89% (4800@1170)	SIBs	[145]
Na/$Na_3V_2(PO_4)_3$	40 mol% Na[FSA]-[C_2C_1im][FSA]	90	90@2C	82.3@11800	100% (200)	SIB	[146]
Li/FeF_2	1 mol dm^{-3} Li[FSA]-[C_3C_1pyrr][FSA]	25	700@28.5	500@285	> 90% (50)	LIBs	[87]

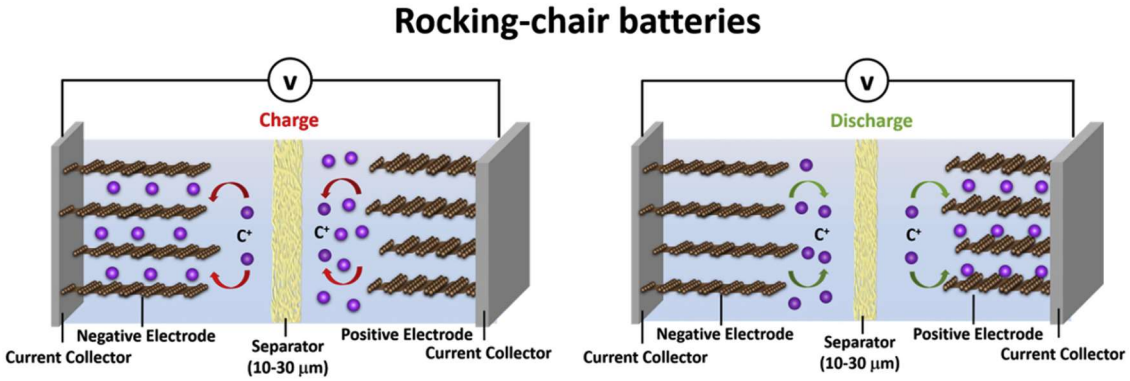

Figure 1-1 Schematic of the rocking-chair batteries with alkali metal ions shuttling between negative and positive electrodes [27]. The symbol, C^+, denotes cation.

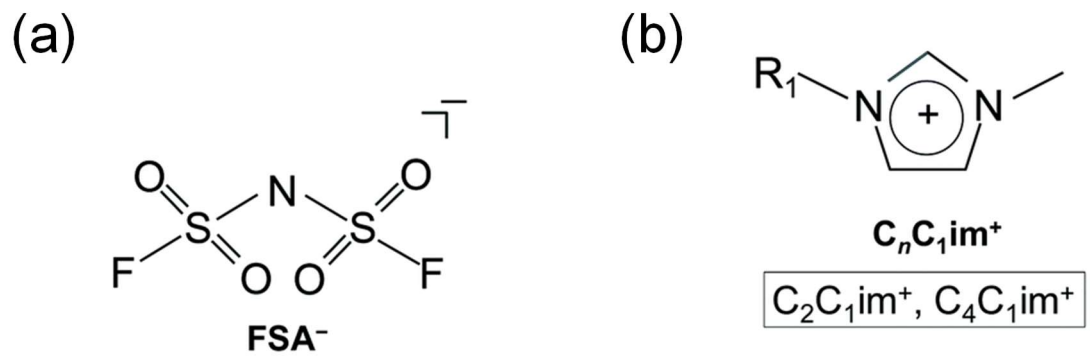

Figure 1-2 Structures (a) $[FSA]^-$ anion and (b) 1-alkyl-3-methylimidazolium cation used for ILs [48].

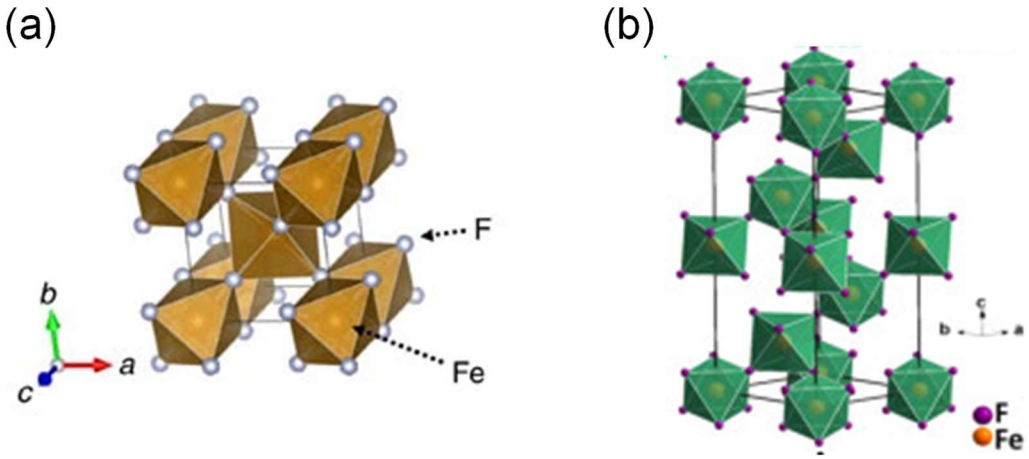

Figure 1-3 Crystal structures of iron fluorides. (a) Rutile FeF_2 ($P4_2/mnm$) [90]. (b) Rhombohedral FeF_3 ($R\bar{3}c$) [100].

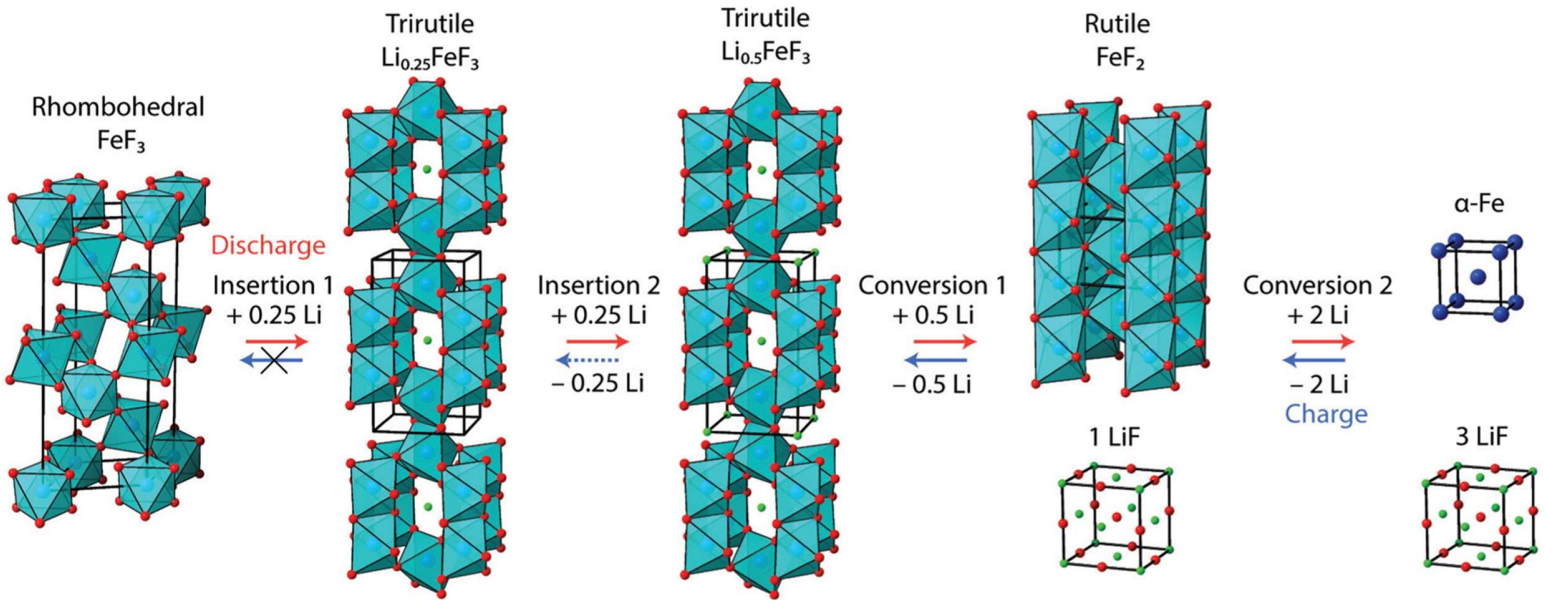

Figure 1-4 The discharge and charge reaction pathways of rhombohedral FeF_3 ($R\bar{3}c$) in LIBs [105].

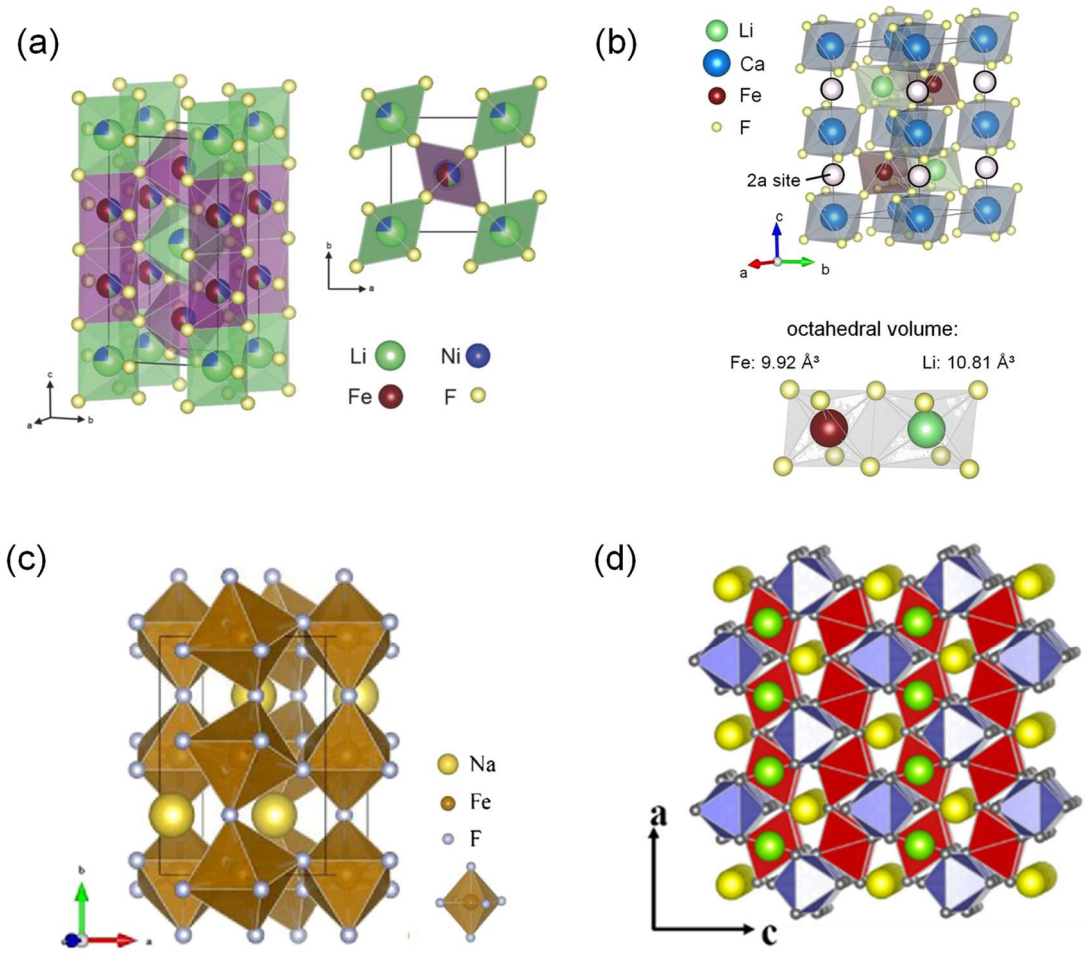

Figure 1-5 Crystal structures of iron-based ternary and quaternary fluorides. (a) Trirutile $LiNiFeF_6$ ($P4_2/mnm$) [100]. (b) Colquiriite-type $LiCaFeF_6$ ($P\bar{3}1c$) [122]. (c) Orthorhombic $NaFeF_3$ ($Pnma$) [124]. (d) Trigonal $Na_2Fe_2F_7$ ($P3_121$). For the $Na_2Fe_2F_7$ structure in (d), blue and red octahedra correspond to $Fe^{3+}F_6$ and $Fe^{2+}F_6$ units, respectively. The yellow balls represent sodium ions sit in the 4*e* and 4*a* sites, and the green balls denote the sodium ions are in the 4*d* sites. Fluoride ions are shown in gray color [117].

References

[1] Z. Yang, J. Zhang, M.C. Kintner-Meyer, X. Lu, D. Choi, J.P. Lemmon, J. Liu, Chem. Rev., 111 (2011) 3577–3613.

[2] A. Evans, V. Strezov, T.J. Evans, Renew. Sust. Energ. Rev., 16 (2012) 4141–4147.

[3] C. Heubner, T. Lein, M. Schneider, A. Michaelis, J. Mater. Chem. A, 8 (2020) 16854–16883.

[4] H. Chen, T.N. Cong, W. Yang, C. Tan, Y. Li, Y. Ding, Prog. Nat. Sci., 19 (2009) 291–312.

[5] H. Qian, J. Zhang, J. Lai, W. Yu, IEEE Trans. Power Electron., 26 (2011) 886–896.

[6] J. Tollefson, Nature, 456 (2008) 436.

[7] B. Dunn, H. Kamath, J.-M. Tarascon, Science, 334 (2011) 928–935.

[8] M. Li, J. Lu, Z. Chen, K. Amine, Adv. Mater., 30 (2018) 1800561.

[9] M. Winter, B. Barnett, K. Xu, Chem. Rev., 118 (2018) 11433–11456.

[10] T. Kim, W. Song, D.-Y. Son, L.K. Ono, Y. Qi, J. Mater. Chem. A, 7 (2019) 2942–2964.

[11] Y. Lyu, X. Wu, K. Wang, Z. Feng, T. Cheng, Y. Liu, M. Wang, R. Chen, L. Xu, J. Zhou, Y. Lu, B. Guo, Adv. Energy Mater., 11 (2021) 1−29.

[12] K. Kubota, M. Dahbi, T. Hosaka, S. Kumakura, S. Komaba, Chem. Rec., 18 (2018) 459–479.

[13] M. Bianchini, M. Roca-Ayats, P. Hartmann, T. Brezesinski, J. Janek, Angew. Chem. Int. Ed. Engl., 58 (2019) 10434−10458.

[14] A.K. Padhi, K.S. Nanjundaswamy, J.B. Goodenough, J. Electrochem. Soc., 144 (1997) 1188–1194.

[15] J. Li, Z.-F. Ma, Chem, 5 (2019) 3–6.

[16] D.E. Demirocak, S.S. Srinivasan, E.K. Stefanakos, Appl. Sci., 7 (2017) 731.

[17] C. Delmas, Adv. Energy Mater., 8 (2018) 1703137.

[18] K. Kubota, S. Komaba, J. Electrochem. Soc., 162 (2015) A2538–A2550.

[19] L.P. Wang, L. Yu, X. Wang, M. Srinivasan, Z.J. Xu, J. Mater. Chem. A, 3 (2015) 9353−9378.

[20] Y. Sun, S. Guo, H. Zhou, Adv. Energy Mater., 9 (2018) 1800212.

[21] D. Kundu, E. Talaie, V. Duffort, L.F. Nazar, Angew. Chem. Int. Ed. Engl., 54 (2015) 3431–3448.

[22] X.-P. Gao, H.-X. Yang, Energy Environ. Sci., 3 (2010) 174–189.

[23] J. Cho, S. Jeong, Y. Kim, Prog. Energy Combust. Sci., 48 (2015) 84–101.

[24] F. Wu, M. Liu, Y. Li, X. Feng, K. Zhang, Y. Bai, X. Wang, C. Wu, Electrochem. Energy Rev., 4 (2021) 382–446.

[25] B. Scrosati, J. Garche, J. Power Sources, 195 (2010) 2419–2430.

[26] J.B. Goodenough, K.S. Park, J. Am. Chem. Soc., 135 (2013) 1167–1176.

[27] Y. Sui, C. Liu, R.C. Masse, Z.G. Neale, M. Atif, M. AlSalhi, G. Cao, Energy Storage Materials, 25 (2020) 1–32.

[28] J. Liu, C. Xu, Z. Chen, S. Ni, Z.X. Shen, Green Energy Environ., 3 (2018) 20–41.

[29] W. Li, B. Song, A. Manthiram, Chem. Soc. Rev., 46 (2017) 3006–3059.

[30] J.B. Goodenough, Y. Kim, Chem. Mater., 22 (2009) 587–603.

[31] W.-J. Zhang, J. Power Sources, 196 (2011) 877–885.

[32] S. Fang, D. Bresser, S. Passerini, Adv. Energy Mater., 10 (2019) 1902485.

[33] L. Yu, L.P. Wang, H. Liao, J. Wang, Z. Feng, O. Lev, J.S.C. Loo, M.T. Sougrati, Z.J. Xu, Small, 14 (2018) 1703338.

[34] N. Nitta, F. Wu, J.T. Lee, G. Yushin, Mater. Today, 18 (2015) 252–264.

[35] M. Gauthier, T.J. Carney, A. Grimaud, L. Giordano, N. Pour, H.H. Chang, D.P. Fenning, S.F. Lux, O. Paschos, C. Bauer, F. Maglia, S. Lupart, P. Lamp, Y. Shao-Horn, J. Phys. Chem. Lett., 6 (2015) 4653–4672.

[36] A. Basile, M. Hilder, F. Makhlooghiazad, C. Pozo-Gonzalo, D.R. MacFarlane, P.C. Howlett, M. Forsyth, Adv. Energy Mater., 8 (2018) 1703491.

[37] I. Moeez, D. Susanto, W. Chang, H.-D. Lim, K.Y. Chung, Chem. Eng. J., 425 (2021) 130547.

[38] G.G. Eshetu, G.A. Elia, M. Armand, M. Forsyth, S. Komaba, T. Rojo, S. Passerini, Adv. Energy Mater., 10 (2020).

[39] M. Marcinek, J. Syzdek, M. Marczewski, M. Piszcz, L. Niedzicki, M. Kalita, A. Plewa-Marczewska, A. Bitner, P. Wieczorek, T. Trzeciak, M. Kasprzyk, P.Łężak, Z. Zukowska, A. Zalewska, W. Wieczorek, Solid State Ionics, 276 (2015) 107–126.

[40] K. Vignarooban, R. Kushagra, A. Elango, P. Badami, B.E. Mellander, X. Xu, T.G. Tucker, C. Nam, A.M. Kannan, Int. J. Hydrog. Energy, 41 (2016) 2829–2846.

[41] L. Lu, X. Han, J. Li, J. Hua, M. Ouyang, J. Power Sources, 226 (2013) 272–288.

[42] M.-T.F. Rodrigues, G. Babu, H. Gullapalli, K. Kalaga, F.N. Sayed, K. Kato, J. Joyner, P.M. Ajayan, Nat. Energy, 2 (2017) 1−14.

[43] X. Lin, M. Salari, L.M. Arava, P.M. Ajayan, M.W. Grinstaff, Chem. Soc. Rev., 45 (2016) 5848−5887.

[44] D.R. MacFarlane, N. Tachikawa, M. Forsyth, J.M. Pringle, P.C. Howlett, G.D. Elliott, J.H. Davis, M. Watanabe, P. Simon, C.A. Angell, Energy Environ. Sci., 7 (2014) 232−250.

[45] D.R. MacFarlane, M. Forsyth, P.C. Howlett, M. Kar, S. Passerini, J.M. Pringle, H. Ohno, M. Watanabe, F. Yan, W. Zheng, S. Zhang, J. Zhang, Nat. Rev. Mater., 1 (2016) 1–15.

[46] M. Watanabe, M.L. Thomas, S. Zhang, K. Ueno, T. Yasuda, K. Dokko, Chem. Rev., 117 (2017) 7190–7239.

[47] L.G. Chagas, S. Jeong, I. Hasa, S. Passerini, ACS Appl. Mater. Interfaces, 11 (2019) 22278–22289.

[48] K. Matsumoto, J. Hwang, S. Kaushik, C.-Y. Chen, R. Hagiwara, Energy Environ. Sci., 12 (2019) 3247–3287.

[49] I.A. Shkrob, T.W. Marin, Y. Zhu, D.P. Abraham, J. Phys. Chem. C, 118 (2014) 19661–19671.

[50] P.J. Fischer, M.P. Do, R.M. Reich, A. Nagasubramanian, M. Srinivasan, F.E. Kuhn, Phys. Chem. Chem. Phys., 20 (2018) 29412–29422.

[51] M. Ishikawa, T. Sugimoto, M. Kikuta, E. Ishiko, M. Kono, J. Power Sources, 162 (2006) 658–662.

[52] H. Matsumoto, H. Sakaebe, K. Tatsumi, M. Kikuta, E. Ishiko, M. Kono, J. Power Sources, 160 (2006) 1308–1313.

[53] J. Hwang, H. Okada, R. Haraguchi, S. Tawa, K. Matsumoto, R. Hagiwara, J. Power Sources, 453 (2020) 1−6.

[54] Q. Yang, Z. Zhang, X.G. Sun, Y.S. Hu, H. Xing, S. Dai, Chem. Soc. Rev., 47 (2018) 2020–2064.

[55] J. Zhang, W. Wang, W. Wang, S. Wang, B. Li, ACS Appl. Mater. Interfaces, 11 (2019) 22051–22066.

[56] L. Chen, M. Fiore, J.E. Wang, R. Ruffo, D.-K. Kim, G. Longoni, Adv. Sustainable Syst., 2 (2018) 1700153.

[57] Y. Yang, E.G. Okonkwo, G. Huang, S. Xu, W. Sun, Y. He, Energy Storage Materials, 36 (2021) 186–212.

[58] Y. Fang, Z. Chen, L. Xiao, X. Ai, Y. Cao, H. Yang, Small, 14 (2018) 1703116.

[59] R. Sun, P. Jakes, S. Eurich, D. van Holt, S. Yang, M. Homberger, U. Simon, H. Kungl, R.-A. Eichel, Appl. Magn. Reson., 49 (2018) 415–427.

[60] O.K. Park, Y. Cho, S. Lee, H.-C. Yoo, H.-K. Song, J. Cho, Energy Environ. Sci., 4 (2011) 1621–1633.

[61] H.J. Lee, Z. Brown, Y. Zhao, J. Fawdon, W. Song, J.H. Lee, J. Ihli, M. Pasta, Chem. Mater., 33 (2021) 1238–1248.

[62] N. Yabuuchi, K. Kubota, M. Dahbi, S. Komaba, Chem. Rev., 114 (2014) 11636–11682.

[63] N. Yabuuchi, H. Yoshida, S. Komaba, Electrochemistry, 80 (2012) 716–719.

[64] M. Guignard, C. Didier, J. Darriet, P. Bordet, E. Elkaim, C. Delmas, Nat. Mater., 12 (2013) 74–80.

[65] C. Delmas, C. .Fouassier, P. Hagenmuller, Physica B+C, 99 (1980) 81–85.

[66] F. Lian, P. Axmann, C. Stinner, Q.G. Liu, M. Wohlfahrt-Mehrens, J. Appl. Electrochem., 38 (2008) 613–617.

[67] D. Darbar, E.C. Self, L. Li, C. Wang, H.M. Meyer, C. Lee, J.R. Croy, M. Balasubramanian, N. Muralidharan, I. Bhattacharya, I. Belharouak, J. Nanda, J. Power Sources, 479 (2020) 228591.

[68] R. Qian, Y. Liu, T. Cheng, P. Li, R. Chen, Y. Lyu, B. Guo, ACS Appl. Mater. Interfaces, 12 (2020) 13813–13823.

[69] L. Zheng, L. Li, R. Shunmugasundaram, M.N. Obrovac, ACS Appl. Mater. Interfaces, 10 (2018) 38246–38254.

[70] D.D. Yuan, Y.X. Wang, Y.L. Cao, X.P. Ai, H.X. Yang, ACS Appl. Mater. Interfaces, 7 (2015) 8585–8591.

[71] N. Yabuuchi, M. Yano, H. Yoshida, S. Kuze, S. Komaba, J. Electrochem. Soc., 160 (2013) A3131–A3137.

[72] J.-Y. Hwang, S.-T. Myung, Y.-K. Sun, J. Phys. Chem. C, 122 (2018) 13500–13507.

[73] A. Heist, S. Hafner, S.-H. Lee, J. Electrochem. Soc., 166 (2019) A873–A879.

[74] T. Jin, H. Li, K. Zhu, P.F. Wang, P. Liu, L. Jiao, Chem. Soc. Rev., 49 (2020) 2342–2377.

[75] N. Wongittharom, T.-C. Lee, C.-H. Wang, Y.-C. Wang, J.-K. Chang, J. Mater. Chem. A, 2 (2014) 5655–5661.

[76] J. Kim, D.-H. Seo, H. Kim, I. Park, J.-K. Yoo, S.-K. Jung, Y.-U. Park, W.A. Goddard Iii, K. Kang, Energy Environ. Sci., 8 (2015) 540–545.

[77] J. Hwang, K. Matsumoto, Y. Orikasa, M. Katayama, Y. Inada, T. Nohira, R. Hagiwara, J. Power Sources, 377 (2018) 80–86.

[78] A.S. Andersson, B. Kalska, P. Eyob, D. Aernout, L. Haggstrom, J.O. Thomas, Solid State Ionics, 140 (2001) 63–70.

[79] R. Rajagopalan, B. Chen, Z. Zhang, X.L. Wu, Y. Du, Y. Huang, B. Li, Y. Zong, J. Wang, G.H. Nam, M. Sindoro, S.X. Dou, H.K. Liu, H. Zhang, Adv. Mater., 29 (2017) 1605694.

[80] Y. Jiang, X. Zhou, D. Li, X. Cheng, F. Liu, Y. Yu, Adv. Energy Mater., 8 (2018) 1800068.

[81] L. Tan, S. Zhang, C. Deng, J. Power Sources, 275 (2015) 6–13.

[82] J. Hwang, K. Matsumoto, R. Hagiwara, Adv. Sustainable Syst., 2 (2018) 1700171.

[83] J. Hwang, H. Okada, R. Haraguchi, S. Tawa, K. Matsumoto, R. Hagiwara, J. Power Sources, 453 (2020) 227911.

[84] J. Cabana, L. Monconduit, D. Larcher, M.R. Palacin, Adv. Mater., 22 (2010) E170–E192.

[85] C. Li, K. Chen, X. Zhou, J. Maier, npj Comput. Mater., 4 (2018).

[86] D.E. Conte, N. Pinna, Mater. Renew. Sustain. Energy, 3 (2014) 1−22.

[87] A.W. Xiao, H.J. Lee, I. Capone, A. Robertson, T.U. Wi, J. Fawdon, S. Wheeler, H.W. Lee, N. Grobert, M. Pasta, Nature Mater., 19 (2020) 644–654.

[88] S.K. Martha, J. Nanda, H. Zhou, J.C. Idrobo, N.J. Dudney, S. Pannala, S. Dai, J. Wang, P.V. Braun, RSC Adv., 4 (2014) 6730–6737.

[89] S. Kim, J. Liu, K. Sun, J. Wang, S.J. Dillon, P.V. Braun, Adv. Funct. Mater., 27 (2017) 1702783.

[90] F. Wang, S.W. Kim, D.H. Seo, K. Kang, L. Wang, D. Su, J.J. Vajo, J. Wang, J. Graetz, Nat. Commun., 6 (2015) 6668.

[91] F. Wang, R. Robert, N.A. Chernova, N. Pereira, F. Omenya, F. Badway, X. Hua, M. Ruotolo, R. Zhang, L. Wu, V. Volkov, D. Su, B. Key, M.S. Whittingham, C.P. Grey, G.G. Amatucci, Y. Zhu, J. Graetz, J. Am. Chem. Soc., 133 (2011) 18828–18836.

[92] F. Wang, H.C. Yu, M.H. Chen, L. Wu, N. Pereira, K. Thornton, A. Van der Ven, Y. Zhu, G.G. Amatucci, J. Graetz, Nat. Commun., 3 (2012) 1201.

[93] W. Gu, A. Magasinski, B. Zdyrko, G. Yushin, Adv. Energy Mater., 5 (2015) 1401148.

[94] K. He, Y. Zhou, P. Gao, L. Wang, N. Pereira, G.G. Amatucci, K.-W. Nam, X.-Q. Yang, Y. Zhu, F. Wang, D. Su, ACS Nano, 8 (2014) 7251–7259.

[95] D. Ni, W. Sun, C. Lu, Z. Wang, J. Qiao, H. Cai, C. Liu, K. Sun, J. Power Sources, 413 (2019) 449–458.

[96] A.Y. Maulana, C.M. Futalan, J. Kim, J. Alloys Compd., 840 (2020) 155719.

[97] S.-W. Kim, K.-W. Nam, D.-H. Seo, J. Hong, H. Kim, H. Gwon, K. Kang, Nano Today, 7 (2012) 168–173.

[98] S. Tawa, Y. Sato, Y. Orikasa, K. Matsumoto, R. Hagiwara, J. Power Sources, 412 (2019) 180–188.

[99] I. Hwang, S.-K. Jung, E.-S. Jeong, H. Kim, S.-P. Cho, K. Ku, H. Kim, W.-S. Yoon, K. Kang, Nano Res., 10 (2017) 4388–4397.

[100] T. Zhao, L. Li, R. Chen, H. Wu, X. Zhang, S. Chen, M. Xie, F. Wu, J. Lu, K. Amine, Nano Energy, 15 (2015) 164–176.

[101] F. Badway, F. Cosandey, N. Pereira, G.G. Amatucci, J. Electrochem. Soc., 150 (2003) A1318–A1327.

[102] F. Badway, N. Pereira, F. Cosandey, G.G. Amatucci, J. Electrochem. Soc., 150 (2003) A1209–A1218.

[103] R.E. Doe, K.A. Persson, Y.S. Meng, G. Ceder, Chem. Mater., 20 (2008) 5274–5283.

[104] N. Yamakawa, M. Jiang, B. Key, C.P. Grey, J. Am. Chem. Soc., 131 (2009) 10525−10536.

[105] L. Li, R. Jacobs, P. Gao, L. Gan, F. Wang, D. Morgan, S. Jin, J. Am. Chem. Soc., 138 (2016) 2838–2848.

[106] X. Hua, A.S. Eggeman, E. Castillo-Martinez, R. Robert, H.S. Geddes, Z. Lu, C.J. Pickard, W. Meng, K.M. Wiaderek, N. Pereira, G.G. Amatucci, P.A. Midgley, K.W. Chapman, U. Steiner, A.L. Goodwin, C.P. Grey, Nature Mater., (2021) 841–850.

[107] M. Nishijima, I.D. Gocheva, S. Okada, T. Doi, J.-i. Yamaki, T. Nishida, J. Power Sources, 190 (2009) 558–562.

[108] C. Li, C. Yin, X. Mu, J. Maier, Chem. Mater., 25 (2013) 962–969.

[109] D.-l. Ma, H.-g. Wang, Y. Li, D. Xu, S. Yuan, X.-l. Huang, X.-b. Zhang, Y. Zhang, Nano Energy, 10 (2014) 295–304.

[110] P. Liao, J. Li, J.R. Dahn, J. Electrochem. Soc., 157 (2010) A355–A361.

[111] E. Gonzalo, A. Kuhn, F. García-Alvarado, M.S. Islam, J. Mater. Chem. A, 1 (2013) 6588–6592.

[112] J. Kohl, D. Wiedemann, S. Nakhal, P. Bottke, N. Ferro, T. Bredow, E. Kemnitz, M. Wilkening, P. Heitjans, M. Lerch, J. Mater. Chem., 22 (2012) 15819–15827.

[113] G. Lieser, C. Dräger, M. Schroeder, S. Indris, L. de Biasi, H. Geßwein, S. Glatthaar, H. Ehrenberg, J.R. Binder, J. Electrochem. Soc., 161 (2014) A1071–A1077.

[114] G. Lieser, L.d. Biasi, H. Geßwein, S. Indris, C. Dräger, M. Schroeder, S. Glatthaar, H. Ehrenberg, J.R. Binder, J. Electrochem. Soc., 161 (2014) A1869–A1876.

[115] A. Kitajou, H. Komatsu, K. Chihara, I.D. Gocheva, S. Okada, J.-i. Yamaki, J. Power Sources, 198 (2012) 389–392.

[116] R.A. Shakoor, S.Y. Lim, H. Kim, K.-W. Nam, J.K. Kang, K. Kang, J.W. Choi, Solid State Ionics, 218 (2012) 35–40.

[117] U.K. Dey, N. Barman, S. Ghosh, S. Sarkar, S.C. Peter, P. Senguttuvan, Chem. Mater., 31 (2019) 295–299.

[118] W. Viebahn, W. Rüdorff, H. Kornelson, Z. Naturforsch. B, 22 (1967) 1218.

[119] V.W. Viebahn, W. Rudorff, R. Hänsler, Chimia, 23 (1969) 503–510.

[120] P. Liao, R.A. Dunlap, J.R. Dahn, J. Electrochem. Soc., 157 (2010) A1080–A1084.

[121] J. Fourquet, E. Samedi, Y. Calage, J. Solid State Chem., 77 (1988) 84–89.

[122] L. de Biasi, G. Lieser, C. Dräger, S. Indris, J. Rana, G. Schumacher, R. Mönig, H. Ehrenberg, J.R. Binder, H. Geßwein, J. Power Sources, 362 (2017) 192–201.

[123] A. Kitajou, Y. Ishado, T. Yamashita, H. Momida, T. Oguchi, S. Okada, Electrochim. Acta, 245 (2017) 424–429.

[124] S. Yu, P. Zhang, S.Q. Wu, A.Y. Li, Z.Z. Zhu, Y. Yang, J. Solid State Electrochem., 18 (2014) 2071–2075.

[125] Y. Yamada, T. Doi, I. Tanaka, S. Okada, J.-i. Yamaki, J. Power Sources, 196 (2011) 4837–4841.

[126] K.V. Kravchyk, T. Zünd, M. Wörle, M.V. Kovalenko, M.I. Bodnarchuk, Chem. Mater., 30 (2018) 1825–1829.

[127] H. Park, Y. Lee, M.-k. Cho, J. Kang, W. Ko, Y.H. Jung, T.-Y. Jeon, J. Hong, H. Kim, S.-T. Myung, J. Kim, Energy Environ. Sci., 14 (2021) 1469–1479.

[128] R.W. Schmitz, P. Murmann, R. Schmitz, R. Müller, L. Krämer, J. Kasnatscheew, P. Isken, P. Niehoff, S. Nowak, G.-V. Röschenthaler, N. Ignatiev, P. Sartori, S. Passerini, M. Kunze, A. Lex-Balducci, C. Schreiner, I. Cekic-Laskovic, M. Winter, Prog. Solid State Chem., 42 (2014) 65–84.

[129] D.Y.W. Yu, K. Donoue, T. Inoue, M. Fujimoto, S. Fujitani, J. Electrochem. Soc., 153 (2006) A835–A839.

[130] C.L. Berhaut, D. Lemordant, P. Porion, L. Timperman, G.e. Schmidtc, M.e. Anouti, RSC Adv., 9 (2019) 4599–4608.

[131] D.I. Iermakova, R. Dugas, M.R. Palacín, A. Ponrouch, J. Electrochem. Soc., 162 (2015) A7060–A7066.

[132] E.R. Logan, E.M. Tonita, K.L. Gering, J. Li, X. Ma, L.Y. Beaulieu, J.R. Dahn, J. Electrochem. Soc., 165 (2018) A21–A30.

[133] K. Kuratani, N. Uemura, H. Senoh, H.T. Takeshita, T. Kiyobayashi, J. Power Sources, 223 (2013) 175–182.

[134] K. Matsumoto, E. Nishiwaki, T. Hosokawa, S. Tawa, T. Nohira, R. Hagiwara, J. Phys. Chem. C, 121 (2017) 9209–9219.

[135] K. Matsumoto, T. Hosokawa, T. Nohira, R. Hagiwara, A. Fukunaga, K. Numata, E. Itani, S. Sakai, K. Nitta, S. Inazawa, J. Power Sources, 265 (2014) 36–39.

[136] R. Hagiwara, K. Matsumoto, J. Hwang, T. Nohira, Chem. Rec., 19 (2018) 758–770.

[137] H. Qi, Y. Ren, S. Guo, Y. Wang, S. Li, Y. Hu, F. Yan, ACS Appl. Mater. Interfaces, 12 (2020) 591–600.

[138] P.C. Rath, Y.-W. Wang, J. Patra, B. Umesh, T.-J. Yeh, S. Okada, J. Li, J.-K. Chang, Chem. Eng. J., 415 (2021) 128904.

[139] F. Wu, G.-T. Kim, T. Diemant, M. Kuenzel, A.R. Schuer, X. Gao, B. Qin, D. Alwast, Z. Jusys, R.J. Behm, D. Geiger, U. Kaiser, S. Passerini, Adv. Energy Mater., 10 (2020) 2001830.

[140] H. Si, L. Li, W. Hao, L. Seidl, X. Cheng, H. Xu, G. Jia, O. Schneider, S. An, X. Qiu, ACS Appl. Energy Mater., 2 (2019) 5050–5056.

[141] M. Zarrabeitia, L. Gomes Chagas, M. Kuenzel, E. Gonzalo, T. Rojo, S. Passerini, M.A. Munoz-Marquez, ACS Appl. Mater. Interfaces, 11 (2019) 28885–28893.

[142] M. Kalapsazova, K. Kostov, E. Zhecheva, R. Stoyanova, Front. Chem., 8 (2020) 600140.

[143] H. Zhang, I. Hasa, D. Buchholz, B. Qin, D. Geiger, S. Jeong, U. Kaiser, S. Passerini, NPG Asia Mater., 9 (2017) e370.

[144] J. Hwang, K. Matsumoto, Y. Orikasa, M. Katayama, Y. Inada, T. Nohira, R. Hagiwara, J. Power Sources, 377 (2018) 80–86.

[145] C.V. Manohar, T.C. Mendes, M. Kar, D. wang, C. Xiao, M. Forsyth, S. Mitra, D.R. MacFarlane, Chem. Commun., 54 (2018) 3500–3503.

[146] J. Hwang, K. Matsumoto, R. Hagiwara, ACS Appl. Energy Mater., 2 (2019) 2818–2827.

Chapter 2

Experimental

2.1 Apparatus and material handling

All air-sensitive reagents and active materials, assembling and disassembling of coin cells, and the packing of ball-mill vessels were handled in a glove box (Miwa Manufacturing Co., Ltd., DBO-2LKH-HNBR) filled with argon gas (purity = 99.995%) and equipped with a gas purification system (Miwa Manufacturing Co., Ltd., MS3-P60S-N). The atmosphere inside the glove box was maintained at a dew point below –90 °C and an oxygen concentration less than 1 ppm, which was monitored by a dew point meter (GE panametrics Ltd., MTS5-311-10) and an oxygen analyzer (GE Sensing & Inspection Technologies Co., Ltd., DF-150ε), respectively.

All the ILs and electrode materials were dried in a drying vessel using a vacuum line, shown in Figures 2-1 and 2-2, prior to use. The vacuum line was composed of stainless-steel tubes (SUS316, 1/2 inch in outer diameter) and PFA tubes (tetrafluoroetylene-perfluoroalkylvinylether copolymer, 1/2 inch in outer diameter), which were connected through stainless steel joints and valves partially made of Kel-F (polychlorotrifluoroethylene) tip (Swagelok). The temperature of the drying vessel was controlled by silicone oil heated in an oil bath with a magnetic stirrer. The vacuum atmosphere was generated by a rotary vacuum pump (ULVAC KIKO, Inc., GLD-136C).

A cold trap (Pyrex glass) cooled with liquid nitrogen was used to prevent volatiles from entering the pump. The pressure of the vacuum line was monitored by a Pirani gauge.

The starting precursor fluorides, LiF (Aldrich, purity > 99.99%), NaF (Wako Pure Chemical Industries, purity 99%), FeF_2 (Aldrich, purity > 98%), MnF_2 (Aldrich, purity > 98%), and FeF_3 (Aldrich, purity > 97%) were dried under vacuum at 120 °C and stored in the Ar-filled glove box. Tetrahydrofuran (THF; dehydrated, Wako Pure Chemical Industries, water content < 10 ppm, stabilizer-free), Li metal (Aldrich, 99.95%), and Na metal (Aldrich, 99.95%) were used as purchased. Acetylene black (AB; Wako Pure Chemical Industries, purity > 99.99%) and poly(tetrafluoroethylene) (PTFE; Aldrich; particle size: ca. 200 μm) were dried under vacuum at 120 °C. The FSA salts, Li[FSA] (Kishida Chemical, purity > 99%) and Na[FSA] (Mitsubishi Materials Electronic Chemicals, purity > 99%) as well as an FSA IL, $[C_2C_1im][FSA]$ (Kanto Chemical, purity > 99.9%), were dried under vacuum at 80 °C for 24 h. Battery-grade 1 M $LiPF_6$/EC:DMC (1:1 in volume, Kishida Chemical; EC: ethylene carbonate; DMC: dimethyl carbonate; water content < 30 ppm) and 1 M $NaPF_6$/EC:DMC (1:1 in volume, Kishida Chemical) organic electrolytes were used as purchased.

2.2 Synthesis of active materials

The target material was prepared by ball milling under different conditions in a planetary ball mill (Planetary Micro Mill PULVERISETTE 7 premium line, Fritsch, 20 mL grinding bowl with zirconia inner wall and 3 mm diameter zirconia balls). Figure 2-3

shows the schematic diagram of an airtight ball-milling bowl. The heat treatment was conducted loading ball-milled sample in a stainless-steel tube with a diameter of 29 mm (Asahi Rika Seisakusho Co., Ltd.; ARF-20KC) under different conditions (Figure 2-4). More detailed preparation methods will be described in each chapter.

2.3 Characterization techniques

2.3.1 X-ray diffraction (XRD)

In this study, XRD was used to analyze the crystal structure and lattice parameters of the samples involved in this study. The XRD patterns of the powder samples at different synthetic stages were recorded in the Bragg−Brentano geometry using a Rigaku MiniFlex diffractometer with Ni-filtered Cu *K*α radiation (λ = 1.5418 Å, 30 kV and 10 mA) and a D/tex Ultra250 Si-strip high-speed detector.

The *ex-situ* synchrotron XRD patterns of the electrodes at different charged and discharged states were recorded in the BL5S2 of the Aichi Synchrotron Radiation Center equipped with a PILATUS 100 K two-dimensional detector. Each electrode was prepared by disassembling the cell followed by rinsing with tetrahydrofuran (THF, Wako Pure Chemical Industries, water content ≤10 ppm), and vacuum-drying for 1 d at room temperature. After washing and drying, the electrode materials were further sealed in Lindeman glass capillaries.

The obtained XRD patterns were further refined with the Rietveld refinement using the GSAS or FullProf data analysis software to obtain the structural parameters of the samples. The corresponding crystal structures were visualized by the VESTA program.

2.3.2 Field emission scanning electron microscopy (SEM) and energy dispersive X-ray spectroscopy (EDX)

In this study, SEM and EDX were used to analyze the particle size, morphological characteristics, and elemental distribution of the samples. The SEM and EDX images of the powder samples were identified *via* field-emission SEM (Hitachi SU-8020, Japan) and EDX mapping (Horiba EMAXEvolution X-max, Japan).

2.3.3 Specific surface area measurement with Brunauer−Emmett−Teller (BET) method

Nitrogen adsorption analysis was performed using Tristar II 3020 equipment (Shimadzu Corp.) to evaluate the BET surface area of the powder samples.

2.3.4 Atomic absorption spectrometry (AAS) and inductively coupled plasma−atomic emission spectrometry (ICP-AES)

The metal element contents in some powder samples were determined by AAS (Hitachi Z-2300) and ICP-AES (Hitachi PS3520VDD II) after dissolution with sulfuric, nitric, and perchloric acids.

2.3.5 X-ray absorption fine structure (XAFS) measurement

All the XAFS data were measured using the BL-3 at the Synchrotron Radiation Center, Ritsumeikan University at room temperature. The Fe *K*-edge spectra were obtained in a transmission mode. The electrode powder (~ 7 mg) after charging and discharging was thoroughly mixed with boron nitride (250 mg) and then molded into pellets with 10 mm in diameter by pressurizing at 60 MPa for 5 min using a dry pellet pressing die set (tungsten carbide, Figure 2-5) and a hydraulic press machine.

2.3.6 X-ray photoelectron spectroscopy (XPS)

Bonding states in materials were analyzed by a JEOL JPS-9010 XPS instrument with Mg*K*α radiation (λ = 9.89 Å, 10 kV−10 mA) after Ar etching at an ion energy of 400 eV for different times according to the samples. The obtained spectra were fitted using an analytical software (SpecSurf, ver. 1.8.3.7, JEOL, Ltd). The electrodes were handled using the same preparation method for the *ex-situ* XRD measurements.

2.4 Electrochemical measurements

2.4.1 Electrode preparation and cell configurations

For the enhanced conductivity of the materials, the target compounds were further ball-milled with acetylene black (AB) (Wako Pure Chemical Industries) and heated by the same method as its preparation. The positive electrode sheet was prepared by thoroughly

mixing the compound of active material/AB with poly(tetrafluoroethylene) (PTFE, Aldrich, Inc.; particle size: ca. 200 μm) binder using an agate mortar and an agate pestle. The sheet was pressed onto a fresh Al mesh (13 mm in diameter) to prepare the working electrode with a loading mass of ~ 3 mg cm^{-2} (see schematic drawing in Figure 2-5).

Coin cells (2032-type), as shown in Figure 2-6, were assembled in the Ar-filled glove box to examine the electrochemical performance of each material. The Li metal disk fixed on the stainless steel (SUS316L) plate current collector, or Na metal disk fixed on the Al plate current collector was used as the counter electrode. A glass fiber filter (Whatman, GF/A; 16 mm in diameter and 260 μm in thickness) was used as a separator after being immersed in IL electrolyte under vacuum at 80 °C for 12 h.

2.4.2 Galvanostatic charge-discharge test

All the electrochemical data (i.e., charge-discharge, rate capability, and cyclability tests) were obtained by an HJ-SD8 charge-discharge system (Hokuto Denko). The prepared coin cells were maintained at an open circuit voltage for more than 5 h prior to the measurements. The operating temperature was controlled using an ESPEC SU221 environmental test chamber.

The charge-discharge curves and cyclability of the working electrode were measured by galvanostatic charge-discharge at a certain current density. Galvanostatic intermittent titration techniques (GITTs) were employed to assess the overpotentials by

repeatedly monitoring the voltage relaxation in the open-circuit state immediately after charging or discharging to a certain voltage.

2.4.3 Cyclic voltammetry (CV) and electrochemical impedance spectroscopy (EIS)

CV and EIS measurements were performed using a VSP potentiostat (Bio-Logic). Half cells were assembled for CV measurements. All EIS data were recorded over a frequency range from 10 mHz to 100 kHz with a perturbation amplitude of 10 mV in symmetric cells and half-cells (both are 2032 coin-type). Symmetric cells were assembled for the EIS spectra at different temperatures (25 °C and 90 °C), in which the two charged electrodes (state of charges (SOCs): 50%) were obtained in half-cells using IL electrolyte at 25 °C and 90 °C, respectively. The half-cells were assembled for EIS spectra during cycling, which were measured at 3.2 V during the charging step (SOCs: 50%) of the *n*th cycle (n = 0, 1, 10, 20, 50, and 100) when the half-cells were cycled at a rate of 100 mA g^{-1}.

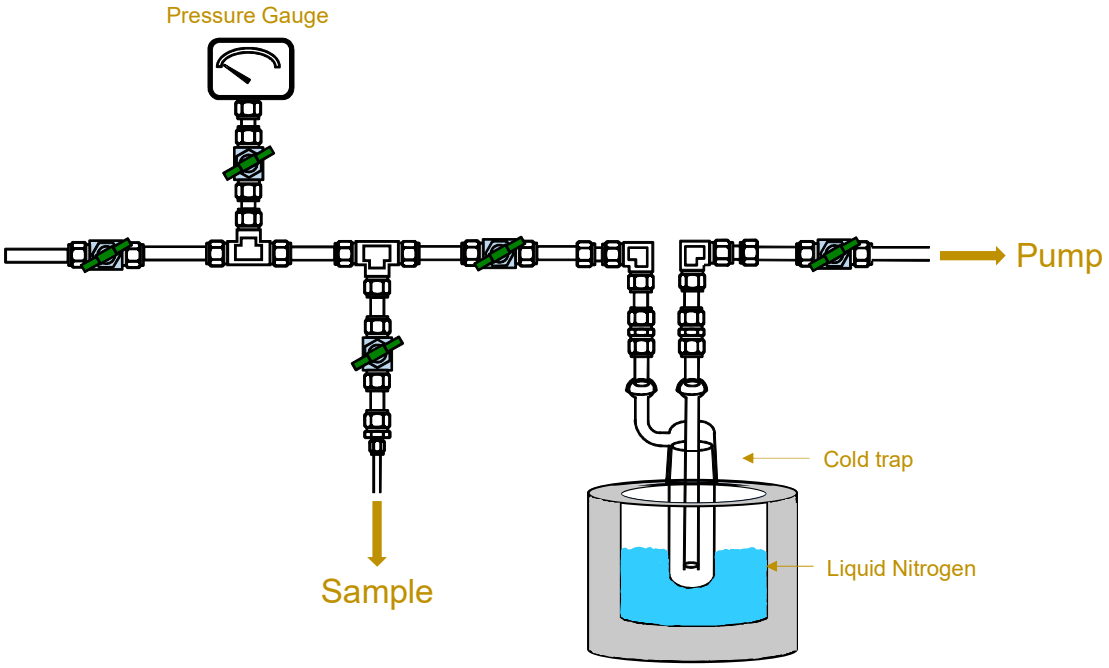

Figure 2-1 Schematic diagram of the vacuum line [1].

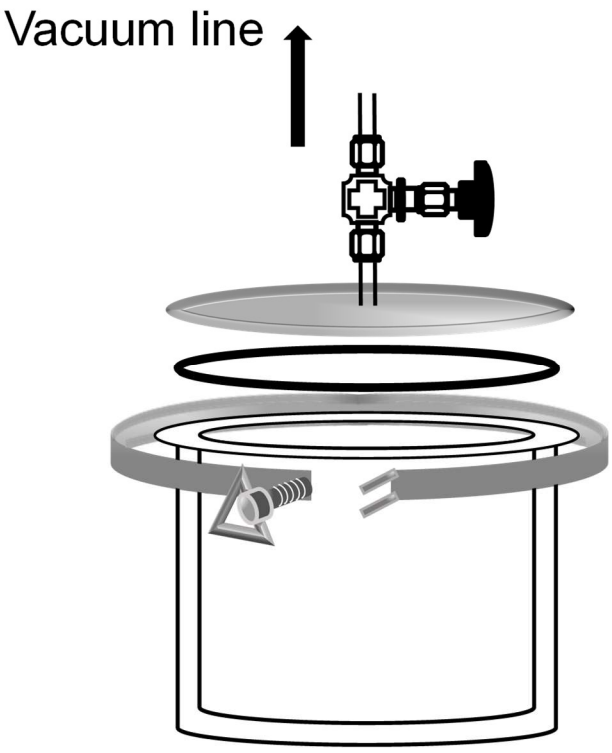

Figure 2-2 Schematic diagram of the drying vessel.

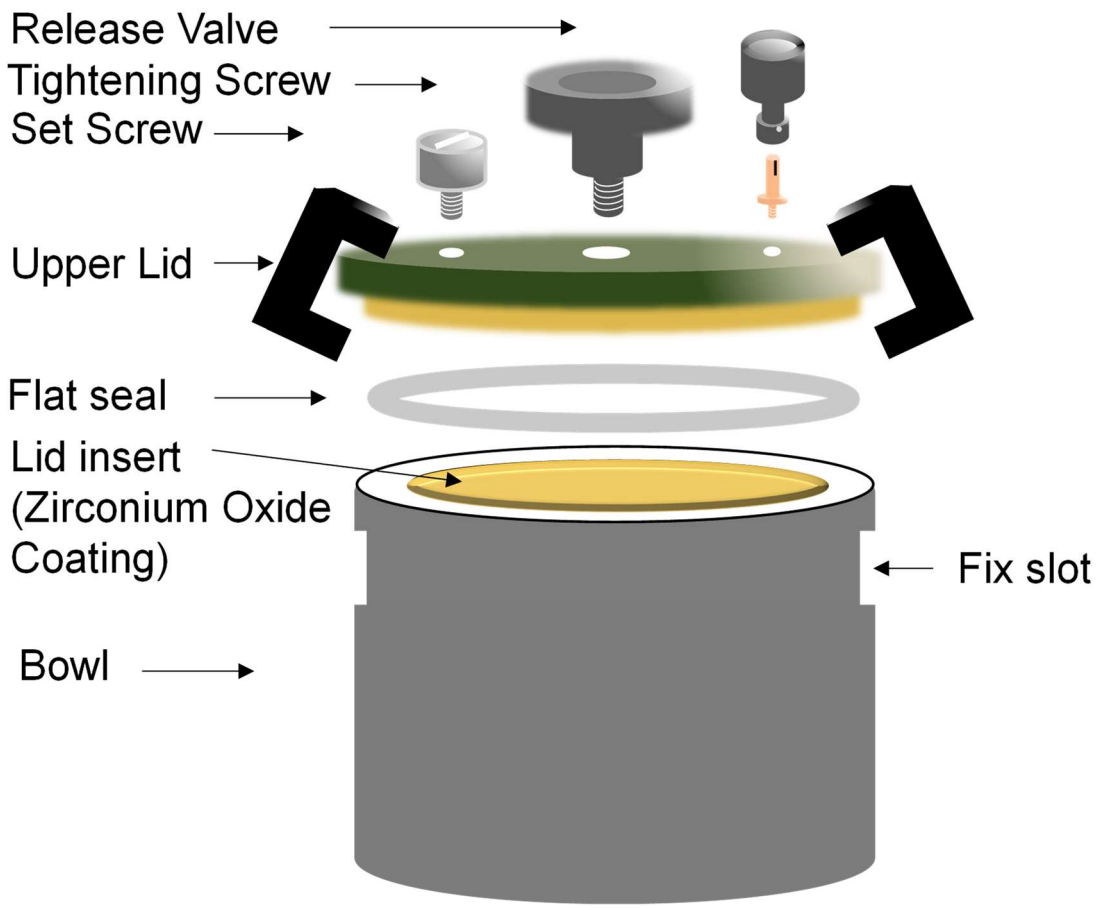

Figure 2-3 Schematic diagram of an airtight ball-milling bowl.

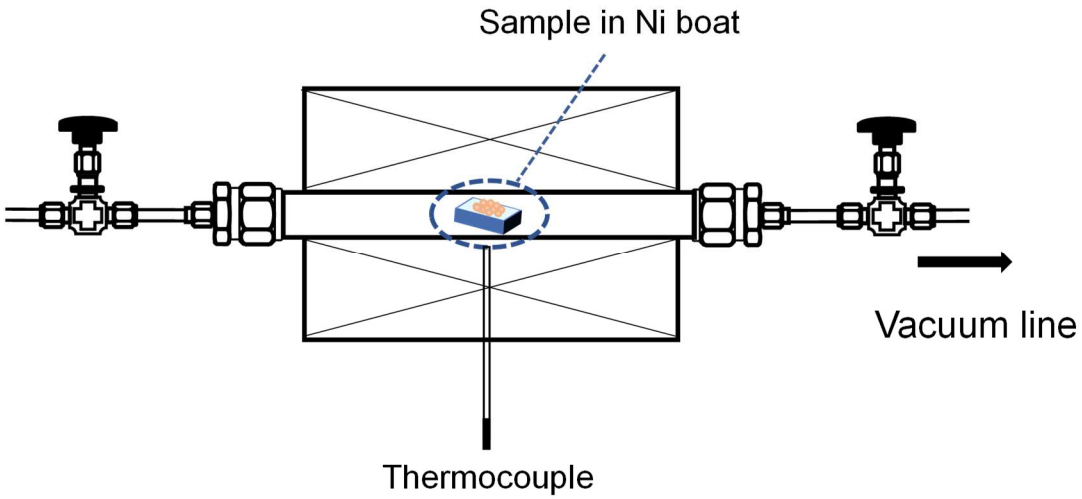

Figure 2-4 Schematic diagram of the heating equipment [2].

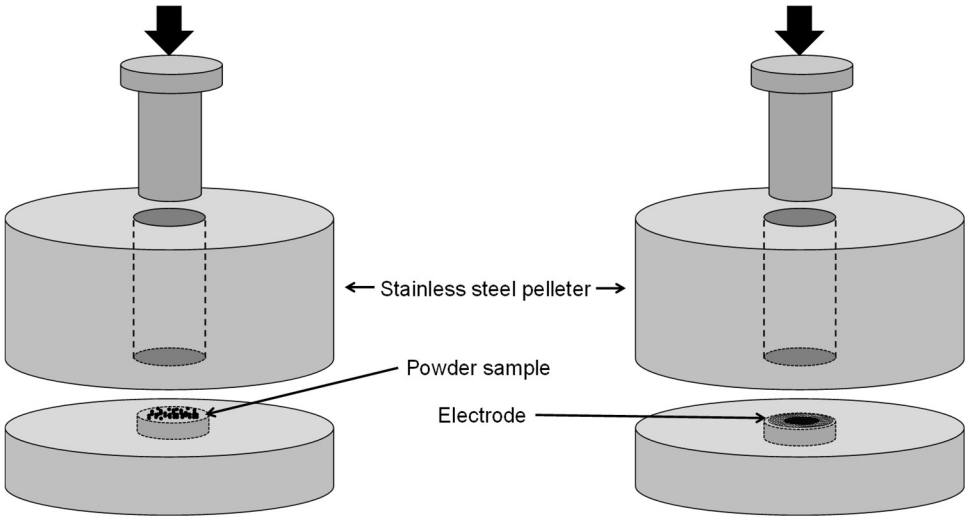

Figure 2-5 Schematic diagram of the mold used to make pellet and electrode.

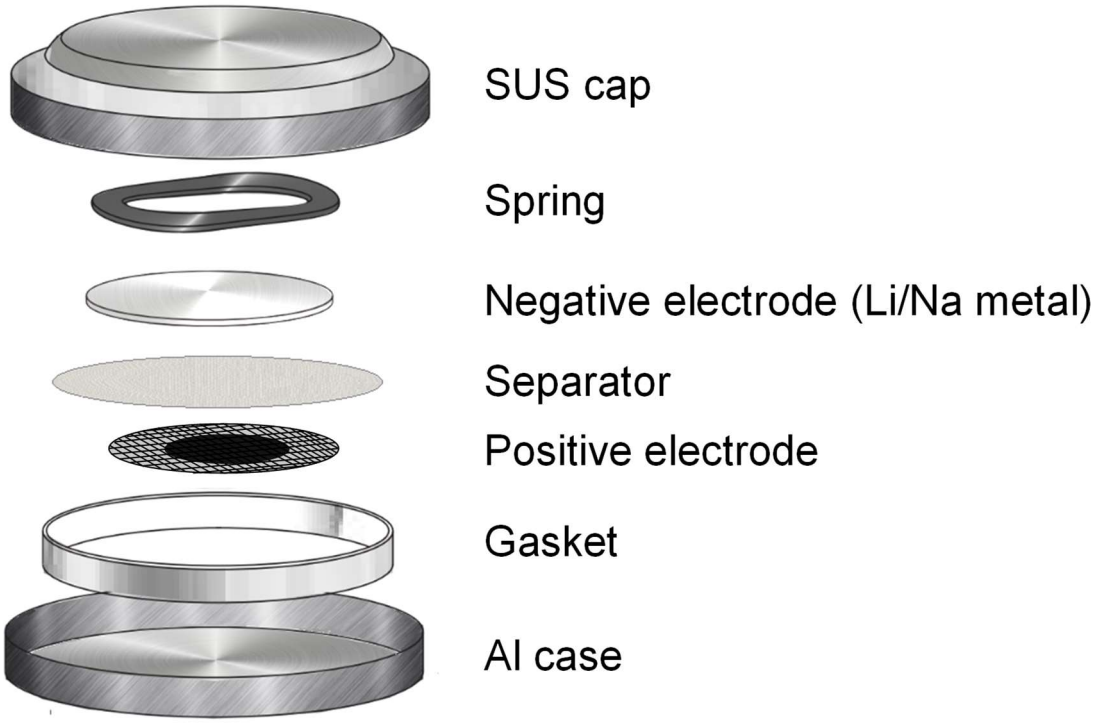

Figure 2-6 A schematic diagram of coin cell 2032 [1].

References

[1] J. Hwang, PhD Thesis, Graduate School of Energy Science, Kyoto University (2019).

[2] S. Jitto, Master Thesis, Graduate School of Energy Science, Kyoto University (2019).

Chapter 3

Exploration on the Reaction Mechanism of Trirutile $LiFe_2F_6$ in Li-ion Batteries

3.1 Introduction

The discharge mechanism of FeF_3 as the positive electrode for the LIBs have been extensively studied through both experimental and theoretical techniques [1-5], in which the intermediate phase $Li_x[Fe^{II}_{1-x}Fe^{III}_x]F_3$ before the full reduction of FeF_3 to LiF and Fe were suggested to exist. Furthermore, trirutile $Li_{0.5}FeF_3$ (hereafter, denoted as $LiFe_2F_6$) was calculated to possess a stable crystal structure in the space group of $P4_2/mnm$ [6, 7], attaining theoretical capacities of 115 mAh g^{-1} based on one-electron reaction. As such, understanding the electrochemical behavior of $LiFe_2F_6$ as a positive electrode material of LIBs would significantly aid the verification of its reaction pathway in the Li−Fe−F system [5, 8, 9].

Table 3-1 lists selected reports on trirutile $LiFe_2F_6$ in previous studies. The trirutile structure embodied by $Li[A^{II}B^{III}]F_6$ (A, B = transition metals) was first envisaged by Viebahn *et al*. [10, 11], whose work was ensued by the direct synthesis of trirutile $LiFe_2F_6$ and related X-ray and magnetic structural studies [6, 12-14]. The trirutile structure, also regarded as the triple rutile-type structure, has been found to bear a structural semblance to related rutile structures, especially along the crystallographic *c*-axis on X-ray diffraction (XRD) patterns [7]. Some reports regarded trirutile $LiFe_2F_6$ as an intermediate

phase [3-5], however, none of them directly clarified the electrochemical behavior of this phase. In fact, due to the restrictive synthesis conditions of trirutile $LiFe_2F_6$, literature on its electrochemical mechanisms as the positive electrode materials for LIBs remains scarce. Attempts to analyze the electrochemical behavior of $LiFe_2F_6$ have been made by Liao *et al*. *via* reporting the synthesis of $LiFe_2F_6$ with a disordered rutile structure, where the superlattice peak along the *c*-axis disappeared, exposing the formation of a cationdisordered rutile structure [15, 16]. Electrochemical measurements performed on this disordered $LiFe_2F_6$ in LIBs showed a limited capacity in the $LiPF_6$/EC:DEC (1:2 in volume) organic electrolyte. During the initial discharge and the subsequent initial charge, expansion and contraction of the *a*-axis and the *c*-axis, respectively, were observed, suggesting the reversible intercalation of Li^+ within the tunnels of rutile $Li_{1+x}Fe_2F_6$ ($0 < x < 0.6$) in a single-phase region, which is contrary to the reaction pathway of FeF_3 alongside Li [3, 5]. A later theoretical study on the phase transition of trirutile $LiFe_2F_6$ as well as Li^+ insertion/extraction in trirutile $Li_xFe_2F_6$ suggested that the trirutile phase exists as a stable phase in the space group of $P4_2/mnm$ as 0.25 Li^+ insertion/extraction into/from trirutile $LiFe_2F_6$ [17]. However, it is worth mentioning that the DFT calculations of the atomic structure and electronic states of $Li_xFe_2F_6$ revealed that trirutile $LiFe_2F_6$ has the most stable structure in the space group of $P4_2nm$. As $x > 1$, $Li_xFe_2F_6$ is energetically unstable, and a conversion reaction occurs in this region [18, 19]. It is noteworthy that, in a technical sense, no experimental report has been presented to illuminate the phase evolution of ordered trirutile $LiFe_2F_6$ as the positive electrode for Li-ion batteries. In this

vein, such an attempt would not only mark a leap toward understanding the electrochemical behavior of $LiFe_2F_6$ but also bear academic significance in the augmentation of this class of materials.

Herein, for the first time, the electrochemical performance of ordered trirutile $LiFe_2F_6$ was assessed at elevated temperatures of 90 °C with the aid of the thermally stable Li[FSA][C_2C_1im][FSA] IL electrolyte. Ordered trirutile $LiFe_2F_6$ was prepared through high-energy ball milling followed by heat treatment at 400 °C. Further, a series of charge−discharge tests and a GITT were performed on the prepared electrode with the Li[FSA][C_2C_1im][FSA] IL. The particle size, morphology of the prepared powder sample, phase evolution, and Fe oxidation states of the resulting electrode samples are rationalized using the results of SEM, nitrogen adsorption, synchrotron XRD and XAFS measurements. The inherent performance of $LiFe_2F_6$ is discussed in detail in the context of the data obtained.

3.2 Experimental

In a typical preparation of $LiFe_2F_6$, 0.467 g of LiF (0.01800 mol), 1.689 g of FeF_2 (0.01800 mol), and 2.029 g of FeF_3 (0.01798 mol) were weighed and loaded in an airtight bowl with a zirconia inner wall under a dry argon atmosphere. The mixture was then ball-milled in a planetary ball mill at 600 rpm for 6 h with zirconia balls. After the ball milling process, the bowl was opened in the glovebox, and the sample was transferred into a nickel boat. The nickel boat was thereafter placed in an airtight stainless steel pipe with a

valve in the glovebox, and the entire pipe was transferred to the vacuum line. Heat treatment was then performed on the sample at 400 °C for 17 h under vacuum. A target sample of $LiFe_2F_6$ (approximately 3.7 g) was recovered from the nickel boat in the glovebox.

The XRD patterns of $LiFe_2F_6$ at different synthetic stages were recorded in the Bragg−Brentano geometry using a Rigaku MiniFlex diffractometer. Structural parameters were refined with the Rietveld method by curve-fitting using the GSAS and FullProf data analysis software [20, 21]. The crystal structure was visualized by the VESTA program [22]. The morphology of the prepared $LiFe_2F_6$ powder was identified via field-emission SEM. Elemental distribution over the $LiFe_2F_6$ electrode was obtained by EDX mapping. Nitrogen adsorption analysis was performed using Tristar II 3020 equipment to evaluate the Brunauer−Emmett−Teller (BET) surface area of the $LiFe_2F_6$ sample. The Li and Fe contents in $LiFe_2F_6$ were determined after dissolution with sulfuric, nitric, and perchloric acids by AAS and ICPAES, respectively. Synchrotron XRD patterns of $LiFe_2F_6$ at different charge−discharge stages were recorded in the BL5S2 of the Aichi Synchrotron Radiation Center equipped with a PILATUS 100 K two-dimensional detector with a wavelength of 0.9997 Å. The electrode powders washed with THF and vacuum-dried at room temperature were sealed in Lindeman glass capillaries. For XAFS measurements, the electrode powders after charging and discharging (~ 6.7 mg) were thoroughly mixed with boron nitride (250 mg) and then molded into pellets. All the XAFS data were measured using the BL-3 at the Synchrotron Radiation Center, Ritsumeikan

University, at room temperature. The Fe *K*-edge spectra were obtained in a transmission mode.

The $LiFe_2F_6$/AB composite (75:25 in weight) was prepared by dry ball milling at 600 rpm for one hour with the same synthesis process as $LiFe_2F_6$. The powdered $LiFe_2F_6$/AB composite was recovered in the glovebox and heated at 300 °C for 6 h under vacuum. The PTFE binder was thoroughly mixed with the $LiFe_2F_6$/AB composite ($LiFe_2F_6$/AB:PTFE = 95:5 in weight) using an agate mortar and a pestle to form a homogeneous electrode sheet. The sheet was pressed onto a fresh Al mesh (13 mm in diameter) to prepare the test electrode with a loading mass of ~ 3 mg cm^{-2}.

Coin cells (2032-type) were assembled in the Ar-filled glovebox with the $LiFe_2F_6$ working electrode, the Li[FSA]-[C_2C_1im][FSA] (30:70 in mol) IL electrolyte, and the Li metal disk counter electrode fixed on a stainless steel (SUS316L) plate current collector. The glass microfiber separator was immersed in the IL electrolyte under vacuum at 90 °C for 12 h prior to cell assembling.

All the electrochemical data were obtained by an HJ-SD8 charge-discharge system. The charge−discharge curves and cycling performance of the working electrode were measured by galvanostatic charge−discharge tests. In this study, the rate of 1 C corresponds to 115 mAh g^{-1}, and the capacity of the positive electrode is shown as a value per weight (in grams) of $LiFe_2F_6$. GITT curves were employed to assess the overpotentials by repeatedly monitoring the voltage relaxation in the open-circuit state immediately after charging or discharging to a certain voltage.

3.3 Results and discussion

To understand the structure of the ball milled mixture, XRD patterns were taken before (B-$LiFe_2F_6$) and after heat treatment at 400 °C (BH-$LiFe_2F_6$) as shown in Figure 3-1a. In the case of B-$LiFe_2F_6$ (Figure 3-1a (1)), several broad peaks are discerned. However, the strongest peak, which can be assigned to residual FeF_3 (space group: $R\bar{3}c$ [2, 3]), appears around 23.94°, suggesting that the ball milling process alone does not complete the reaction. The other peaks observed are assignable to the rutile-type $LiFe_2F_6$ where cations are disordered. It is noted that the two characteristic superlattice peaks attributed to trirutile $LiFe_2F_6$ are not detected at 19.26° and 21.46° before the heat treatment. Upon heat treatment at 400 °C (Figure 3-1a (2)), the diffraction peaks of BH-$LiFe_2F_6$ become significantly sharper while the peak assignable to FeF_3 is observed to disappear. Rietveld refinement employed for further analysis of BH-$LiFe_2F_6$ indicated that the XRD pattern is well-fitted within the parameters of the trirutile $LiFe_2F_6$ structure in the $P4_2/mnm$ space group (R_p = 1.30%, R_{wp} = 2.04%) as highlighted by the fitting results (Figure 3-1b) and summarized in Table 3-2. The $LiFe_2F_6$ trirutile structure is characterized by edge-sharing among Li^+F_6, $Fe^{2+}F_6$, and $Fe^{3+}F_6$ octahedra, with a distinct Li^+-Fe^{2+}-Fe^{3+} cationic ordering along the *c*-axis (Figure 3-1c). This creates tunnels that facilitate Li^+ extraction/insertion from/into the host lattice [7, 10, 14, 23]. Also, the minor peaks of an impurity FeF_2 phase, seen in the diffraction patterns (Figure 3-1a (2) and b), are verified as 2.53 wt% by the Rietveld analysis.

To enhance the electronic conductivity of the composite electrode, the heat-treated crystalline $LiFe_2F_6$ sample was ball-milled with AB in the weight ratio of $LiFe_2F_6$:AB = 75:25 [24]. XRD patterns of the repeatedly ball milled sample with AB were obtained before (RB-$LiFe_2F_6$) and after heat treatment at 300 °C (RBH-$LiFe_2F_6$) as shown in Figure 3-1a (3) and (4). Upon ball milling with AB (Figure 3-1a (3)), the diffraction peaks of RB-$LiFe_2F_6$ appear to be broadened and weakened, featuring two rather dim characteristic peaks of the trirutile structure around 20°. However, these characteristic peaks appear again after the heat treatment of the RB-$LiFe_2F_6$ sample, suggesting the recovery of the Li and Fe ordering (Figure 3-1a (4), RBH-$LiFe_2F_6$). A comparison between the XRD patterns of BH-$LiFe_2F_6$ and RBH-$LiFe_2F_6$ (Figure 3-1a (2) and (4)) indicates that, except for the broadening of the diffraction peaks caused by a decrease in crystallite size, the introduction of AB creates no significant changes in the structure and impurity phases (see Figure 3-1d,e for the SEM images). Although partial reduction of Fe(III) at 300 °C under vacuum may occur with the presence of AB in this study (cf. the heat treatment of FeF_3 with carbon materials under an Ar flow) [25], the amount of FeF_2 produced by the reduction is considered to be very limited according to the subsequent Rietveld refinement of the RBH-$LiFe_2F_6$ electrode (see below).

SEM measurements were additionally performed to examine the morphological properties of the pristine BH-$LiFe_2F_6$ and RBH-$LiFe_2F_6$ samples as shown in Figure 3-1d,e. Results indicate that both samples are composed of micro-sized secondary particles, which are agglomerates of the nanoparticles. The pristine BH-$LiFe_2F_6$ has larger particles

(above 100 nm) than RBH-$LiFe_2F_6$ (above 50 nm), indicating that the ball milling process further ground the $LiFe_2F_6$ particles and that nanosized AB particles were introduced. The homogeneous distribution of Fe and F atoms in micrometer order is also confirmed by EDX analysis (Figure 3-1d,e). The increase in BET surface area from 3.1 $m^2\ g^{-1}$ (BH-$LiFe_2F_6$) to 88 $m^2\ g^{-1}$ (RBH-$LiFe_2F_6$) also indicates the decrease in $LiFe_2F_6$ particle size, but the contribution of AB surface area seems to be more significant (AB only: 53 $m^2\ g^{-1}$ before ball milling and 327 $m^2\ g^{-1}$ after ball milling; see Figure 3-1f and Table 3-3). The Li and Fe contents in the BH-$LiFe_2F_6$ were determined by the AAS and ICP-AES analyzers. The BH-$LiFe_2F_6$ sample has Li and Fe contents of 3.0 and 47.5 wt%, respectively, which are close to the theoretical values of 3.0 and 48.0 wt%.

To investigate the electrochemical behavior of the RBH-$LiFe_2F_6$ electrode, galvanostatic charge−discharge tests were performed on a half-cell configuration comprising a Li metal counter electrode and Li[FSA]-[C_2C_1im][FSA] (30:70 in mol) IL electrolyte. Two different cutoff voltage ranges of 3.2−4.3 and 2.5−4.3 V were set at a rate of 0.2 C (~ 20 mA g^{-1}) and a temperature of 90 °C as highlighted by the charge-discharge curves and the corresponding differential capacity versus potential (dQ/dV) plots shown in Figure 3-2. For the 3.2−4.3 V voltage range (Figure 3-2a), an initial charge capacity of 122 mAh g^{-1} characterized by a plateau around 4.0 V is obtained. The three initial cycles exhibit superposing discharge curves that plateau around 3.9 V, attaining a reversible capacity of 89.8 mAh g^{-1}. As will be explained hereinafter, the plateau corresponds to the extraction/insertion of one-electron Li^+ from/into the host trirutile

lattice [15]. The ratio of the discharge capacity to the theoretical capacity indicates that 0.78 Li^+ extraction/insertion is achieved during the charge-discharge process. The Coulombic efficiency of the three initial cycles increases as the cycles progress from 73.5% in the first cycle to 87.8% in the third cycle. The irreversible capacity observed is ascribed to the side reactions to which the oxidative decomposition of the electrolyte mostly contributes [26]. The corresponding dQ/dV curves of the first three cycles are shown in Figure 3-2b. There is only a pair of redox peaks in the cutoff voltage of 3.2−4.3 V, which is attributed to Li^+ extraction/insertion from/into the host trirutile lattice occurring at 4.01 and 3.95 V, respectively. No significant changes are noted in the positions of the redox couple throughout the first three cycles, demonstrating the high reversibility of the charge-discharge process in the 3.2−4.3 V voltage range.

To explore the electrochemical properties of $LiFe_2F_6$ at a lower potential, charge-discharge profiles were obtained in the 2.5−4.3 V voltage range (Figure 3-2c). During the initial cycle, a discharge capacity of 174.5 mAh g^{-1} marked by a plateau around 3.0 V is obtained. As elucidated by previous reports on the reaction mechanism of FeF_3 and confirmed by synchrotron XRD results hereafter, the plateau appearing around 3.0 V during the discharge process is considered to originate from the conversion reaction of $LiFe_2F_6$ to LiF and FeF_2 (see below for further discussion) [5]. The capacity in the cutoff voltage of 3.2−2.5 V region is 91.1 mAh g^{-1}, equivalent to a 0.80 Li^+ reaction. In the second charging process, a change in the curve gradient is observed from 3.0 V onward with a short plateau appearing around 4.1 V. The specific voltages where these plateaus

are located are further confirmed by the corresponding dQ/dV plots (Figure 3-2d). When the lower cutoff voltage is reduced to 2.5 V, significant changes in both the peak intensity and position of the two redox couples are observed during the first two cycles. However, almost no changes are observed as the cycle progress from the second to the third cycle. The reaction mechanisms represented by these peaks will be later expounded in the context of GITT and synchrotron XRD results.

The cycling tests of RBH-$LiFe_2F_6$ for the two voltage ranges (3.2−4.3 and 2.5−4.3 V) were examined using Li[FSA]-[C_2C_1im][FSA] IL electrolyte at 90 °C, and their resulting discharge capacity and Coulombic efficiency as a function of cycle number are shown in Figure 3-3. In the voltage range of 3.2−4.3 V (Figure 3-3a,b), the discharge capacity decreases from 89.8 to 85.7 mAh g^{-1} over the first 20 cycles, delivering a capacity retention of 95.4%. A high retention suggests that the ordered $LiFe_2F_6$ trirutile structure can be reversibly delithated/lithiated in the IL electrolyte at 90 °C. The Coulombic efficiency increases as the cycle progress, reaching more than 90% after 10 cycles. However, it is seen to fluctuate around 90% after 25 cycles. This can be ascribed to the occurrence of the aforementioned side reactions [26]. In the case of the 2.5−4.3 V voltage range (Figure 3-3c,d), the discharge capacity is seen to fade during the first five cycles, thereafter flattening to become almost constant. A capacity retention of 81.5% is achieved at the 20th cycle (142.3 mAh g^{-1}). The initial Coulombic efficiency is noted to be over 100% because the amount of Li^+ insertion exceeds the one Li^+ extraction from $LiFe_2F_6$ in this cutoff voltage. Upon subsequent cycling, the Coulombic efficiency

gradually decreases from 95.9% in the second cycle but later increases with further cycling, resulting in 96.1% at the 20th cycle. Although the cycle performance of trirutile $LiFe_2F_6$ in the IL electrolyte at 90 °C is not superior to other reported state-of-the-art positive electrode materials that include some iron fluorides [27-30], this cycle performance suggests that this electrode material and the electrolyte as well as operation temperature are suitable for clarifying the reaction mechanism of trirutile $LiFe_2F_6$.

To discern the effects of temperature on electrode behavior, galvanostatic charge−discharge tests in the voltage ranges of 3.2−4.3 and 2.5−4.3 V were performed on a Li[FSA]-[C_2C_1im][FSA] IL electrolyte and 1 M $LiPF_6$/EC:DMC organic electrolyte at 25 °C (Figure 3-4). In the IL electrolyte (Figure 3-4a,b), RBH-$LiFe_2F_6$ exhibits poor electrochemical activity with no distinct plateaus appearing in both the voltage ranges at 25 °C. Similar electrochemical activities are observed in the organic electrolyte as shown in Figure 3-4c,d. These results suggest that the ionic conductivities of $LiFe_2F_6$ and charge transfer at the interphase thwart its activation toward Li^+ extraction/insertion in these conditions, which is limited by the large secondary particles. These results indicate that the activity of $LiFe_2F_6$ is brought out by the operation at elevated temperature.

To gain insight into the reaction mechanisms of ordered trirutile $LiFe_2F_6$, GITT measurements were performed through repeated monitoring of the voltage relaxation during the open-circuit state after charging or discharging to certain cell voltages. Figure 3-5 shows the GITT curves of the RBH-$LiFe_2F_6$ electrode during the first two cycles in the 3.2−4.3 and 2.5−4.3 V voltage ranges at 90 °C. During the first charge in the cutoff

voltage of 3.2−4.3 V (Figure 3-5a), the open-circuit voltage after relaxation gradually increases, indicating the occurrence of a single-phase reaction. A capacity of 26.3 mAh g^{-1} is eventually attained representing the extraction of 0.22 Li^+ from trirutile $LiFe_2F_6$. Upon reaching 4.0 V, the relaxation potential remains virtually unchanged, which is an indication of a two-phase reaction occurring between the trirutile phase and another phase. At the end of the initial charging process, a gradual increase in the open-circuit voltage after relaxation is observed, suggesting the occurrence of another single-phase reaction. During the subsequent discharge process, a plateau corresponding to the two-phase reaction can be observed around 3.9 V, indicating the same reaction path for the delithiation and lithiation processes. The second cycle of the GITT test essentially yields the same charge−discharge curve as the first cycle, demonstrating the same reaction mechanisms and the high reversibility of delithiation/lithiation processes within the trirutile structure in the cutoff voltage of 3.2−4.3 V. Drastic changes on the voltage profiles are seen to occur when the lower cutoff voltage is reduced (Figure 3-5b). When the initial discharge is extended to 2.5 V, further lithiation beyond $LiFe_2F_6$ is perceived to occur, as manifested by the two sloping regions in the galvanostatic charge-discharge in Figure 3-2c. The overpotential in the corresponding GITT curve increases as the lithiation continues. During the second charging process, a sloping curve is observed between 3.2 and 3.9 V, followed by a constant open-circuit voltage of 3.9 V. This is a manifestation that the phase evolution is different from the one in the initial discharging. The absence of a plateau around 3.0 V, previously observed in the first discharge,

indicates the poor recovery from the phases formed at 2.5 V to trirutile $LiFe_2F_6$. Moreover, the second discharge process is marked by a limited capacity for the plateau region at 3.9 V and a large overpotential below 3.2 V. A combination of the voltage profiles from the galvanostatic charge−discharge and GITT measurements (Figures 3-2 and 3-5) reveals that extending the discharge process to 2.5 V causes a poor reversible reaction, which results in incomplete recovery of trirutile $LiFe_2F_6$ after undergoing the electrochemical reaction in this voltage region.

To verify the phase transformation and reaction mechanism during the initial charge−discharge and second charge processes, synchrotron XRD and XAFS analyses were carried out on trirutile $LiFe_2F_6$ as summarized in Figure 3-6. The states analyzed by XRD and XAFS are given by the corresponding-colored points in the potential−time profile (Figure 3-6a). Figure 3-6b presents the XRD patterns of the RBH-$LiFe_2F_6$ electrode in the different charge/discharge states. The peak at 2θ = 11.68°, which is allocated to the PTFE binder [31, 32], appears throughout the entire delithiation and lithiation process. As can be seen in the crystallographic data and refinement results obtained through Rietveld refinement (Table 3-4), the diffraction peaks of the pristine electrode (pattern 1) are mostly indexed to trirutile $LiFe_2F_6$ in the space group of $P4_2/mnm$, which corroborates with the data of the as-prepared material (Table 3-2) and confirms that the crystal structure of $LiFe_2F_6$ (pattern 1) is not influenced by AB and PTFE in the formation of the electrode composite. A slight amount of FeF_2 (3.63 wt%) is observed as confirmed in the sample as prepared (Figure 3-1a (2) and b). After the initial charge

(pattern 2), some residual peaks of trirutile $LiFe_2F_6$ are still observed in their original positions, conforming with the insufficient practical capacity (78% based on the theoretical capacity) indicated by the electrochemical data (Figure 3-2a). The new peak appearing at 15.45° is designated as the strongest diffraction peak of FeF_3 (012 diffraction) belonging to the space group of $R\bar{3}c$. This shows that, during the initial charge process, FeF_3 is generated from the residual FeF_2 and LiF leftover from the preparation process of trirutile $LiFe_2F_6$. This side reaction is consistent with the results drawn from the phase evolution of LiF/FeF_2 in previous works [26, 33]. In addition, shifts in several diffraction peaks belonging to trirutile $LiFe_2F_6$ are observed. Some diffraction peaks are seen to shift to lower angles while others appear to shift to higher angles, revealing the formation of a new tetragonal phase (tetragonal I). Further analysis by the Rietveld refinement (Table 3-4) elaborates that these diffraction peaks can be indexed as a tetragonal phase with larger *a* and smaller *c* lattice parameters than those of original trirutile $LiFe_2F_6$, suggesting that delithiation results in isotropic lattice expansion to the *a* and *b*-axes and shrinkage along the *c*-axis. The unit cell volume after delithiation is 201.650(3) $Å^3$, which corresponds to a 1.09% decrease from the initial unit cell volume of the trirutile structure. This volume change is smaller than that of typical positive electrode materials during the process of Li^+ extraction, such as $LiCoO_2$ (~ 2.0%, SOC = 0.5) [34, 35], spineltype $LiMn_2O_4$ (~ 3.2%, SOC = 0.5) [36, 37], and olivine-type $LiFePO_4$ (~ 4.6%, SOC = 0.5) [38, 39], although the amount of Li^+ extracted is limited in the present case. After discharging to 3.2 V (pattern 3), the diffraction peaks shift back

to their original positions, suggesting that the trirutile structure is recovered at 3.2 V by inserting ~ 0.78 Li^+ into the original sites. The disappearance of the FeF_3 diffraction peak after discharging to 3.2 V indicates that lithiation of the FeF_3 phase results in trirutile $LiFe_2F_6$ or FeF_2 with LiF. This insertion reaction has been widely investigated among the FeF_3 electrodes [4, 5] and the LiF/FeF_2 nanocomposites [26]. A further discharge to 2.5 V (pattern 4) results in the decrease of the trirutile $LiFe_2F_6$ phase according to Rietveld refinement (8.48 wt%) and the increase of the rutile FeF_2 and LiF to the main phases (Table 3-4). This observation indicates that the conversion reaction from the trirutile $LiFe_2F_6$ phase to FeF_2 and LiF occurs at 2.5 V after the disintegration of the trirutile phase. A similar behavior is recognized in the previous report on the Li−Fe−F system, regardless of the starting phase [5]. However, the conversion reaction is not complete, and the trirutile $LiFe_2F_6$ phase exists as an impurity. After the second charge to 4.3 V (pattern 5), the XRD pattern observed can be indexed as a tetragonal structure with the residual peaks belonging to FeF_2. These peaks (denoted as tetragonal II) show slight shifts compared to those of the initial trirutile structure (pattern 1) and tetragonal I after the initial charge (pattern 2), suggesting the trirutile structure is no longer recovered by delithiation from the two-phase mixture of rutile FeF_2 and LiF. Further verification by Rietveld refinement identified tetragonal II as the disordered trirutile structure (the Li site is occupied by Fe with an occupancy of 0.374(4)). The corresponding crystallographic data (Table 3-4) indicate that the second delithiation results in a 0.83% increase in the *a* lattice parameter and a 1.20% decrease in the *c* lattice parameter, causing a 0.45% overall increase in

volume from the initial trirutile $LiFe_2F_6$. No peaks of FeF_3 are observed after the second charge, suggesting that FeF_3 is not formed from FeF_2 and LiF, as will be hereafter confirmed by XAFS data. Figure 3-6c shows the schematic drawing of the changes in XRD patterns from trirutile $LiFe_2F_6$ to tetragonal I and tetragonal II (patterns 1, 2, and 5), where each peak is identified according to the crystallographic data by Rietveld refinement. The position shifts and intensity changes of the diffraction peaks as a result of delithiation can be visually tracked from the initial trirutile structure to the resulting tetragonal I and II structures.

The Fe *K*-edge XAFS spectra provide information on the oxidation state and local structure around Fe atoms of the RBH-$LiFe_2F_6$ electrode that occurs during the charge−discharge. Figure 3-6d demonstrates the Fe *K*-edge X-ray absorption near edge structure (XANES) spectra of the RBH-$LiFe_2F_6$ electrode at different states of charge and discharge. The absorption edge evolution indicates the variation of Fe oxidation states [26, 40-42]. After the initial charging process to 4.3 V ($x \sim 0.78$ in $Li_{1-x}Fe_2F_6$), the main Fe *K*-edge absorption edge exhibits a high-energy shift to the edge of Fe^{3+}-containing reference compounds (spectra 1 and 2) [26, 43], suggesting the oxidation from Fe^{2+} to Fe^{3+}. After the subsequent discharge to 3.2 V (spectrum 3), the Fe *K*-edge position returns to the original position. The spectral overlap between the pristine state (spectrum 1) and the state after discharge to 3.2 V (spectrum 3) indicates the reversibility of the topotactic Li^+ extraction/insertion from/into the trirutile structure. After further discharge to 2.5 V (spectrum 4), the shift of Fe *K*-edge to a further lower energy corresponding to the Fe^{2+}

edge position is observed [5, 43, 44], evidencing the reduction to Fe^{2+} during this discharge process. After the second charge to 4.3 V (spectrum 5), the XANES spectrum does not overlap with the one obtained after the initial charge (spectrum 2), suggesting less Li^+ extraction from the host lattice of the trirutile structure. To investigate the local structure of Fe atoms in the RBH-$LiFe_2F_6$ electrode under different charging and discharging states, Fe *K*-edge extended X-ray absorption fine-structure spectroscopy (EXAFS) analysis was employed as shown by the Fourier transform (FT) spectra in Figure 3-6e. The FT EXAFS spectra significantly change by the initial charging (spectra 1 and 2) and return to the original form after discharging to 3.2 V (spectrum 3). The first peak centered around 1.56 Å corresponds to the contribution of the Fe−F first-neighboring shell, whereas the second peak appearing around 3.28 Å represents the contribution of the Fe−Fe first-neighboring shell [26]. The primary Fe−F distance is enlarged to 1.63 Å after the discharging process to 2.5 V (spectrum 4), which agrees with the reduction from Fe^{3+} to Fe^{2+} as suggested by the aforementioned XANES analysis. The disagreement of the curves after recharging to 4.3 V (spectrum 5) and the state of the first charge (spectrum 2) are further evidence the higher oxidation at the second delithiated state.

Figure 3-7 illustrates the phase evolution of the RBH-$LiFe_2F_6$ electrode at 90 °C during the charge−discharge processes. In the voltage range of 3.2−4.3 V, the topotactic Li^+ extraction/insertion reversibly occurs between trirutile $LiFe_2F_6$ and tetragonal I $Li_{1-x}Fe_2F_6$ through a single-phase reaction and a two-phase reaction around 4.0 V,

attaining a discharge capacity corresponding to $x = 0.78$. This process is constrained at 25 °C but is stable over 20 cycles at 90 °C. An extension of the lower cutoff voltage to 2.5 V triggers the conversion reaction from trirutile $LiFe_2F_6$ to a mixture of rutile FeF_2 and LiF without forming another intermediate phase, which presumably results from the absence of Li^+ accessible sites in the trirutile structure. During the second charging process, the sloping region starting from 3.1 V may be related to the reconstruction of the trirutile structure considering the corresponding plateau formed during the discharge process. However, this reaction seems to be incomplete and is followed by a short plateau at 4.1 V. According to the XRD analysis, this two-phase reaction leads to the formation of the tetragonal II phase with a disordered trirutile structure. These observations suggest the poor recovery of trirutile $LiFe_2F_6$ from the completely destructed state after the conversion reaction to LiF and FeF_2. The second charge capacity is 159.5 mAh g^{-1} (Figure 3-2c), corresponding to less Li^+ extraction ($x \sim 0.7$ for $Li_{1-x}Fe_2F_6$) compared to the first charge capacity ($x \sim 0.78$ for $Li_{1-x}Fe_2F_6$), thus providing evidence of the lower delithiated state after the second charge process. Previous publications have described the formation of trirutile $LiFe_2F_6$ as an intermediate obtained by inserting Li^+ into a FeF_3 framework with a distorted rhenium trioxide structure ($R\bar{3}c$) [4, 5]. However, there is no sign of rhombohedral FeF_3 ($R\bar{3}c$) after the second charge to 4.3 V, contrary to other reports that confirmed the reconversion from LiF/FeF_2 to FeF_3 at 25 °C [26, 33, 45]. Such a difference indicates that the starting material strongly affects the phase evolution in the Li−Fe−F systems at 90 °C. In the overall conversion chemistry of FeF_3 at room

temperature, the role of trirutile $LiFe_2F_6$ is considered to be limited because its electrochemical activity is extremely low. The difficulty of reconversion during charging also indicates little contribution of $LiFe_2F_6$ once it is converted to LiF and FeF_2 during the first discharging.

3.4 Conclusions

Although the electrochemical behavior of $LiFe_2F_6$ with a trirutile structure has been long-pursued in literature, a functional charge−discharge mechanism has not been reported. In this study, the charge−discharge properties of trirutile $LiFe_2F_6$ were investigated at an intermediate temperature operation that facilitates various processes in batteries. Trirutile $LiFe_2F_6$ was prepared by high-energy ball milling combined with heat treatment. Its electrochemical properties in the Li[FSA]-[C_2C_1im][FSA] IL electrolyte were examined at 90 °C as the room-temperature performance was very limited. At a rate of 0.2 C (1 C = 115 mAh g^{-1}), the trirutile RBH-$LiFe_2F_6$ electrode exhibits a reversible capacity of 89.8 mAh g^{-1} in the cutoff voltage of 3.2−4.3 V, corresponding to the reversible extraction and insertion of 0.78 Li^+. After 20 consecutive cycles, this reversible capacity slightly decreases to 85.7 mAh g^{-1}, delivering a capacity retention of 95.4%. The extension of the lower cutoff voltage to 2.5 V triggers another electrochemical reaction, giving an initial discharge capacity of 174.5 mAh g^{-1}. Over 20 cycles, this value fades to 142.3 mAh g^{-1}, leading to a capacity retention of 81.5%. Additional GITT tests and synchrotron XRD analyses revealed the reversibility of topotactic Li^+ extraction/insertion in the voltage

region of 3.2−4.3 V through a two-phase mode between the trirutile phase and tetragonal I phase. Further lithiation at the lower voltage of 2.5 V gives rise to a conversion reaction to LiF and rutile FeF_2. During the second charge from 2.5 V, reconversion from LiF and FeF_2 resulted in the Li/Fe disordered trirutile phase with low crystallinity instead of ordered trirutile $LiFe_2F_6$ or rhombohedral FeF_3, indicating the ordered trirutile phase did not recover after undergoing the conversion process.

This work provides comprehensive insights into the overall reaction mechanisms of trirutile $LiFe_2F_6$ as a positive electrode for Li-ion batteries to expand the information space of the Li−Fe−F phase transformation. It also proposes new ideas for developing high-energy density LIBs based on the reversible topotactic reactions of the trirutile structural framework. Further modification of the trirutile materials with different transition metals or fabrication techniques is expected to extend their practical use, including operation at room temperature. The synthesis of completely pure trirutile $LiFe_2F_6$ was not achieved by high-energy ball milling and heat treatment in this study, as residual amounts of FeF_2 and LiF were found throughout the process. As such, improvement in the synthetic procedure will be in the scope of future studies.

Table 3-1 Summary of major milestones in trirutile $LiFe_2F_6$ studies.

Year	Existent form	Preparation method	Analysis	Crystallographic and electrochemical properties
1967 [10]	Trirutile $Li[A^{II}B^{III}]F_6$ (A, B = transition metals) (S. G. $P4_2/mnm$)	Solid-state reaction	XRD	$LiCoFeF_6$: a = 4.670 Å, c = 9.180 Å $LiNiFeF_6$: a = 4.630 Å, c = 9.150 Å
1968 [12]	Trirutile $LiFe_2F_6$ (S. G. $P4_2/mnm$)	Solid-state reaction	XRD	a = 4.673 Å, c = 9.290 Å
1969 [11]	Trirutile $Li[A^{II}B^{III}]F_6$ (A, B = transition metals) (S. G. $P4_2/mnm$)	Solid-state reaction	XRD	$LiCoFeF_6$: a = 4.665 Å, c = 9.159 Å $LiNiFeF_6$: a = 4.648 Å, c = 9.128 Å $LiZnFeF_6$: a = 4.671 Å, c = 9.154 Å
1971 [13]	Trirutile $LiFe_2F_6$	Solid-state reaction	Mössbauer spectroscopy	None
1972 [6]	Trirutile $LiFe_2F_6$ (S. G. $P4_2/mnm$)	Solid-state reaction	Neutron diffraction, Magnetic structure	a = 4.673 Å, c = 9.290 Å
1972 [14]	Trirutile $LiFe_2F_6$ (S. G. $P4_2/mnm$)	Solid-state reaction	Neutron diffraction, Magnetic structure	a = 4.673 Å, c = 9.290 Å
1988 [7]	Trirutile $LiFe_2F_6$ (S. G. $P4_2nm$)	Hydrothermal synthesis	Single-crystal XRD	a = 4.679 Å, c = 9.324 Å
2008 [3]	Trirutile $LiFe_2F_6$ (S. G. $P4_2/mnm$)	Calculated intermediate phase upon Li^+ insertion into FeF_3	DFT calculation for the Li-Fe-F system	a = 4.756 Å, c = 9.339 Å
2009 [4]	Trirutile $LiFe_2F_6$ (S. G. $P4_2/mnm$)	Intermediate phase upon Li^+ insert into FeF_3	XRD, PDF analysis and solid-state NMR	The intermediate phase appears during discharge of a FeF_3 electrode at 127 mAh g^{-1}
2010 [15]	Disordered rutile $LiFe_2F_6$ and $Li_{1.2}FeF_{6.2}$ (S. G. $P4_2/mnm$)	Solid-state reaction	XRD, In-situ XRD	81% capacity retention after 17 cycles between 2.5−4.0 V (102 mAh g^{-1} for initial discharge capacity) and 62% capacity retention after 14 cycles between 2.0−4.5 V (126 mAh g^{-1} for initial discharge capacity)
2010 [16]	Disordered rutile $Li_{1.2}FeF_{6.2}$ (S. G. $P4_2/mnm$)	Solid-state reaction	XRD, Mössbauer spectra	a = 4.717 Å, c = 3.127 Å
2013[17]	Trirutile $LiFe_2F_6$ (S. G. $P4_2/mnm$)	Calculation	DFT calculation	a = 4.726 Å, c = 9.222 Å
2016 [5]	Trirutile $LiFe_2F_6$	Intermediate phase upon Li^+ insert into FeF_3	In-situ XAS, DFT calculation	The intermediate phases appear during discharge and charge of a FeF_3 electrode at 1/6 C
2017 [18]	Trirutile $LiFe_2F_6$ (S. G. $P4_2nm$)	Calculation	DFT calculation	a = 4.666 Å, c = 9.253 Å
2019 [19]	Trirutile $LiFe_2F_6$ (S. G. $P4_2nm$)	Calculated intermediate phase upon Li^+ insert into FeF_3	DFT calculation, Density of states (DOS) analysis, XANES analysis	a = 4.725 Å, c = 9.383 Å

Table 3-2 Crystallographic parameters of BH-$LiFe_2F_6$ obtained from Rietveld refinement.

Refinement results for BH-$LiFe_2F_6$ (S.G. $P4_2/mnm$) R_p = 1.30%, R_{wp} = 2.04%

a = 4.6799(6) Å			c = 9.3161(1) Å		V = 204.041(7) Å^3	
Atom	Wyckoff symbol	x	y	z	Biso / Å^2	Occup.
Li	2*a*	0	0	0	0.5	1
Fe	4*e*	0	0	0.3333(5)	0.5	1
F1	4*f*	0.2916(3)	0.2916(3)	0	0.5	1
F2	8*j*	0.3031(2)	0.3031(2)	0.3360(1)	0.5	1

Table 3-3 BET surface areas of (i) AB without ball-milling, (ii) AB after ball-milling, (iii) BH-$LiFe_2F_6$ after heat treatment at 400 °C and (iv) RBH-$LiFe_2F_6$ after heat treatment at 300 °C (see Figure 3-1f for the corresponding nitrogen absorption isotherms).

Sample	BET Surface Area / $m^2\ g^{-1}$
(i) AB without ball-milling	53
(ii) AB after ball-milling	327
(iii) BH-$LiFe_2F_6$	3.1
(iv) RBH-$LiFe_2F_6$	88

Table 3-4 Crystallographic parameters of the trirutile $LiFe_2F_6$, Tetragonal I, Discharge state and Tetragonal II appearing during the charge-discharge process of the RBH-$LiFe_2F_6$ electrode obtained by Rietveld refinement.

Refinement results for trirutile $LiFe_2F_6$ (Pattern 1)[a] (S.G. $P4_2/mnm$) R_p = 2.27%, R_{wp} = 3.65%

a = 4.6798(1) Å			c = 9.3095(4) Å		V = 203.879(1) Å^3	
Atom	Wyckoff symbol	x	y	z	Biso / Å^2	Occup.
Li	2*a*	0	0	0	0.5	1
Fe	4*e*	0	0	0.3321(2)	0.5	1
F1	4*f*	0.2894(6)	0.2894(6)	0	0.5	1
F2	8*j*	0.3098(4)	0.3098(4)	0.3424(4)	0.5	1

Refinement results for Tetragonal I (Pattern 2)[b] (S.G. $P4_2/mnm$) R_p = 2.61%, R_{wp} = 3.70%

a = 4.7718(3) Å			c = 8.8557(1) Å		V = 201.650(3) Å^3	
Atom	Wyckoff symbol	x	y	z	Biso / Å^2	Occup.
Fe	4*e*	0	0	0.3277(3)	0.5	1
F1	4*f*	0.3038(1)	0.3038(1)	0	0.5	1
F2	8*j*	0.2974(7)	0.2974(7)	0.3382(8)	0.5	1

Refinement results for Discharge state (Pattern 4)[c] (S.G. $P4_2/mnm$) R_p = 2.64%, R_{wp} = 4.21%

a = 4.7029(2) Å			c = 3.2586(3) Å		V = 72.074(8) Å^3	
Atom	Wyckoff symbol	x	y	z	Biso / Å^2	Occup.
Fe	2*a*	0	0	0	0.5	1
F	4*f*	0.3065(4)	0.3065(4)	0	0.5	1

Refinement results for Tetragonal II (Pattern 5)[d] (S.G. $P4_2/mnm$) R_p = 2.76%, R_{wp} = 4.01%

a = 4.7189(2) Å			c = 9.1972(8) Å		V = 204.799(2) Å^3	
Atom	Wyckoff symbol	x	y	z	Biso / Å^2	Occup.
Fe1	2*a*	0	0	0	0.5	0.374(4)
Fe2	4*e*	0	0	0.3375(4)	0.5	0.834(5)
F1	4*f*	0.3265(1)	0.3265(1)	0	0.5	1
F2	8*j*	0.3278(7)	0.3278(7)	0.3471(9)	0.5	1

[a]FeF_2 ($P4_2/mnm$) is considered to be an impurity phase. [b]Trirutile $LiFe_2F_6$ ($P4_2/mnm$), FeF_2 ($P4_2/mnm$), and FeF_3 ($R\bar{3}c$) are considered to be impurity phases. Li is not included in the analysis. [c]Trirutile $LiFe_2F_6$ ($P4_2/mnm$) is considered to be an impurity phase. [d]FeF_2 ($P4_2/mnm$) is considered to be an impurity phase. Li is not included in the analysis.

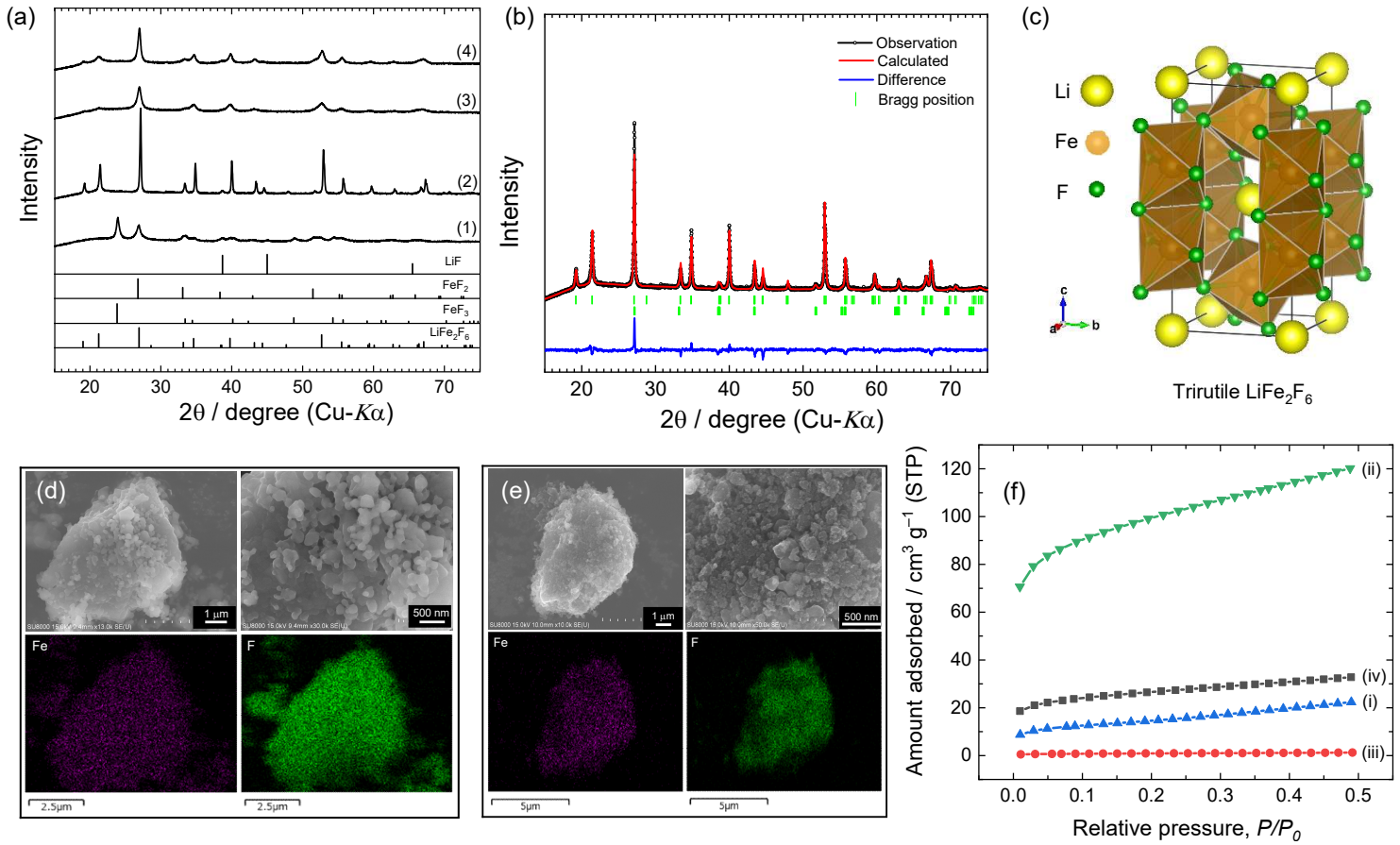

Figure 3-1 (a) X-ray diffraction patterns of the $LiFe_2F_6$ samples at different synthetic stages: (1) B-$LiFe_2F_6$ obtained by ball-milling of LiF, FeF_2, and FeF_3. (2) BH-$LiFe_2F_6$ obtained by heating the sample of (1) at 400 °C for 17 h. (3) RB-$LiFe_2F_6$ obtained by ball-milling the sample of (2) with AB, and (4) RBH-$LiFe_2F_6$ obtained by heating the sample of (3) at 300 °C for 6 h. B, H, and R denote ball-milling, heating, and repeated treatment, respectively. (b) XRD patterns and Rietveld refinement results of

the BH-$LiFe_2F_6$ sample. (c) The refined crystal structure. See Table 3-2 for the crystallographic data. Morphological properties (SEM and EDX) of the (d) pristine BH-$LiFe_2F_6$ and (e) RBH-$LiFe_2F_6$. (f) Nitrogen adsorption isotherms of (i) AB without ball-milling, (ii) AB after ball-milling, (iii) BH-$LiFe_2F_6$ after heat treatment at 400 °C, and (iv) RBH-$LiFe_2F_6$ after heat treatment at 300 °C.

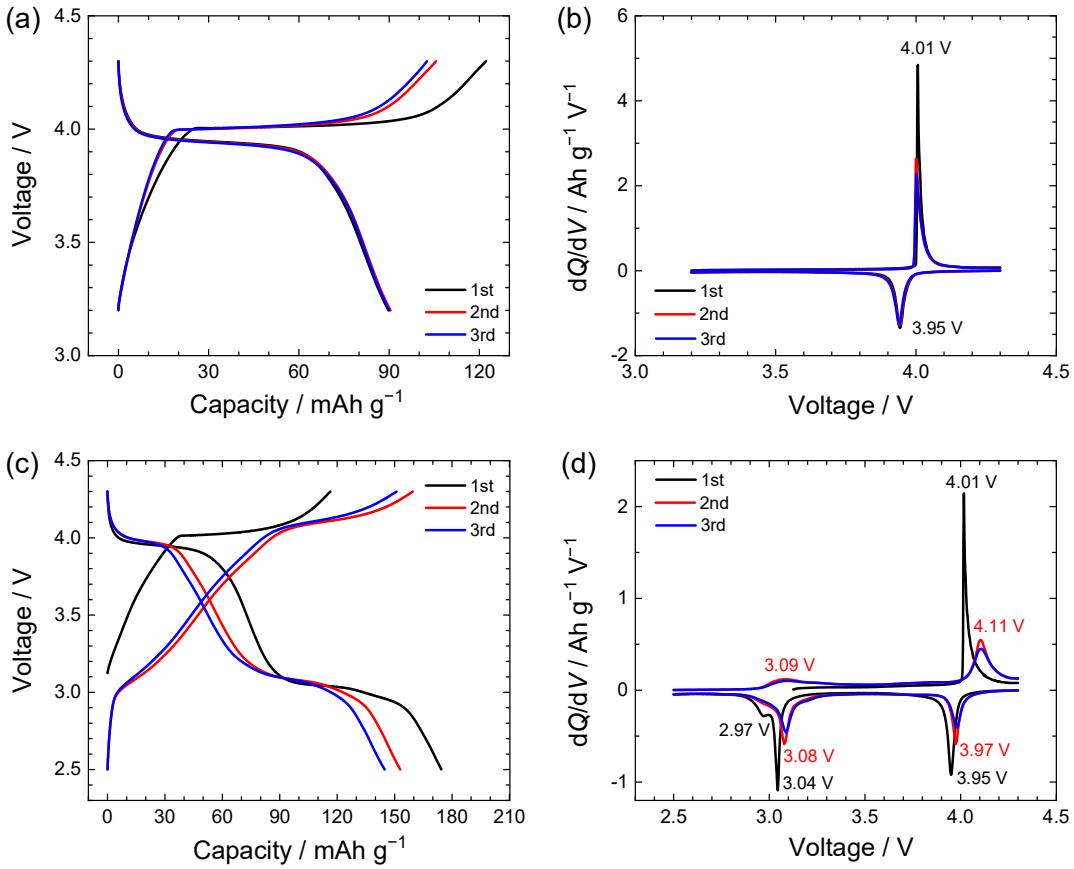

Figure 3-2 Charge-discharge curves of the trirutile $LiFe_2F_6$ electrode evaluated using ionic liquid Li[FSA]-[C_2C_1im][FSA] (30:70 in mol) at 90 °C. (a) The first three cycles between 3.2−4.3 V and (b) the corresponding dQ/dV plots of the charge-discharge curves in (a) during the initial three cycles. (c) The first three cycles between 2.5−4.3 V and (d) the corresponding dQ/dV plots of the charge-discharge curves in (c) during the initial three cycles.

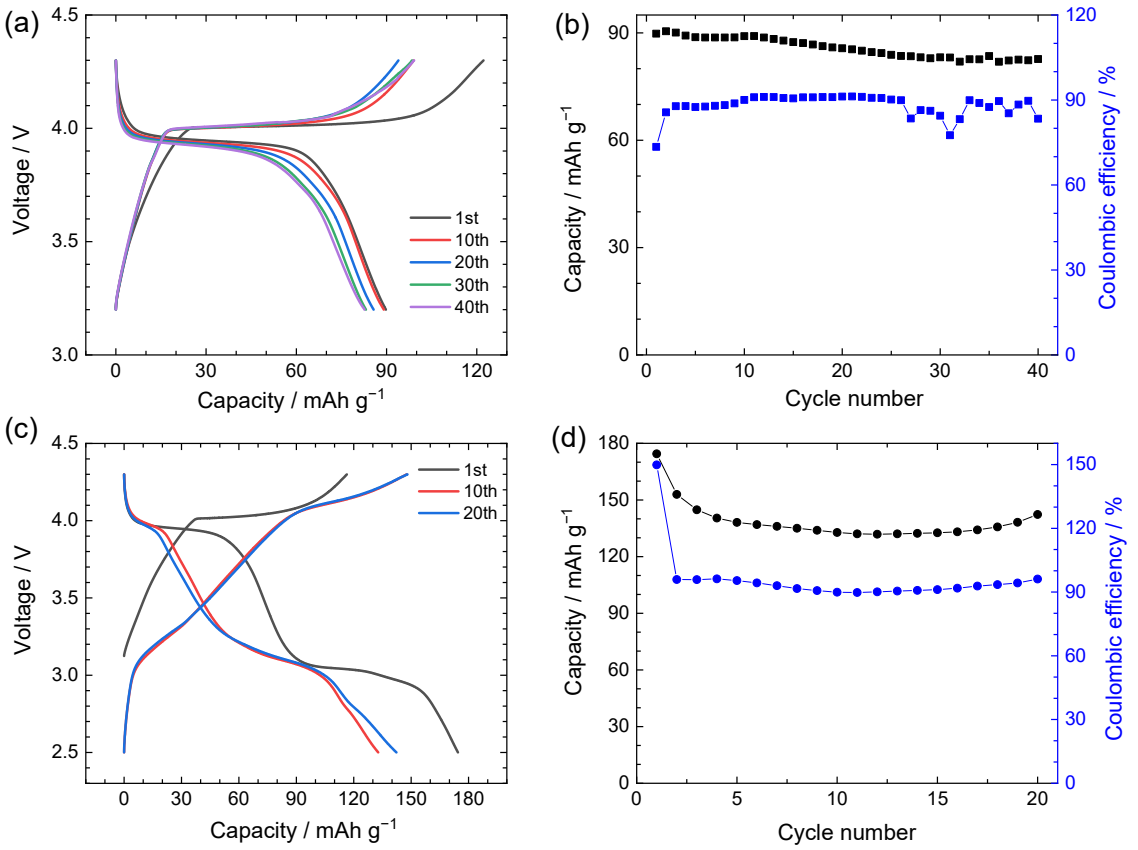

Figure 3-3 Cyclability of the trirutile $LiFe_2F_6$ evaluated using ionic liquid Li[FSA]-[C_2C_1im][FSA] (30:70 in mol) at 90 °C. (a) Charge-discharge curves and (b) cycle plot for 40 cycles in the cut-off voltage of 3.2−4.3 V. (c) Charge-discharge curves and (d) cycle plot for 20 cycles in the cut-off voltage of 2.5−4.3 V.

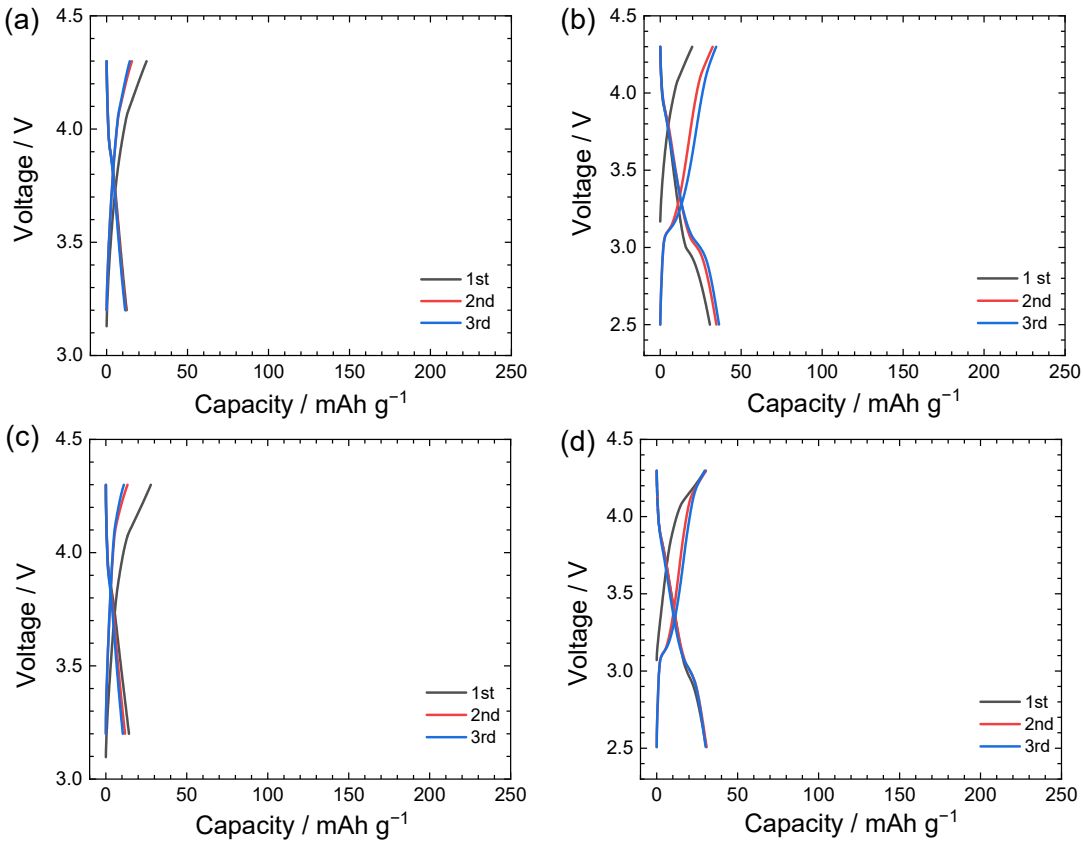

Figure 3-4 Charge-discharge curves of the trirutile $LiFe_2F_6$ electrode at room temperature (25 °C). Li[FSA]-[C_2C_1im][FSA] (30:70 in mol) in the cut-off voltages between (a) 3.2−4.3 V and (b) 2.5−4.3 V. 1 M $LiPF_6$/EC:DMC organic electrolyte in the cut-off voltages between (c) 3.2−4.3 V and (d) 2.5−4.3 V.

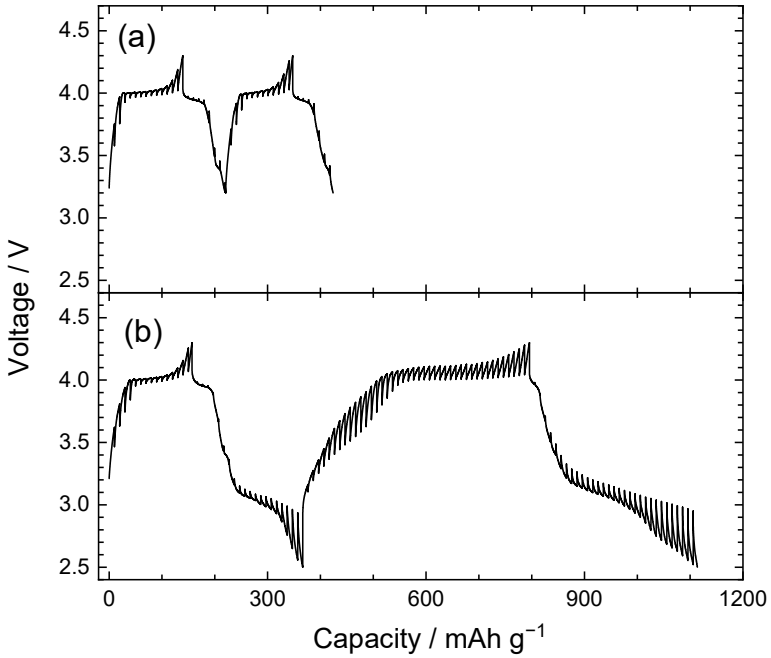

Figure 3-5 The GITT curves of the RBH-$LiFe_2F_6$ electrode in the voltage ranges of (a) 3.2−4.3 V and (b) 2.5−4.3 V at 90 °C. The GITT conditions were conducted via a stepwise polarization at 50 mA g^{-1} for 1 h and thereafter left at an open-circuit state for 2.5 h.

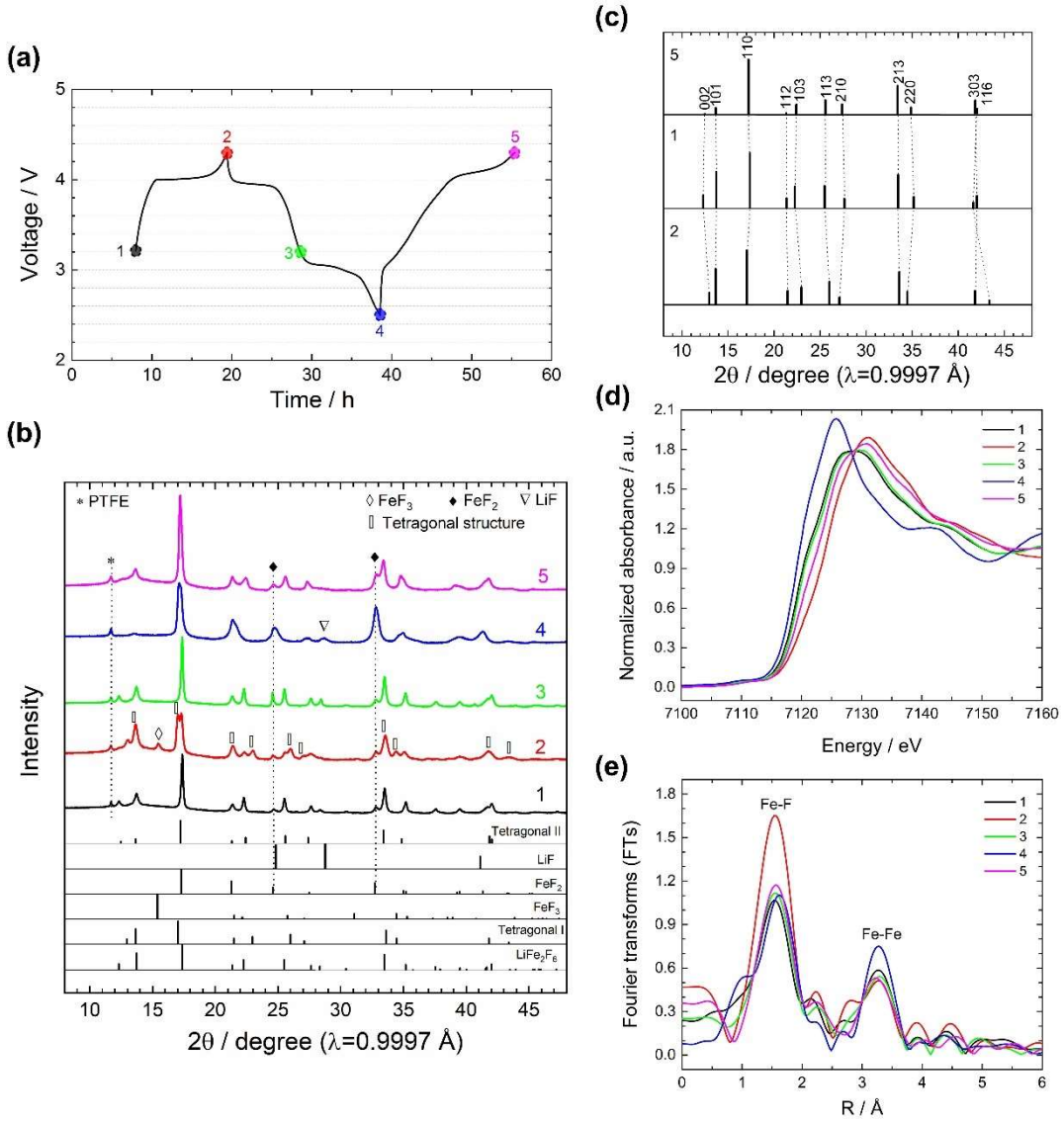

Figure 3-6 Synchrotron XRD and XAFS results for the RBH-$LiFe_2F_6$ electrode. (a) Charge and discharge voltage profiles taken at a cur-rent density equivalent to 0.1 C (1 C = 115 mAh g^{-1}) at 90 °C: (1) Pristine state, (2) initial charge to 4.3 V, (3) half discharge to 3.2 V, (4) full discharge to 2.5 V, and (5) second charge to 4.3 V. (b) Synchrotron XRD patterns (λ = 0.9997 Å) of the charged and discharged samples. (c) Simulated XRD peak positions of the trirutile $LiFe_2F_6$ (Pattern 1), Tetragonal I phase obtained after the initial charge (Pattern 2), and Tetragonal II phase obtained after the second charge (Pattern 5). The original XRD patterns are shown in (b). (d) Fe *K*-edge XANES spectra and (e) corresponding Fourier transforms of the EXAFS oscillations.

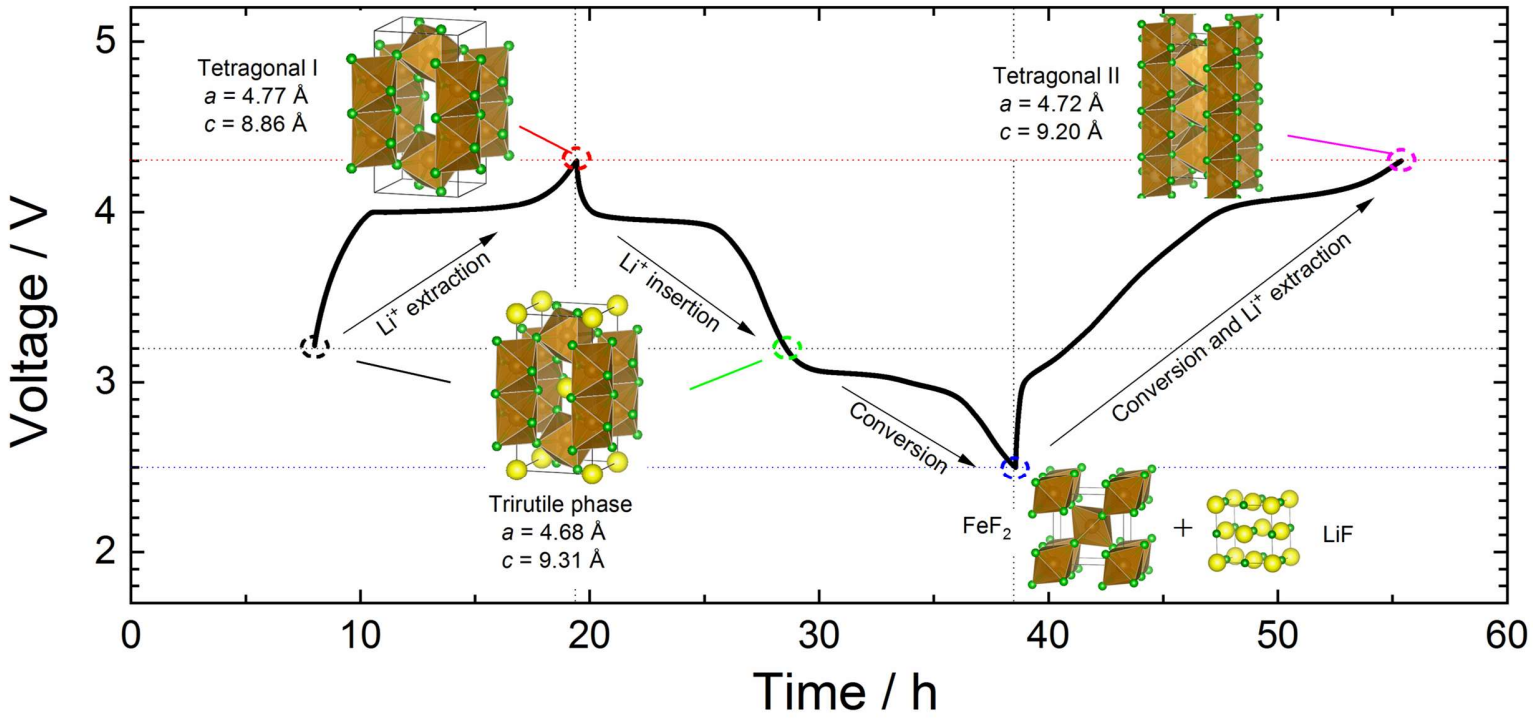

Figure 3-7 Schematic illustration of the reaction pathway for the RBH-$LiFe_2F_6$ electrode during the charge-discharge process. Tetragonal I phase has a delithiated trirutile structure, whereas Tetragonal II phase has a Li-Fe disordered trirutile structure.

References

[1] F. Badway, F. Cosandey, N. Pereira, G.G. Amatucci, J. Electrochem. Soc., 150 (2003) A1318–A1327.

[2] F. Badway, N. Pereira, F. Cosandey, G.G. Amatucci, J. Electrochem. Soc., 150 (2003) A1209–A1218.

[3] R.E. Doe, K.A. Persson, Y.S. Meng, G. Ceder, Chem. Mater., 20 (2008) 5274–5283.

[4] N. Yamakawa, M. Jiang, B. Key, C.P. Grey, J. Am. Chem. Soc., 131 (2009) 10525−10536.

[5] L. Li, R. Jacobs, P. Gao, L. Gan, F. Wang, D. Morgan, S. Jin, J. Am. Chem. Soc., 138 (2016) 2838–2848.

[6] G. Shachar, J. Makovsky, H. Shaked, Phys. Rev. B, 6 (1972) 1968−1974.

[7] J. Fourquet, E. Samedi, Y. Calage, J. Solid State Chem., 77 (1988) 84–89.

[8] H.J. Tan, H.L. Smith, L. Kim, T.K. Harding, S.C. Jones, B. Fultz, J. Electrochem. Soc., 161 (2014) A445−A449.

[9] A. Martin, M.-L. Doublet, E. Kemnitz, N. Pinna, Adv. Funct. Mater., 28 (2018) 1802057.

[10] W. Viebahn, W. Rüdorff, H. Kornelson, Z. Naturforsch. B, 22 (1967) 1218.

[11] V.W. Viebahn, W. Rudorff, R. Hänsler, Chimia, 23 (1969) 503–510.

[12] J. Portier, A. Tressaud, R. Pape, P. Hagenmuller, C. R. Acad. Sci. (Paris), Serie C 267 (1968) 1711−1713.

[13] N. Greenwood, A. Howe, F. Menil, J. Chem. Soc. A, (1971) 2218−2224.

[14] M.M. Wintenberger, M.A. Tressaud, F. Menil, Solid State Commun., 10 (1972) 739−744.

[15] P. Liao, J. Li, J.R. Dahn, J. Electrochem. Soc., 157 (2010) A355–A361.

[16] P. Liao, R.A. Dunlap, J.R. Dahn, J. Electrochem. Soc., 157 (2010) A1080–A1084.

[17] Y. Zheng, R.-F. Li, S.-Q. Wu, Y.-H. Wen, Z.-Z. Zhu, Y. Yang, Electrochemistry, 81 (2013) 12−15.

[18] L.-F. Lin, Q.-R. Xu, Y. Zhang, J.-J. Zhang, Y.-P. Liang, S. Dong, Phys. Rev. Mater., 1 (2017) 1−8.

[19] M. Mori, S. Tanaka, H. Senoh, K. Matsui, T. Okumura, H. Sakaebe, H. Kiuchi, E. Matsubara, Phys. Rev. B, 100 (2019) 1−10.

[20] B.H. Toby, J. Appl. Cryst., 34 (2001) 210−213.

[21] J. Rodríquez-Carvajal, T. Roisnel, Mater. Sci. Forum, 443−444 (2004) 123–126.

[22] K. Momma, F. Izumi, J. Appl. Crystallogr., 44 (2011) 1272−1276.

[23] E.J. Kinast, L.I. Zawislak, J.B.M. da Cunha, V. Antonietti, M.A.Z. de Vasconcellos, C.A. dos Santos, J. Solid State Chem., 163 (2002) 218–223.

[24] M. Nishijima, I.D. Gocheva, S. Okada, T. Doi, J.-i. Yamaki, T. Nishida, J. Power Sources, 190 (2009) 558–562.

[25] N. Yabuuchi, M. Sugano, Y. Yamakawa, I. Nakai, K. Sakamoto, H. Muramatsu, S. Komaba, Journal of Materials Chemistry, 21 (2011) 10035−10041.

[26] S. Tawa, Y. Sato, Y. Orikasa, K. Matsumoto, R. Hagiwara, J. Power Sources, 412 (2019) 180–188.

[27] X. Fan, E. Hu, X. Ji, Y. Zhu, F. Han, S. Hwang, J. Liu, S. Bak, Z. Ma, T. Gao, S.C. Liou, J. Bai, X.Q. Yang, Y. Mo, K. Xu, D. Su, C. Wang, Nat. Commun., 9 (2018) 2324.

[28] Y. Han, H. Li, J. Li, H. Si, W. Zhu, X. Qiu, ACS Appl. Mater. Interfaces, 8 (2016) 32869−32874.

[29] M. Jiang, X. Wang, H. Hu, S. Wei, Y. Fu, Y. Shen, J. Power Sources, 316 (2016) 170−175.

[30] S.W. Kim, D.H. Seo, H. Gwon, J. Kim, K. Kang, Adv. Mater., 22 (2010) 5260–5264.

[31] W. Kang, F. Li, Y. Zhao, C. Qiao, J. Ju, B. Cheng, RSC Advances, 6 (2016) 32646−32652.

[32] M. Kim, S. Lee, B. Kang, Adv Sci (Weinh), 3 (2016) 1500366.

[33] S.-W. Kim, K.-W. Nam, D.-H. Seo, J. Hong, H. Kim, H. Gwon, K. Kang, Nano Today, 7 (2012) 168–173.

[34] J.N. Reimers, J. Electrochem. Soc., 139 (1992) 2091–2097.

[35] R. Koerver, W. Zhang, L. de Biasi, S. Schweidler, A.O. Kondrakov, S. Kolling, T. Brezesinski, P. Hartmann, W.G. Zeier, J. Janek, Energy Environ. Sci., 11 (2018) 2142−2158.

[36] T. Kanamura, H. Naito, T. Yao, Z. Takehara, J. Mater. Chem., 6 (1996) 33−36.

[37] A. Asadi, S.F. Aghamiri, M.R. Talaie, RSC Advances, 6 (2016) 115354−115363.

[38] P. Gibot, M. Casas-Cabanas, L. Laffont, S. Levasseur, P. Carlach, S. Hamelet, J.M. Tarascon, C. Masquelier, Nat. Mater., 7 (2008) 741−747.

[39] C.V. Ramana, A. Mauger, F. Gendron, C.M. Julien, K. Zaghib, J. Power Sources, 187 (2009) 555–564.

[40] U. Srivastava, H. Nigam, Coord. Chem. Rev., 9 (1973) 275−310.

[41] T. Yamamoto, X-Ray Spectrom., 37 (2008) 572−584.

[42] N. Parsai, A. Mishra, Journal of Physics: Conference Series, 836 (2017) 012045.

[43] L. de Biasi, G. Lieser, C. Dräger, S. Indris, J. Rana, G. Schumacher, R. Mönig, H. Ehrenberg, J.R. Binder, H. Geßwein, J. Power Sources, 362 (2017) 192–201.

[44] I. Hwang, S.-K. Jung, E.-S. Jeong, H. Kim, S.-P. Cho, K. Ku, H. Kim, W.-S. Yoon, K. Kang, Nano Res., 10 (2017) 4388–4397.

[45] S. Tawa, K. Matsumoto, R. Hagiwara, J. Electrochem. Soc., 166 (2019) A2105−A2110.

Chapter 4

Li-storage Mechanism of Rutile $Li_{1.2}MnFe_{1.2}F_{6.8}$ *via* Two Redox Reactions

4.1 Introduction

Among electrode materials based on transition metal fluorides in previous works, iron fluoride systems were most widely studied both by experimental and theoretical techniques [1-16]. Mixing of metal ions sometimes withdraws favorable performance of electrode materials from various aspects. In this context, the compound of Li*M*(II)*M*(III)F_6 (*M* = transition metal) has been widely investigated as the positive electrode for lithium-ion batteries (LIBs) [17-23]. Table 4-1 presents a summary of the electrochemical properties of selected Li*M*(II)*M*(III)F_6 positive electrodes for LIBs.

The Li*M*(II)*M*(III)F_6 compounds with trirutile-type (rutile-type when disordered) structure have characteristic structural frames for fluoride materials [24, 25]. Some compounds in the Li*M*(II)*M*(III)F_6 family have also been noted to adopt a rutile structure that is isostructural to the trirutile structure except for the Li^+, *M*(II), and *M*(III) ions which tend to be disordered with random occupancy of metal positions in the rutile structure [17, 18]. For instance, a study by Liao *et al*. reported the cation-disordered rutile-type $LiMgFeF_6$, where all the cations are disordered, but it was found to be electrochemically inactive [17, 18]. In a subsequent study by Lieser *et al*., a cation-ordered trirutile $LiMgFeF_6$ electrode synthesized through a sol-gel process exhibited enhanced

electrochemical properties marked by a reversible specific capacity of 107 mAh g^{-1} [19]. Other studies on the charge-discharge behavior of trirutile $LiNiFeF_6$ have reported Li^+ insertion to occur *via* a phase separation mechanism between Li-lean $Li_{1+x1}NiFeF_6$ and Li-rich $Li_{1+x2}NiFeF_6$ ($x1 \leq 0.16 \leq x2$) where the trirutile structure was preserved [20, 22].

Depending on the arrangement of the different valence metal cations in the octahedral sites, the Na_2SiF_6-type (*P*321) structures have also been reported among certain Li*M*(II)*M*(III)F_6 compositions [21]. Na_2SiF_6-type structure comprises of SiF_6 units sharing three edges with NaF_6 octahedra, forming empty zigzag channels. This channel structure facilitates lithium diffusion in the case of Li*M*(II)*M*(III)F_6. However, the compound $LiMnFeF_6$ with this structure delivers a poor performance because the Li-rich $Li_{1+x}MnFeF_6$ undergoes a phase transition from the Na_2SiF_6-type to rutile-type structure [21]. Reports by Sekino *et al*. have shown that such phase transformations (*i.e.,* Na_2SiF_6-type Li*M*(II)*M*(III)F_6 to rutile-type or trirutile-type structures) can be induced by changes in compositions, pressure, and temperature (e.g. $(Li, Ti)_{1-x}Co_{1+2x}F_6$, $LiNi_{1-x}Mn_xCrF_6$) [21, 26].

Given the detrimental effects of structural transformations from Na_2SiF_6-type to rutile-type in $LiMnFeF_6$ [21], it is postulated that electrochemical performance can be improved by introducing $Li_xMn_yFe_zF_6$ with a rutile-type structure to achieve reversible Li^+ extraction/insertion and circumvent the unfavorable phase transitions. Therefore, in a bid to validate this hypothesis, the preparation of a Li-rich $Li_{1.06}Mn_{0.88}Fe_{1.06}F_6$ phase (hereafter, denoted as $Li_{1.2}MnFe_{1.2}F_{6.8}$) with a cation-disordered rutile structure is

reported as a positive electrode for LIBs for the first time. Here, the electrochemical properties and reaction mechanism(s) of the positive electrode material are explored at elevated temperatures with the aid of a thermally stable IL electrolyte to bring out the electrochemical capabilities of the positive electrode material [27-29]. Additionally, the electrochemical behavior of the composite electrode is explicated in detail using synchrotron XRD and XPS analyses.

4.2 Experimental

In the first step for preparing carbon-coated $Li_{1.2}MnFe_{1.2}F_{6.8}$, LiF, MnF_2, and FeF_3 were mixed in a molar ratio of 1.2 : 1 : 1.2. The mixed powder (~ 1 g) was loaded in an airtight vessel with a zirconia inner wall under a dry argon atmosphere. The mixture was then ball-milled in a planetary ball mill at 800 rpm for 24 h with zirconia balls. The pink powder was recovered from the bowl in the glovebox. In the second step, the collected powder was mixed with AB in a weight ratio of 75:25 through ball-milling for 1 h at 800 rpm.

The electrode sheet was prepared by thoroughly mixing the carbon-coated $Li_{1.2}MnFe_{1.2}F_{6.8}$ with PTFE binder at a ratio of 95:5 using an agate mortar and a pestle. The test electrode was finally obtained by pressing the electrode sheet on fresh Al mesh with a loading mass of ~ 2 mg cm^{-2}. The IL electrolyte was prepared thoroughly stirring the mixture of Li[FSA] and $[C_2C_1im][FSA]$ with a molar ratio of 40:60. Coin cells (2032-type) were assembled in the Ar-filled glovebox with the $Li_{1.2}MnFe_{1.2}F_{6.8}$ working

electrode, the Li[FSA]-[C_2C_1im][FSA] (40:60 in mol) IL electrolyte, and the Li metal disk counter electrode fixed on a stainless steel plate current collector. The glass microfiber separator was immersed in the IL electrolyte under vacuum at 90 °C for 12 h prior to cell assembling. All the electrochemical data were obtained by an HJ-SD8 charge−discharge system. The charge−discharge curves and cycling performance of the working electrode were measured by galvanostatic charge−discharge tests.

The XRD pattern of the final compound carbon-coated $Li_{1.2}MnFe_{1.2}F_{6.8}$ was recorded in the Bragg−Brentano geometry using a Rigaku MiniFlex diffractometer. Structural parameters were refined with the Rietveld refinement by curve-fitting using the GSAS data analysis software [30]. The crystal structure was visualized by the VESTA program [31]. Synchrotron XRD patterns of the $Li_{1.2}MnFe_{1.2}F_{6.8}$ electrodes at different states of charge were recorded in the BL5S2 of the Aichi Synchrotron Radiation Center equipped with a PILATUS 100 K two-dimensional detector with a wavelength of 0.88589 Å. The electrode powders washed with THF and vacuum-dried at room temperature were sealed in Lindeman glass capillaries. The XPS analysis of the $Li_{1.2}MnFe_{1.2}F_{6.8}$ electrodes at different states of charge were carried out using a JEOL JPS-9010 XPS instrument after Ar etching at an ion energy of 400 eV for 30 s. The obtained spectra were analyzed using SpecSurf software.

4.3 Results and discussion

A carbon-coated $Li_{1.2}MnFe_{1.2}F_{6.8}$ composite was prepared *via* a two-step ball-milling process. This composition was selected out of several other compositions in a preliminary screening to avoid the possible formation of byproducts such as Li_3FeF_6. Figure 4-1 shows the XRD pattern of the final composite, which was obtained to ascertain the structure of $Li_{1.2}MnFe_{1.2}F_{6.8}$ crystalline phase in the composite. The obtained XRD data does not detect any residual starting material (LiF, MnF_2, or FeF_3) or the byproduct Li_3FeF_6 phase in the carbon-coated $Li_{1.2}MnFe_{1.2}F_{6.8}$ (Figure 4-1a). Even though the detailed structural analysis is prevented by the broad diffraction peaks, the calculated pattern (red line), which is obtained by Rietveld refinement based on a rutile phase with all the metal cations occupying the 2*a* site (Figure 4-1b and Table 4-2), is congruent with the experimental XRD pattern (black line). The obtained $Li_{1.2}MnFe_{1.2}F_{6.8}$ can be characterized as a rutile structure wherein all cations are disordered in their stoichiometric occupancies in the 2*a* site (Figure 4-1b).

The electrochemical properties of a Li/$Li_{1.2}MnFe_{1.2}F_{6.8}$ half-cell containing Li[FSA]-[C_2C_1im][FSA] (40:60 in mol) IL electrolyte were investigated at room temperature (25 °C) and elevated temperature (90 °C) to determine the effect of temperature on the charge-discharge behavior. The temperature of 90 °C is suitable to improve battery performance using thermally stable ILs without introducing special peripheral materials, whereas most organic electrolytes (and solid-electrolyte interphase from organic electrolytes) are unstable at this temperature [27, 28]. The electrode manifests a limited initial discharge capacity of 63 mAh g^{-1} at 25 °C with poor

electrochemical activity observed across 30 cycles (Figure 4-2a,b). Conversely, the electrode demonstrates improved performance at 90 °C (Figure 4-3), emphasizing the vital role of elevated temperatures and the necessity of a thermally stable IL electrolyte to activate $Li_{1.2}MnFe_{1.2}F_{6.8}$ capabilities [32-35]. As such, the charge-discharge behavior of the $Li_{1.2}MnFe_{1.2}F_{6.8}$ electrode at 90 °C was investigated in the voltage range of 2.5–4.5 V at 23.1 mA g^{-1}, as shown in Figure 4-3a. The initial charge to 4.5 V delivers a capacity of 94 mAh g^{-1}, corresponding to a ~ 0.91 Li^+ extraction (based on its theoretical capacity of 103 mAh g^{-1} equivalence to 1.0 Li^+ extraction from $Li_{1.2}MnFe_{1.2}F_{6.8}$). The initial discharge to 2.5 V results in a 146 mAh g^{-1} capacity, which notably exceeds the abovementioned theoretical capacity of 1.0 Li^+ transfer. This capacity surplus evinces the occurrence of a conversion reaction that most likely ensues below 2.9 V, where a change in the gradient of the discharge curve is noted (Figure 4-3a,b). The rationale behind this behavior will be discussed later with XRD and XPS results. Continued cycling in the 2.5–4.5 V voltage range engenders charge-discharge curves with gentle plateaus around 4.1 V and 3.0 V during charge and discharge, respectively (see dQ/dV plot in Figure 4-3b). The first 10 cycles are marked by a gradual increase in discharge capacity, followed by a steady decrease over the subsequent 30 cycles (see cycling performance in Figure 4-3c,d). Over the 40 cycles, a discharge capacity of 115 mAh g^{-1} is achieved at the 40th cycle. These results suggest that the partial conversion reaction induces different redox activities that increase the discharge capacity of $Li_{1.2}MnFe_{1.2}F_{6.8}$ over the first 10 cycles but cause a gradual electrode degradation that diminishes the discharge capacity thereafter.

In order to examine the effects of a complete conversion reaction on the electrochemical properties of the $Li_{1.2}MnFe_{1.2}F_{6.8}$ electrode, the lower cut-off voltage limit was extended to 2.0 V (Figure 4-4). Charge-discharge curves were obtained in the voltage range of 2.0–4.5 V as illustrated in Figure 4-4a. The initial discharge to 2.0 V is characterized by a long plateau around 2.3 V, attaining a capacity of 417 mAh g^{-1} (Figure 4-4a,b). This discharge capacity corresponds to 4.0 Li^+, wherein 1.0 Li^+ is obtained through insertion and 3.0 Li^+ from the conversion reaction to zero-valent transition metal. The high electrochemical activity of the $Li_{1.2}MnFe_{1.2}F_{6.8}$ electrode between 2.0–4.5 V is considered to be brought out by elevated temperature (90 °C) with the aid of Li[FSA]-$[C_2C_1im][FSA]$ (40:60 in mol) IL electrolyte. During the subsequent cycles, the discharge capacity is observed to progressively decline to 257 mAh g^{-1} at the 10th cycle, accompanied by the disappearance of the long sloping plateau around 2.3 V (Figure 4-4c,d), which evidences that the conversion reaction to zero-valent transition metal is poorly reversible. Compared with some Li*M*(II)*M*(III)F_6-type positive electrode materials listed in Table 4-1, especially Na_2SiF_6-type $LiMnFeF_6$, the rutile $Li_{1.2}MnFe_{1.2}F_{6.8}$ electrode shows a higher discharge capacity in the same voltage range (2.0–4.5 V), even in a narrow voltage range (2.5–4.5 V) and higher rate (23.1 mA g^{-1}). However, long-term cycling of the rutile $Li_{1.2}MnFe_{1.2}F_{6.8}$ electrode is hindered in the two different voltage ranges owing to the limited reversibility of the conversion reaction, which is also observed from the similar family of materials in previous works (see Table 4-1). Nevertheless, the exploration of its reaction mechanism provides important information

to discover the origins of the poor performance and further explore the family of structurally related materials with improved performance.

For deeper insight into the reaction mechanisms of the cation-disordered rutile-type $Li_{1.2}MnFe_{1.2}F_{6.8}$ in the IL electrolyte at 90 °C, synchrotron XRD and XPS measurements were performed on pristine electrodes and electrodes at different states of charge (SOCs), as reflected in Figures 4-5, 4-6, and 4-7. A potential-time profile (Figure 4-5a) highlights the SOCs of the different electrodes subjected to XRD and XPS measurements. Figure 4-5b displays the XRD patterns of the $Li_{1.2}MnFe_{1.2}F_{6.8}$ electrodes at the different SOCs. The pristine electrode with a starting voltage of 3.2 V in a half-cell, which was prepared by mixing the carbon-coated $Li_{1.2}MnFe_{1.2}F_{6.8}$ with PTFE, is depicted by Pattern 1. A diffraction peak appearing around 10.4° is assigned to PTFE. This peak is retained across all patterns obtained. Rietveld fitting performed on other diffraction peaks in the pristine electrode confirms that the structure can be indexed as a cation-disordered rutile phase (S.G. $P4_2/mnm$) with the lattice parameters of a = 4.7969(9) Å and c = 3.2733(6) Å (Figure 4-6a and Table 4-3), which is comparable with those of the carbon-coated $Li_{1.2}MnFe_{1.2}F_{6.8}$ (Figure 4-1a and Table 4-2).

Charging the $Li_{1.2}MnFe_{1.2}F_{6.8}$ electrode to 4.5 V (Pattern 2) causes most diffraction peaks to shift to higher angles. Peaks are assigned to tetoragonal lattice with a larger a and smaller c lattice parameters than that of the original $Li_{1.2}MnFe_{1.2}F_{6.8}$, suggesting a delithiated disordered rutile phase, which was confirmed by the Riedveld refinement (Figure 4-6b and Table 4-3). After discharging to 2.5 V (Pattern 3), the

diffraction pattern of the cation-disordered rutile-type $Li_{1.2}MnFe_{1.2}F_{6.8}$ is observed to be recovered, which establishes that the insertion of Li^+ into the host rutile structure is reversible (Figure 4-6c and Table 4-3). In addition, Pattern 3 also shows new peaks assignable to LiF (S.G.: $Fm\bar{3}m$) and FeF_2 (S.G.: $P4_2/mnm$), denoting the occurrence of a partial conversion reaction from $Li_{1.2}MnFe_{1.2}F_{6.8}$ to LiF and FeF_2 during the discharge from the voltage of 4.5 to 2.5 V: thereby corroborating the interpretation of the charge-discharge results. This observation is consistent with the work on the ordered trirutile $LiFe_2F_6$ discussed at 90 °C in Chapter 3, but it contradicts previous works on the lithium insertion mechanisms which involved the transformation of the trirutile Li*M*(II)*M*(III)F_6 phase to Li-rich phase $Li_{1+x}M$(II)*M*(III)F_6 operating at different temperatures of 25 °C. [19, 20, 22]. Extended discharge to 2.0 V (Pattern 4) triggers a further conversion reaction to Fe (space group: $Im\ \bar{3}\ m$) while preserving the cation-disordered rutile-type $Li_{1.2}MnFe_{1.2}F_{6.8}$, as is confirmed by the Rietveld refinement (Figure 4-6d and Table 4-3). This conversion reaction is observed in the discharge process of iron fluorides (FeF_3 and FeF_2), even though the starting material is different from this work [36, 37]. In addition, after recharging to 4.5 V from 2.5 V (Pattern 5), the peaks of the delithiated rutile phase are observed alongside LiF and FeF_2 peaks. This reveals that the partial conversion from the mixture of LiF and FeF_2 to the cation-disordered rutile-type $Li_{1.2}MnFe_{1.2}F_{6.8}$ occurred along with the subsequent extraction of Li^+. The lattice parameters of the delithiated phase in Pattern 5 (Figure 4-6e and Table 4-3) bear a close resemblance to those of the delithiated phase in Pattern 2 (Figure 4-6b and Table 4-3), which provides an attestation

that Li^+ extraction/insertion from/into the disordered rutile-type $Li_{1.2}MnFe_{1.2}F_{6.8}$ phase/delithiated rutile-type phase is reversible.

Even though the pertinent electrochemical reactions are discerned using synchrotron XRD measurements, the oxidation states of Mn could not be ascertained due to the broad and weak diffraction peaks. Therefore, XPS measurements were performed in the Mn 3p region to track the Mn oxidation states. Figure 4-7 shows the Mn 3p spectra at different SOCs (the spectrum number corresponds to the XRD pattern numbers). The pristine electrode (Spectrum 1) displays a peak assignable to Mn(II) at the binding energy of 49.3 eV [38, 39]. Charging to 4.5 V (Spectrum 2) produces a peak at 49.9 eV. This peak is assigned to Mn(III) [40, 41], indicating the extraction of Li^+ from the disordered rutile-type $Li_{1.2}MnFe_{1.2}F_{6.8}$. The binding energy is seen to return to 49.3 eV upon discharge to 2.5 V (Spectrum 3), suggesting that Mn(III) is reduced to Mn(II). When the electrode was further discharged to 2.0 V (Spectrum 4), the Mn(II) peak disappears and is replaced by a Mn(0) peak at 47.8 eV [42]. This confirms the occurrence of the further conversion reaction to LiF and metallic Mn formed by the reduction of Mn(II). Spectrum 5, obtained after the second charge from 2.5 V to 4.5 V, displays a broad peak that can be fitted with two peaks corresponding to Mn(II) and Mn(III) at 49.3 eV and 49.9 eV, respectively. This observation not only demonstrates the partial oxidation of Mn(II) but also corroborates the conclusion from the XRD results, evincing that the second charge starts to involve two redox couples: Fe(II)/Fe(III) and Mn(II)/Mn(III) which are obtained from the

conversion reaction that transforms the mixture of LiF, FeF_2/MnF_2 to the cation-disordered rutile-type $Li_{1.2}MnFe_{1.2}F_{6.8}$.

Figure 4-8 shows the schematic illustration of reaction mechanism for a $Li/Li_{1.2}MnFe_{1.2}F_{6.8}$ half-cell with the Li[FSA]-[C_2C_1im][FSA] (40:60 in mol) IL electrolyte at 90 °C. In a certain high voltage range between around 3.2 V to 4.5 V, a reversible topotactic insertion reaction is observed. This extraction/insertion reaction is proved by XPS measurement that it is accompanied by the Mn(II)/Mn(III) redox reaction in the first cycle. In a low voltage range between around 3.2 V to 2.5 V, conversion reactions from the cation-disordered rutile $Li_{1.2}MnFe_{1.2}F_{6.8}$ to rutile FeF_2, rutile MnF_2, and LiF occur along with the redox reaction of Fe(III)/Fe(II), which is marked by a change in the gradient of the discharge curve (Figure 4-3a,b). Further conversion reactions to metallic Fe, Mn and LiF occur in the low voltage ranges of 2.5–2.0 V with a characterization of a long plateau around 2.3 V (Figure 4-4a,b), involving two redox reactions of Fe(II)/Fe(0), and Mn(II)/Mn(0).

4.4 Conclusions

This chapter described a carbon-coated $Li_{1.2}MnFe_{1.2}F_{6.8}$ with cation-disordered rutile-type structure for the first time, obtained by two-step ball-milling of its stoichiometric precursors. Through a combination of charge-discharge tests in the voltage range of 2.5–4.5 V at 90 °C, synchrotron XRD and XPS analyses, it is established that the reversible topotactic extraction/insertion of Li^+ from/into $Li_{1.2}MnFe_{1.2}F_{6.8}$ cumulatively results from

a synergy of redox reactions involving Mn(II)/Mn(III) and a partial conversion reaction that transforms the cation-disordered rutile $Li_{1.2}MnFe_{1.2}F_{6.8}$ to LiF and rutile FeF_2. Additionally, a deep discharge to 2.0 V triggers a further conversion reaction to Fe(0)/Mn(0) and LiF. Here, new electrochemical properties of a Li-Mn-Fe-F material are unveilled at elevated temperature with the aid of an IL electrolyte. This work not only provides evidence of two redox couples in the electrode material but also adequately demonstrates the utilization of multiple redox couples to achieve more than 1.0 Li^+ exchange in lithium transition metal fluorides.

Table 4-1 Electrochemical properties of selected Li*M*(II)*M*(III)F_6-type positive electrode materials for LIBs.

Electrodes	Synthetic methods	Electrolyte@Temperature	1st discharge capacity (voltage range@rate)	Cycling performance (cycle number)	Reaction mechanism
Disordered rutile-type $LiFe_2F_6$ [17]	Ball-milling	1 M Li[PF_6]-EC:DEC@25 °C	102 mAh g^{-1} (2.5–4.0 V@9.3 mA g^{-1}) 126 mAh g^{-1} (2.0–4.5 V@9.3 mA g^{-1})	81% (17 cycles) 62% (14 cycles)	Reversible lithium insertion in trirutile $Li_{1+x}Fe_2F_6$
Disordered rutile-type $LiMgFeF_6$ [17]	Ball-milling	1 M Li[PF_6]-EC:DEC@25 °C	Electrochemically inactive	Electrochemically inactive	Electrochemically inactive
Disordered rutile-type $Li_{1.2}Fe_2F_{6.2}$ [17, 18]	Ball-milling	1 M Li[PF_6]-EC:DEC@25 °C	109 mAh g^{-1} (2.5–4.0 V@9.3 mA g^{-1}) 155 mAh g^{-1} (2.0–4.5 V@9.3 mA g^{-1})	84% (16 cycles) 88% (27 cycles)	Reversible lithium insetion
Trirutile $LiMgFeF_6$ [19]	Sol-gel synthesis	1 M Li[PF_6]-EC:DMC@25 °C	89 mAh g^{-1} (2–4.5 V@6.66 mA g^{-1})	120.2% (20 cycles)	Reversible lithium insertion
Trirutile $LiNiFeF_6$ [20, 22]	Sol-gel synthesis	1 M Li[PF_6]-EC:DMC@25 °C	95 mAh g^{-1} (2–4.5 V@5.7 mA g^{-1})	92.6% (20 cycles)	Reversible lithium insertion between trirutile Li-poor $Li_{1+x1}NiFeF_6$ and trirutile Li-rich $Li_{1+x2}NiFeF_6$
Colquiriite-type $LiCaFeF_6$ [23]	Solid-state method	1 M Li[PF_6]-EC:DMC@25 °C	112 mAh g^{-1} (2–4.5 V@6.18 mA g^{-1})	83.9% (20 cycles)	Reversible lithium insertion
Na_2SiF_6-type $LiMnFeF_6$ [21]	Sol-gel synthesis	1 M Li[PF_6]-EC:DMC@25 °C	95 mAh g^{-1} (2.2–4.3 V@5.78 mA g^{-1})	76.8% (10 cycles)	Reversible lithium insertion between Na_2SiF_6-type $LiMnFeF_6$ and rutile-type $Li_{1+x}MnFeF_6$

Table 4-2 Crystallographic parameters of the carbon-coated $Li_{1.2}MnFe_{1.2}F_{6.8}$ with cation-disordered rutile structure obtained by Rietveld refinement.

Refinement results for the carbon-coated $Li_{1.2}MnFe_{1.2}F_{6.8}$ with cation-disordered rutile structure (S.G. $P4_2/mnm$)
R_p = 1.63%, R_{wp} = 2.12%

a = 4.789(1) Å		c = 3.2756(9) Å			V = 75.14(5) Å^3	
Atom	Wyckoff symbol	x	y	z	Biso / Å^2	Occup.
Li	2a	0	0	0	0.5	0.3529
Fe	2a	0	0	0	0.5	0.3529
Mn	2a	0	0	0	0.5	0.2942
F	4f	0.2981(7)	0.2981(7)	0	0.5	1

Table 4-3 Crystallographic parameters of the $Li_{1.2}MnFe_{1.2}F_{6.8}$ phase in Patterns 1, 2, 3, 4, and 5 in Figure 4-6 (Figure 4-5b).

Refinement results for $Li_{1.2}MnFe_{1.2}F_{6.8}$ in Pattern 1[a] (S.G. $P4_2/mnm$) R_p = 3.34%, R_{wp} = 4.46%

a = 4.7969(9) Å		c = 3.2733(6) Å			V = 75.32(4) Å^3	
Atom	Wyckoff symbol	x	y	z	Biso / Å^2	Occup.
Li	2a	0	0	0	0.5	0.3529
Fe	2a	0	0	0	0.5	0.3529
Mn	2a	0	0	0	0.5	0.2941
F	4f	0.3104(4)	0.3104(4)	0	0.5	1

Refinement results for $MnFe_{1.2}F_{6.8}$ in Pattern 2[b] (S.G. $P4_2/mnm$) R_p = 4.62%, R_{wp} = 5.99%

a = 4.839(2) Å		c = 3.070(2) Å			V = 71.89(8) Å^3	
Atom	Wyckoff symbol	x	y	z	Biso / Å^2	Occup.
Fe	2a	0	0	0	0.5	0.3529
Mn	2a	0	0	0	0.5	0.2941
F	4f	0.295(1)	0.295(1)	0	0.5	1

Refinement results for $Li_{1.2}MnFe_{1.2}F_{6.8}$ in Pattern 3[c] (S.G. $P4_2/mnm$) R_p = 2.21%, R_{wp} = 2.88%

a = 4.7997(7) Å		c = 3.2618(6) Å			V = 75.14(3) Å^3	
Atom	Wyckoff symbol	x	y	z	Biso / Å^2	Occup.
Li	2a	0	0	0	0.5	0.3529
Fe	2a	0	0	0	0.5	0.3529
Mn	2a	0	0	0	0.5	0.2941
F	4f	0.2969(7)	0.2969(7)	0	0.5	1

Refinement results for $Li_{1.2}MnFe_{1.2}F_{6.8}$ in Pattern 4[d] (S.G. $P4_2/mnm$) R_p = 2.02%, R_{wp} = 2.79%

a = 4.7894(5) Å		c = 3.2649(5) Å			V = 74.89(2) Å^3	
Atom	Wyckoff symbol	x	y	z	Biso / Å^2	Occup.
Li	2a	0	0	0	0.5	0.3529
Fe	2a	0	0	0	0.5	0.3529
Mn	2a	0	0	0	0.5	0.2941
F	4f	0.2944(5)	0.2944(5)	0	0.5	1

Refinement results for $MnFe_{1.2}F_{6.8}$ in Pattern 5[e] (S.G. $P4_2/mnm$) R_p = 3.52%, R_{wp} = 4.70%

a = 4.816(3) Å		c = 3.097(2) Å			V = 71.84(8) Å^3	
Atom	Wyckoff symbol	x	y	z	Biso / Å^2	Occup.
Fe	2a	0	0	0	0.5	0.3529
Mn	2a	0	0	0	0.5	0.2941
F	4f	0.2962(9)	0.2962(9)	0	0.5	1

[a]There is no minor phase. [b]The cation-disordered rutile $Li_{1.2}MnFe_{1.2}F_{6.8}$ ($P4_2/mnm$) is considered to be minor phase. [c]The rutile FeF_2 ($P4_2/mnm$), rutile MnF_2 ($P4_2/mnm$) and LiF ($Fm\bar{3}m$) are considered to be minor phases. [d]The rutile FeF_2 ($P4_2/mnm$), rutile MnF_2 ($P4_2/mnm$), LiF ($Fm\bar{3}m$) and Fe ($Im\bar{3}m$) are considered to be minor phases. [e]The disordered trirutile $Li_{1.2}MnFe_{1.2}F_{6.8}$ ($P4_2/mnm$), rutile FeF_2 ($P4_2/mnm$), rutile MnF_2 ($P4_2/mnm$) and LiF ($Fm\bar{3}m$) are considered to be minor phases.

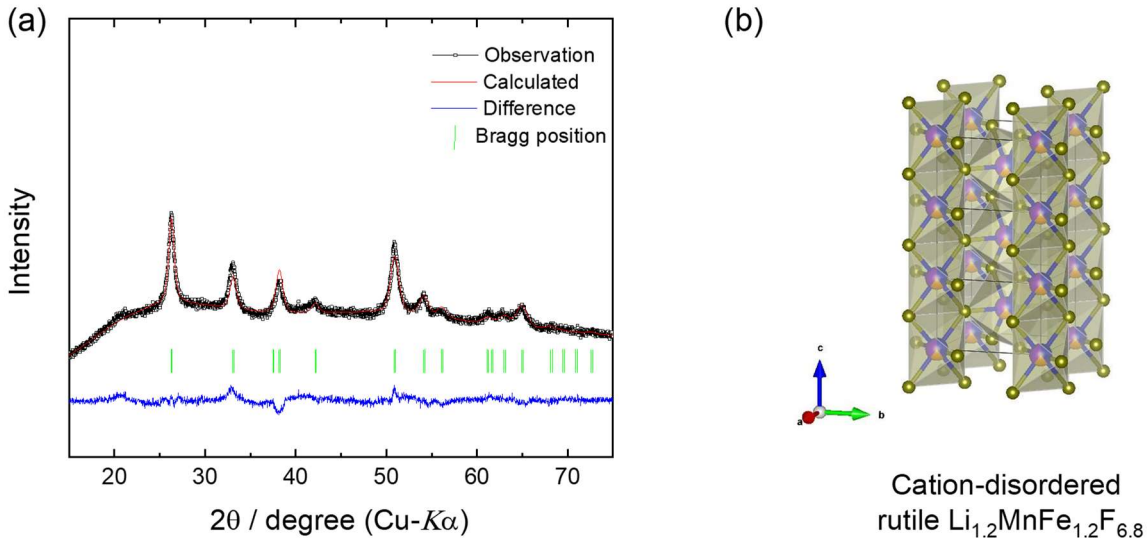

Figure 4-1 (a) XRD pattern of the carbon-coated $Li_{1.2}MnFe_{1.2}F_{6.8}$ powder. (b) The refined crystal structure of the cation-disordered rutile $Li_{1.2}MnFe_{1.2}F_{6.8}$. Li, Mn, Fe, and F atoms are represented by purple, orange, blue, and green spheres, respectively. The ratio of Li, Mn, and Fe is depicted by their corresponding colors on the metal site sphere of the rutile structure.

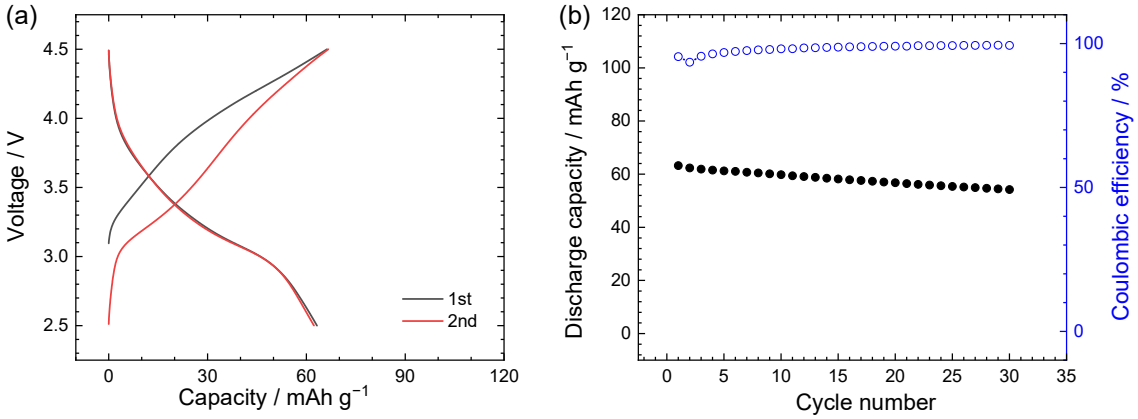

Figure 4-2 Electrochemical properties of the Li/$Li_{1.2}MnFe_{1.2}F_{6.8}$ half-cell containing Li[FSA]-[C_2C_1im][FSA] (40:60 in mol) IL electrolyte at 25 °C. (a) The 1st and 2nd charge-discharge curves, and (b) cycling performance. Rate: 23.1 mA g^{-1}. Cutoff voltage: 2.5–4.5 V.

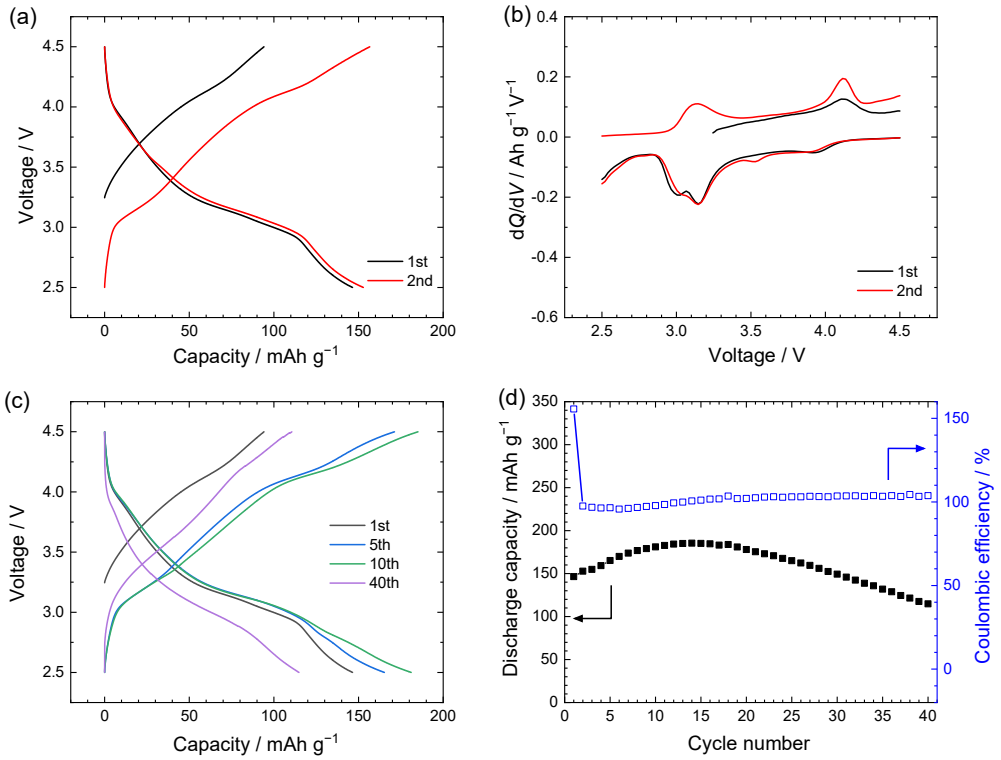

Figure 4-3 Electrochemical properties of the Li/$Li_{1.2}MnFe_{1.2}F_{6.8}$ cell at 90 °C (rate: 23.1 mA g^{-1}). (a) The 1st and 2nd charge-discharge curves in the voltage range of 2.5–4.5 V and (b) their corresponding dQ/dV plots. (c) The corresponding charge-discharge curves at the 1st, 5th, 10th, and 40th cycles and (d) cycling performance during 40 cycles.

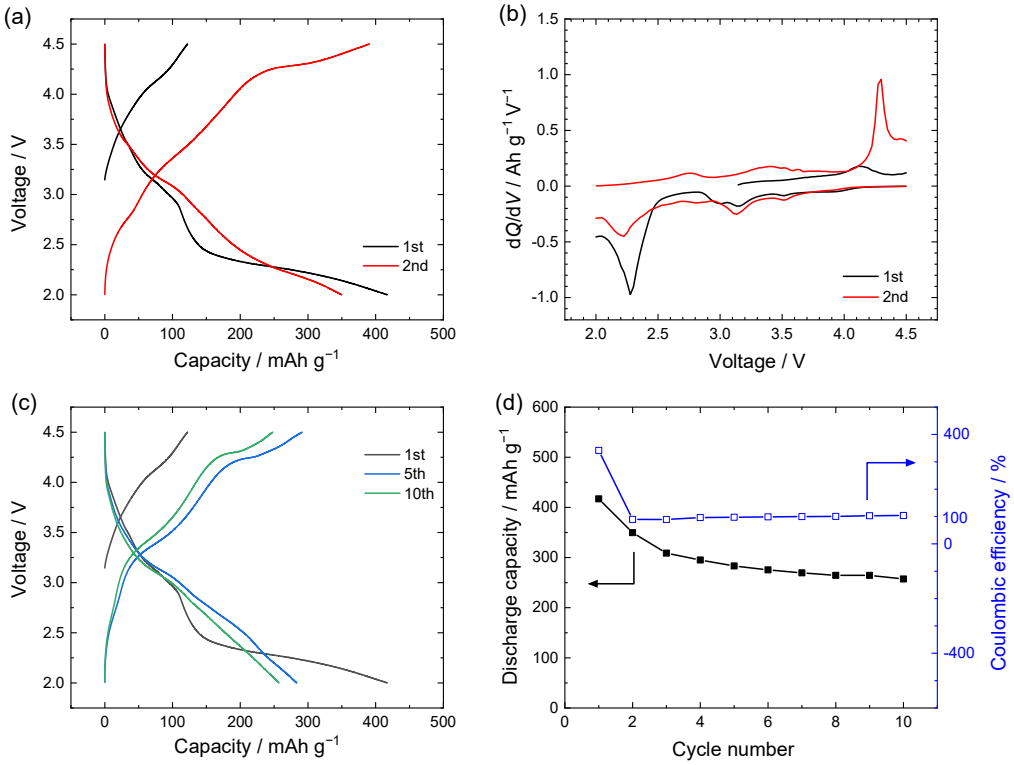

Figure 4-4 Electrochemical properties of the Li/$Li_{1.2}MnFe_{1.2}F_{6.8}$ cell at 90 °C (rate: 23.1 mA g^{-1}). (a) The 1st and 2nd charge-discharge curves in the voltage range of 2.0–4.5 V and (b) their corresponding dQ/dV plots. (c) The corresponding charge-discharge curves at the 1st, 5th, and 10th cycles and (d) cycling performance for 10 cycles.

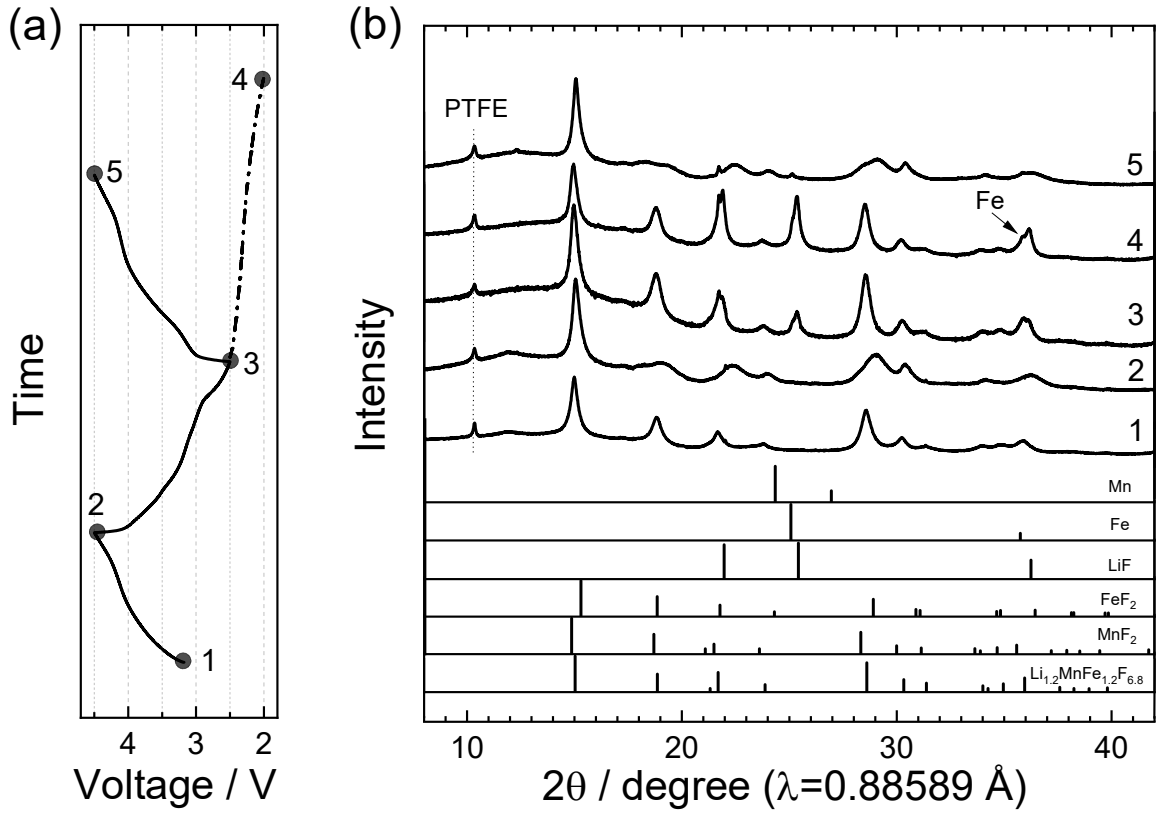

Figure 4-5 (a) Charge-discharge voltage profiles of $Li_{1.2}MnFe_{1.2}F_{6.8}$ electrodes at different SOCs. The electrodes were measured (1) in the pristine state, (2) after the initial charge to 4.5 V, (3) after the initial discharge to 2.5 V, (4) after a deep discharge to 2.0 V, and (5) after the second charge to 4.5 V from the 2.5 V discharged state. (b) Ex-situ synchrotron XRD data of $Li_{1.2}MnFe_{1.2}F_{6.8}$ at different SOCs.

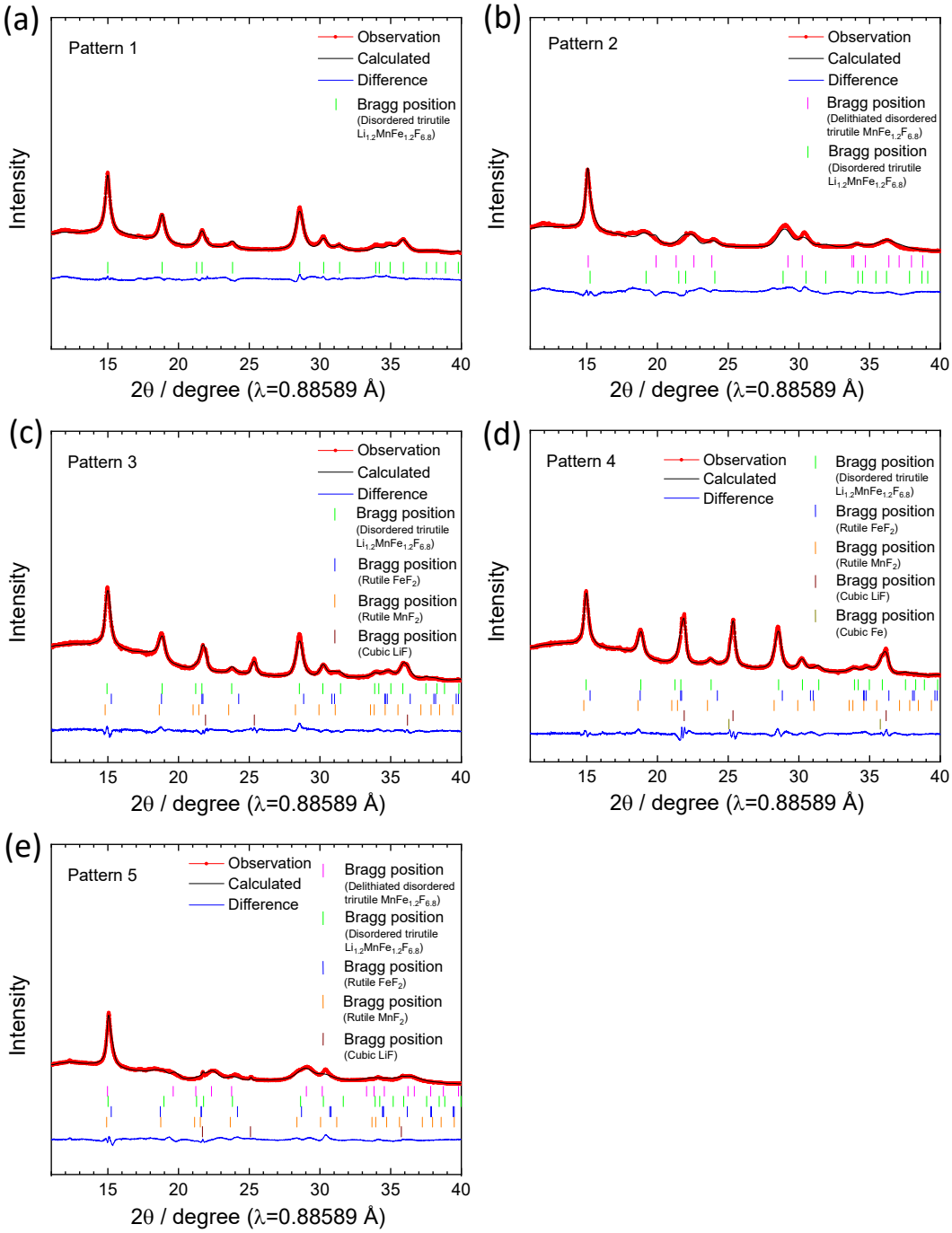

Figure 4-6 Rietveld refinement results of the XRD patterns at different states of charge for the $Li_{1.2}MnFe_{1.2}F_{6.8}$ electrode. (a) Pattern 1, (b) Pattern 2, (c) Pattern 3, (d) Pattern 4, and (e) Pattern 5 corresponding to the states in Figure 4-5a (refined crystallographic parameters are listed in Table 4-3).

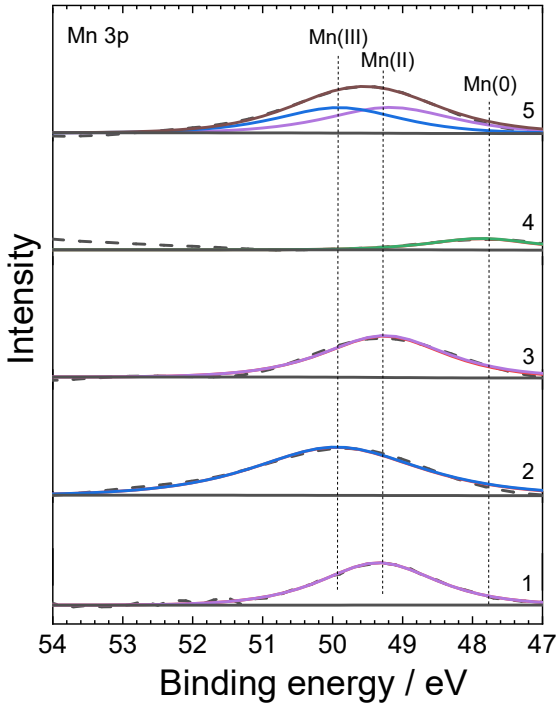

Figure 4-7 The XPS spectra in the Mn 3p region of the $Li_{1.2}MnFe_{1.2}F_{6.8}$ electrodes at different SOCs corresponding to the states in Figure 4-5a.

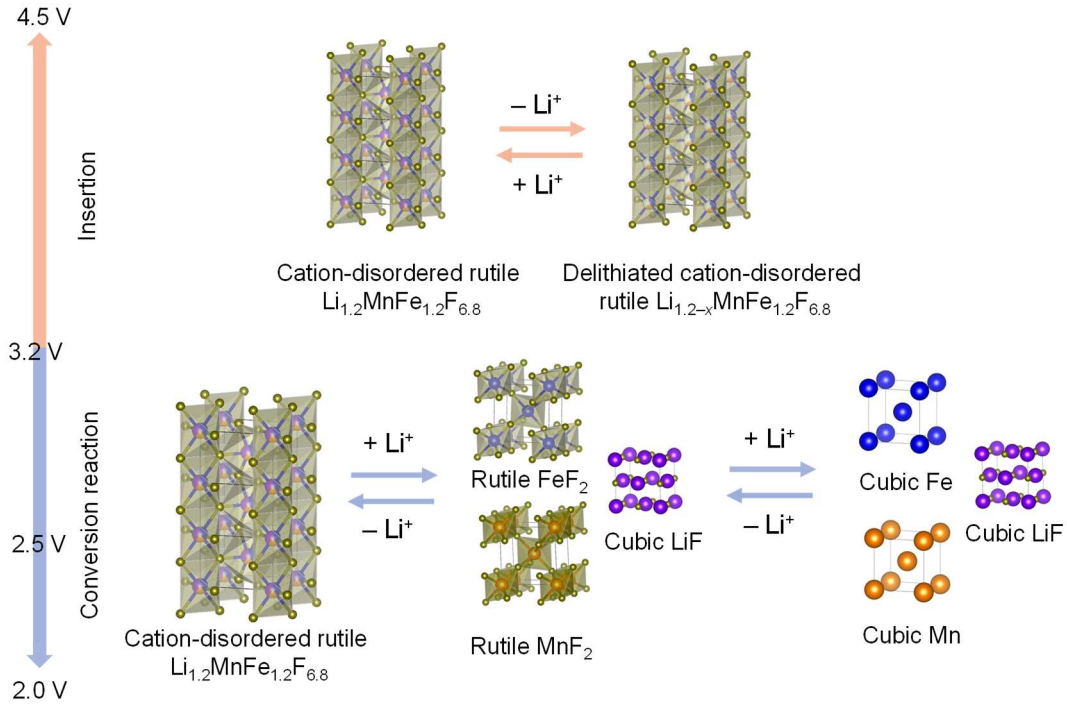

Figure 4-8 The schematic illustration of reaction mechanism for a Li/$Li_{1.2}MnFe_{1.2}F_{6.8}$ half-cell with the Li[FSA]-[C_2C_1im][FSA] (40:60 in mol) IL electrolyte at 90 °C.

References

[1] H. Li, G. Richter, J. Maier, Adv. Mater., 15 (2003) 736−739.

[2] F. Badway, F. Cosandey, N. Pereira, G.G. Amatucci, J. Electrochem. Soc., 150 (2003) A1318–A1327.

[3] F. Badway, N. Pereira, F. Cosandey, G.G. Amatucci, J. Electrochem. Soc., 150 (2003) A1209–A1218.

[4] H. Li, P. Balaya, J. Maier, J. Electrochem. Soc., 151 (2004) A1878−A1885.

[5] R.E. Doe, K.A. Persson, Y.S. Meng, G. Ceder, Chem. Mater., 20 (2008) 5274–5283.

[6] N. Yamakawa, M. Jiang, B. Key, C.P. Grey, J. Am. Chem. Soc., 131 (2009) 10525−10536.

[7] R.F. Li, S.Q. Wu, Y. Yang, Z.Z. Zhu, J. Phys. Chem. C, 114 (2010) 16813−16817.

[8] M. Zhou, L. Zhao, A. Kitajou, S. Okada, J.-i. Yamaki, J. Power Sources, 203 (2012) 103−108.

[9] L. Li, F. Meng, S. Jin, Nano Lett., 12 (2012) 6030−6037.

[10] P. Liu, J.J. Vajo, J.S. Wang, W. Li, J. Liu, J. Phys. Chem. C, 116 (2012) 6467−6473.

[11] D.E. Conte, N. Pinna, Mater. Renew. Sustain. Energy, 3 (2014) 1−22.

[12] H.J. Tan, H.L. Smith, L. Kim, T.K. Harding, S.C. Jones, B. Fultz, J. Electrochem. Soc., 161 (2014) A445−A449.

[13] S.K. Martha, J. Nanda, H. Zhou, J.C. Idrobo, N.J. Dudney, S. Pannala, S. Dai, J. Wang, P.V. Braun, RSC Adv., 4 (2014) 6730–6737.

[14] A. Kitajou, I. Tanaka, Y. Tanaka, E. Kobayashi, H. Setoyama, T. Okajima, S. Okada, Electrochemistry, 85 (2017) 472–477.

[15] C. Li, K. Chen, X. Zhou, J. Maier, npj Comput. Mater., 4 (2018).

[16] N. Zhang, X. Xiao, H. Pang, Nanoscale Horiz., 4 (2019) 99−116.

[17] P. Liao, J. Li, J.R. Dahn, J. Electrochem. Soc., 157 (2010) A355–A361.

[18] P. Liao, R.A. Dunlap, J.R. Dahn, J. Electrochem. Soc., 157 (2010) A1080–A1084.

[19] G. Lieser, C. Dräger, L. de Biasi, S. Indris, H. Geßwein, S. Glatthaar, M.J. Hoffmann, H. Ehrenberg, J.R. Binder, J. Power Sources, 274 (2015) 1200−1207.

[20] G. Lieser, C. Dräger, M. Schroeder, S. Indris, L. de Biasi, H. Geßwein, S. Glatthaar, H. Ehrenberg, J.R. Binder, J. Electrochem. Soc., 161 (2014) A1071–A1077.

[21] G. Lieser, L.d. Biasi, H. Geßwein, S. Indris, C. Dräger, M. Schroeder, S. Glatthaar, H. Ehrenberg, J.R. Binder, J. Electrochem. Soc., 161 (2014) A1869–A1876.

[22] L. de Biasi, G. Lieser, J. Rana, S. Indris, C. Dräger, S. Glatthaar, R. Mönig, H. Ehrenberg, G. Schumacher, J.R. Binder, H. Geßwein, CrystEngComm, 17 (2015) 6163−6174.

[23] L. de Biasi, G. Lieser, C. Dräger, S. Indris, J. Rana, G. Schumacher, R. Mönig, H. Ehrenberg, J.R. Binder, H. Geßwein, J. Power Sources, 362 (2017) 192–201.

[24] W. Viebahn, W. Rüdorff, H. Kornelson, Z. Naturforsch. B, 22 (1967) 1218.

[25] V.W. Viebahn, W. Rudorff, R. Hänsler, Chimia, 23 (1969) 503–510.

[26] T. Sekino, T. Endo, T. Sato, M. Shimada, J. Solid State Chem., 88 (1990) 505−512.

[27] X. Lin, M. Salari, L.M. Arava, P.M. Ajayan, M.W. Grinstaff, Chem. Soc. Rev., 45 (2016) 5848−5887.

[28] M.-T.F. Rodrigues, G. Babu, H. Gullapalli, K. Kalaga, F.N. Sayed, K. Kato, J. Joyner, P.M. Ajayan, Nat. Energy, 2 (2017) 1−14.

[29] J. Hwang, K. Matsumoto, R. Hagiwara, Adv. Sustainable Syst., 2 (2018) 1700171.

[30] B.H. Toby, J. Appl. Cryst., 34 (2001) 210−213.

[31] K. Momma, F. Izumi, J. Appl. Crystallogr., 44 (2011) 1272−1276.

[32] T. Torimoto, T. Tsuda, K. Okazaki, S. Kuwabata, Adv. Mater., 22 (2010) 1196−1221.

[33] D.R. MacFarlane, N. Tachikawa, M. Forsyth, J.M. Pringle, P.C. Howlett, G.D. Elliott, J.H. Davis, M. Watanabe, P. Simon, C.A. Angell, Energy Environ. Sci., 7 (2014) 232−250.

[34] K. Matsumoto, E. Nishiwaki, T. Hosokawa, S. Tawa, T. Nohira, R. Hagiwara, J. Phys. Chem. C, 121 (2017) 9209–9219.

[35] J. Hwang, H. Okada, R. Haraguchi, S. Tawa, K. Matsumoto, R. Hagiwara, J. Power Sources, 453 (2020) 1−6.

[36] L. Li, R. Jacobs, P. Gao, L. Gan, F. Wang, D. Morgan, S. Jin, J. Am. Chem. Soc., 138 (2016) 2838–2848.

[37] A.W. Xiao, H.J. Lee, I. Capone, A. Robertson, T.U. Wi, J. Fawdon, S. Wheeler, H.W. Lee, N. Grobert, M. Pasta, Nature Mater., 19 (2020) 644–654.

[38] A. Aoki, J. Appl. Phys., 15 (1976) 305−311.

[39] X. Xiao, Z. Liu, L. Baggetto, G.M. Veith, K.L. More, R.R. Unocic, Phys. Chem. Chem. Phys., 16 (2014) 10398−10402.

[40] G. Fortunato, H.R. Oswald, A. Reller, J. Mater. Chem., 11 (2001) 905−911.

[41] K.M. Shaju, K.V. Ramanujachary, S.E. Lofland, G.V. Subba Rao, B.V.R. Chowdari, J. Mater. Chem., 13 (2003) 2633−2640.

[42] A.R. Chourasia, D.R. Chopra, Surf. Sci. Spectra, 3 (1994) 74−81.

Chapter 5

Structural Evolution of Trirutile-derived FeF_3 during Continuous Sodiation and Desodiation

5.1 Introduction

In the search for reliable battery systems, SIBs have also gained traction due to their high performance and the abundance of Na resources [1-3]. At present, the reaction mechanisms of FeF_3 in LIBs have been extensively studied through both experimental and theoretical techniques [4-10], but that in SIBs remain vastly underexplored [11-19].

Table 5-1 lists noteworthy works on FeF_3 and $NaFeF_3$ positive electrodes in SIBs. Experimental reports on FeF_3 electrodes have demonstrated that the reduction of Fe^{3+} to Fe^{2+} involves a classical process of Na^+ insertion occurring on FeF_3 to be $NaFeF_3$. However, no experimental evidence on the phase structures or the existence of a Na_xFeF_3 intermediate phase has been reported to date [17, 20]. Nonetheless, other studies on $NaFeF_3$ have provided insight into the phase evolutions during the desodiation-sodiation processes. For instance, density functional theory calculations on the orthorhombic $NaFeF_3$ (*Pnma*) predicted that the oxidation of Fe^{2+} to Fe^{3+} was engendered by Na^+ extraction from the orthorhombic $NaFeF_3$ to form fully desodiated FeF_3 (*Pnma*): a slightly more stable phase than the trigonal ($R\bar{3}c$) and cubic ($Pm\bar{3}m$) phases [21]. The theoretical works further indicated an energetically stable, intermediate phase of orthorhombic

$Na_{0.5}FeF_3$, as a line compound in the extraction process [21, 22]. A recent experimental work on nano-sized materials reported a phase transformation from orthorhombic $NaFeF_3$ (*Pnma*) to cubic FeF_3 ($Pm\bar{3}m$), albeit without forming trirutile $Na_{0.5}FeF_3$ [23, 24]. Although the phase transformation was not observed, this study was the first to mention trirutile $Na_{0.5}FeF_3$ in the context of the Na-Fe-F system.

A trirutile-derived FeF_3 (hereafter, tetragonal-1 FeF_3) is formed by the delithiation of the trirutile $LiFe_2F_6$ (space group: $P4_2/mnm$) as described in Chapter 3, which undergoes reversible Li^+ insertion/extraction through two-phase reaction with the trirutile $LiFe_2F_6$. Given that the tetragonal-1 FeF_3 phase has not been exploited as a positive electrode in SIBs, the findings from the Li system emphasize the importance of understanding tetragonal-1 FeF_3 phase evolutions as the means to decipher the iron fluoride mechanisms in the Na-Fe-F system for future material designs. More importantly, the reports predict the possibility of observing the reversible Na^+ extraction/insertion from/into the trirutile-type structure with the tetragonal-1 FeF_3 phase as the starting material which cannot be experimentally synthesized so far. Therefore, in an attempt to explicate the phase evolutions occurring in the Na-Fe-F system, the electrochemical properties and the reaction mechanisms of the tetragonal-1 FeF_3 were investigated in the Na system by means of charge-discharge measurements, GITT, and synchrotron XRD.

5.2 Experimental

Trirutile $LiFe_2F_6$ was prepared by the ball-milling method according to the procedure described in Chapter 3. Tetragonal-1 FeF_3 was prepared by the electrochemical delithiation of the trirutile $LiFe_2F_6$ electrode (Figure 5-1). The electrode was fabricated by pressing a mixture of 95 wt% ball-milled composite $LiFe_2F_6$/AB (75:25 wt%) and 5 wt% PTFE onto an Al mesh. The electrochemical delithiation of trirutile $LiFe_2F_6$ to tetragonal-1 FeF_3 was carried out at a current density of 10 mA g^{-1} in a 2032-type half-cell with a Li metal counter electrode fixed on stainless steel plate current collector. The Li[FSA]-[C_2C_1im][FSA] IL in a molar ratio of 30:70 was used as the electrolyte. After electrochemical delithiation, the cell was disassembled in the glove box. The obtained FeF_3 electrode was then washed with THF and dried under vacuum at room temperature for 12 h. Sodiation-desodiation properties were analyzed in a 2032-type half-cell using the tetragonal-1 FeF_3 positive electrode, a Na metal fixed on Al plate current collector as the counter electrode, and the Na[FSA]-[C_2C_1im][FSA] IL in a molar ratio of 30:70 as the electrolyte. The glass microfiber separator was immersed in the IL electrolyte under vacuum at 90 °C for 12 h prior to the cell assembling. For all the cells, the applied current and the resulting capacity were calculated based on the weight of the pristine $LiFe_2F_6$ electrode (2.00 mg cm^{-2}) according to the following equation:

$$\text{Capacity (mAh g}^{-1}\text{)} = \text{Current (mA) x Time (h) / Mass of the active material (g)}$$

All the electrochemical measurements were performed at an elevated temperature of 90 °C with the aid of thermally stable IL electrolyte. The Na cell was galvanostatically cycled at 21.4 mA g^{-1} in two voltage ranges of 2.6–4.0 and 2.3–4.0 V. The cell for GITT was charged or discharged at 10 mA g^{-1} for 1 h followed by 5-hour open circuit relaxation between 2.3−4.0 V. CV was performed using a VSP potentiostat at a scan rate of 0.1 mV s^{-1} at 90 °C, in which the half-cell was firstly scanned from open circuit voltage to lower voltage in both two voltage ranges.

The Li and Fe contents in the tetragonal-1 FeF_3 were determined after dissolution with sulfuric, nitric, and perchloric acids by AAS and ICP−AES, respectively. The crystalline phases of the charged and discharged electrodes were analyzed by XRD at the BL5S2 beam line of Aichi Synchrotron Radiation Center (wavelength of 0.88589 Å) equipped with a PILATUS 100K two-dimensional detector. The charged and discharged electrode samples were washed with THF, vacuum-dried at room temperature, and then sealed in Lindeman glass capillaries for synchrotron XRD measurements. Structural parameters were refined with the Rietveld refinement by curve-fitting using the GSAS data analysis software [25]. The crystal structure was visualized by the VESTA program [26].

5.3 Results and discussion

The tetragonal-1 FeF_3 phase was electrochemically prepared by delithiating trirutile $LiFe_2F_6$ with the aid of a thermally stable IL electrolyte, Li[FSA]-[C_2C_1im][FSA] (30:70 in mol), at a current density of 10 mA g^{-1} (Figure 5-1) [27]. The process was conducted at 90 °C in light of previous study that revealed that high temperature was essential in activating the delithiation reaction (see Chapter 3). As displayed in Figure 5-1, the delithiation occurred *via* a two-phase process marked by a plateau at 4.0 V. Synchrotron XRD analysis performed at the end of the delithiation confirmed the formation of a tetragonal-1 FeF_3 phase containing trirutile $LiFe_2F_6$, rutile FeF_2 and trigonal FeF_3 ($R\bar{3}c$) impurities (Chapter 3). The nominal composition of $Li_xFe_2F_6$ is calculated to be $x = 0.22$ according to the capacity (Chapter 3), and 0.28 based on the AAS and ICP−AES.

The tetragonal-1 FeF_3 electrode was washed, dried, and transferred into a Na half-cell comprising a Na metal counter electrode and the Na[FSA]-[C_2C_1im][FSA] (30:70 in mol) IL electrolyte. The IL was selected for its ability to derive stable charge-discharge behavior from various electrode materials at elevated temperatures [28-30]. Electrochemical properties of the tetragonal-1 FeF_3 were investigated at room temperature in IL and organic electrolytes (Figure 5-2). At room temperature (25 °C), tetragonal-1 FeF_3 exhibits poor electrochemical activity in both electrolytes in Na system, accompanied by the curve with no distinct plateaus (Figure 5-2). The similar shape of charge-discharge curves is observed during 20 cycles with continuous capacity fading. All these observations suggest that the elevated temperature is essential in order to bring

out the electrochemical activity of tetragonal-1 FeF_3 in the Na system, in line with the report on the Li system [28-30]. Thus, the charge-discharge behavior of the tetragonal-1 FeF_3 was examined in IL electrolyte at 90 °C (Figures 5-3 and 5-4). The electrode was pre-discharged to 2.6 V (Figure 5-3a,b) and thereafter investigated in the 2.6–4.0 V (Figure 5-3c,d). The initial charge-discharge cycle attains a discharge capacity of 53.2 mAh g^{-1} and is marked by a pair of plateaus (3.8/3.6 V, see dQ/dV plot in Figure 5-3d). The plateaus correspond to a two-phase reaction caused by the reversible extraction/insertion of Na^+ from/into the tetragonal structure (Chapter 3). Although the capacity is limited, the shape of the charge-discharge curve remains unchanged during the successive 20 cycles. The CV of the Na/tetragonal-1 FeF_3 cell clearly shows the redox peaks at 3.90/3.51 V for 10 cycles (Figure 5-3e), which is consistent with the preservation of charge-discharge curves and dQ/dV plots in the same cut-off voltage during cycling (Figure 5-3c,d). Further cycling of the charge-discharge test produces superposing charge-discharge curves with no changes in shape and a reversible capacity of 47.3 mAh g^{-1} at the 50th cycle (Figure 5-3f,g). These results evince the reversible insertion reactions of the tetragonal-1 FeF_3 with 0.2 Na^+ (theoretically 118 mAh g^{-1} for 0.5e^- transfer) between 2.6–4.0 V.

The tetragonal-1 FeF_3 was further examined in the extended cutoff range of 2.3−4.0 V (Figure 5-4). A full plateau, which appears around 2.57 V during the pre-discharge to 2.3 V (Figure 5-4a,b), is noted to disappear in the subsequent sodiation

processes (Figure 5-4c,d). This one-time reduction peak corresponds to the conversion of the residual trirutile $LiFe_2F_6$ into rutile FeF_2 and alkali metal fluorides (LiF and NaF) (see Chapter 3). The first two cycles in the 2.3–4.0 V range (Figure 5-4c) produce charge-discharge curves that resemble those in the 2.6–4.0 V range, indicating analogous desodiation-sodiation behavior. However, two pairs of new plateaus are observed to emerge around 10th cycle (see the dQ/dV curves in Figure 5-4d). The CV also shows the new redox peaks after 5th cycle (Figure 5-4e), as suggested by the changes on the charge-discharge curves and dQ/dV plots in the same cut-off voltage during cycling (Figure 5-4c,d). Further cycling of the charge-discharge test shows a slight capacity fade during the initial 50 cycles, accompanied by the new plateaus emerged around 10th cycle (Figure 5-4f,g). All these observations demonstrate a gradual transition in the reaction mechanisms with continued cycling.

Figure 5-5 shows the GITT profiles of the Na/tetragonal-1 FeF_3 cell during the pre-discharge, 1st, and 10th charge-discharge cycles. The voltage after each relaxation process shows a short plateau around 2.6 V during the pre-discharge (Figure 5-5a), which is due to the conversion reaction of the residual trirutile $LiFe_2F_6$ to rutile FeF_2 and LiF as mentioned above. The voltage after relaxation during the first charge gradually increases with increasing SOC and exhibits a plateau at 3.7 V. Considering the GITT profile of the trirutile $LiFe_2F_6$ (Chapter 3), this flat plateau around 3.7 V is assigned to the two-phase reaction between Na-rich and Na-deficient tetragonal phases caused by desodiation in the

tetragonal structure. The first discharge profile is free from the short plateau at 2.6 V observed in the pre-discharge. The GITT curve at the 10th cycle (Figure 5-5b) shows different profiles from the first cycle with smaller voltage hysteresis, which evidences the change of the reaction mechanism during cycling.

For further insight into the reaction mechanisms, synchrotron XRD measurements were performed on the tetragonal-1 FeF_3 electrodes at different states of charge (SOCs) between 2.3−4.0 V (Figure 5-6). The corresponding voltage-time profile is shown in Figure 5-6a. XRD patterns A and B denote the pristine trirutile $LiFe_2F_6$ and the tetragonal-1 FeF_3 electrode, respectively (Figure 5-6b). In the work on the Li system discussed in Chapter 3, the tetragonal-1 FeF_3 and the trirutile $LiFe_2F_6$ were reported to have similar crystal structures except that the tetragonal-1 FeF_3 had a vacant 2*a* site, larger *a*- and *b*-parameters, and a smaller *c*-parameter than the trirutile $LiFe_2F_6$ (trirutile $LiFe_2F_6$: a = 4.6798(1) Å, c = 9.3095(4) Å and tetragonal-1 FeF_3: a = 4.7718(3) Å, c = 8.8557(1) Å). In the current study, pre-discharging the tetragonal-1 FeF_3 phase to 2.6 V (Pattern 1) in the Na system results in the disappearance of the tetragonal-1 phase and the appearance of multiple phases with broad diffraction peaks. Rietveld refinement of Pattern 1 (Figure 5-7a and Table 5-2) confirms that the main phase of the resulting material is related to a sodiated tetragonal Na_xFeF_3 phase formed by the topotactic insertion of Na^+ into the 2*a* site of the tetragonal-1 FeF_3 (hereafter denote as the sodiated tetragonal-1 Na_xFeF_3). The corresponding crystallographic data (Table 5-2) reveal that the sodiated tetragonal-1

Na_xFeF_3 phase has a disordered trirutile structure (where the 2*a* site is occupied by Fe with an occupancy ratio of 0.2235) with larger *a*- and *c*-parameters than those of tetragonal-1 FeF_3. One of the other phases observed is attributed to rutile FeF_2, formed by the partial sodiation of the residual trirutile $LiFe_2F_6$. Alkali fluorides (LiF and NaF) are also noted, but their peaks are too weak and broad to be included in the Rietveld refinement.

The sodiated tetragonal-1 Na_xFeF_3 and the rutile FeF_2 phases are also detected in Pattern 2, demonstrating the occurrence of topotactic Na^+ insertion into the tetragonal-1 FeF_3 followed by conversion reaction from trirutile $LiFe_2F_6$ to rutile FeF_2 and alkali fluorides during the pre-discharge to 2.3 V (Figure 5-7b and Table 5-2). In Pattern 2, a new broad peak appearing around 12.9° is assigned to the 002 diffraction of orthorhombic $NaFeF_3$ [21, 22]. This orthorhombic $NaFeF_3$ is a product of the insertion of extra Na^+ into the tetragonal-1 FeF_3, which suggests that extending the sodiation of the tetragonal-1 FeF_3 to 2.3 V engenders a structural transformation from the tetragonal structure to the orthorhombic structure.

After the initial charging to 4.0 V (Pattern 3), a sharp peak appears around 15.2°, which is related to the formation of a desodiated tetragonal phase at the high voltage. However, the diffraction peaks of this tetragonal phase show slightly shift in position compared to those of the initial tetragonal-1 FeF_3 (Pattern B). This reveals that the tetragonal-1 phase is no longer recovered by the desodiation of the multiple-phase

mixture of sodiated tetragonal-1 Na_xFeF_3 phase, rutile FeF_2, alkali metal fluorides (LiF and NaF) and the orthorhombic $NaFeF_3$. Rietveld refinement of Pattern 3 (Figure 5-7c and Table 5-2) verifies that the slightly shifted diffraction peaks can be indexed as a disordered trirutile structure (hereafter, tetragonal-2 FeF_3) wherein the 2*a* site is occupied by Fe with an occupancy ratio of 0.4357. The corresponding crystallographic data (Table 5-2) further reveal that the initial desodiation engenders a 1.2% decrease in the *a*- lattice parameter and a 6.7% increase in the *c*- lattice parameter, yielding a 4.1% larger overall volume than the initial tetragonal-1 FeF_3. In the previous study on the Li system, the tetragonal-2 FeF_3 phase was also found to exist in the charged state after the electrode was discharged to 2.5 V (Chapter 3). It is worth noting that Pattern 3 also exhibits a peak corresponding to the 012 diffraction of the trigonal FeF_3 ($R\bar{3}c$). This suggests that part of the rutile FeF_2 and the alkali metal fluorides are involved in the formation of the trigonal FeF_3 phase during the charge process [31].

After the first discharge to 2.3 V (Pattern 4), the diffraction pattern resembles that of the pre-discharged electrode (Pattern 2), except for the diffraction peaks of the orthorhombic $NaFeF_3$ which becomes stronger after one cycle, indicating that the amount of orthorhombic $NaFeF_3$ phase increases during the initial discharge. Rietveld refinement of Pattern 4 (Figure 5-7d and 5-2) also reveals the presence of a sodiated tetragonal Na_xFeF_3 phase with lattice parameters similar to the tetragonal-1 Na_xFeF_3 phase, confirming that the tetragonal-2 FeF_3 is re-sodiated back to tetragonal-1 Na_xFeF_3.

At the charged state of the 10th cycle (Pattern 5), the 100 diffraction peak belonging to the cubic FeF_3 ($Pm\bar{3}m$) is observed at 13.3° [23], which confirms that the new reaction previously visualized by the new charge-discharge curves is related to a reversible phase transformation from the orthorhombic $NaFeF_3$ (*Pnma*) phase to the cubic FeF_3 ($Pm\bar{3}m$) phase along with desodiation. This is consistent with the previous study on the charge-discharge behavior of the nano-sized orthorhombic $NaFeF_3$ [23, 24]. Pattern 5 also highlights the presence of a tetragonal phase (hereafter, tetragonal-3 FeF_3) which exhibits a disordered trirutile structure akin to the tetragonal-2 FeF_3, despite their different lattice parameters due to different Fe occupancies (Figure 5-7e and Table 5-2).

At the discharged state of the 10th cycle (Pattern 6), diffraction peaks related to the sodiated tetragonal Na_xFeF_3, orthorhombic $NaFeF_3$ and rutile FeF_2 are observed. The crystal structure of the sodiated tetragonal Na_xFeF_3 phase is analogous to that of the sodiated tetragonal-1 Na_xFeF_3 but with different lattice parameters (Figure 5-7f and Table 5-2). The formation of the sodiated tetragonal Na_xFeF_3 phase, hereafter denoted as sodiated tetragonal-3 Na_xFeF_3, evinces that the topotactic insertion/extraction of Na^+ into/from the tetragonal phase continues to occur during the sodiation-desodiation processes after 10 cycles. The presence of the rutile FeF_2 throughout the charge-discharge cycles denotes its partially inactive electrochemical nature, consistent with the observations made in the previous work on trirutile $LiFe_2F_6$ (Chapter 3).

Figure 5-8 summarizes the charge-discharge mechanisms of the tetragonal-1 FeF_3 in the Na system and the changes occurring during cycling in the 2.3−4.0 V range. First two cycles yield a pair of plateaus around 3.7 V, engendered by a sodiation-desodiation process which mainly involves the topotactic Na^+ insertion/extraction reaction into/from tetragonal-type FeF_3. A conversion reaction from the trirutile $LiFe_2F_6$ to rutile FeF_2 with alkali metal fluorides and transformation to the orthorhombic $NaFeF_3$ also occur during sodiation, whereas rutile FeF_2 is partially converted to trigonal FeF_3 during the successive desodiation. The two initial cycles only produce small amounts of orthorhombic $NaFeF_3$. However, its quantity formed at 2.3 V progressively increase with continued cycling due to the poor reversibility of the orthorhombic to tetragonal phase transformation. After 10 cycles, the sodiation-desodiation process partially changes to reversible Na^+ insertion and extraction between cubic FeF_3 and orthorhombic $NaFeF_3$ phases—a transition marked by the emergence of new charge-discharge curves, while along with the reversible insertion/extraction reaction into/from the tetragonal phase. It is worth noting that a disordered trirutile structure derived from the starting trirutile structure is discerned at different charged states of the electrode.

5.4 Conclusions

In summary, for the first time, a trirutile-derived FeF_3 phase is reported as a positive electrode for SIBs. The formation of disordered trirutile Na_xFeF_3 is confirmed by the

presence of a sodiated tetragonal Na_xFeF_3 in the discharged state of the electrode. This work also shed light on the reaction mechanisms of the Na-Fe-F system by elucidating the structural transition between the tetragonal-1 FeF_3 and the cubic FeF_3 phases in the charged states of the electrode during cycling. However, the sodiation-desodiation processes are mired in unexpected reactions caused by impurity phases formed during the preparation of the starting material. Therefore, it is postulated that future investigations using a composite of pure-phased sodium iron fluoride with the tetragonal structure would provide a better perspective of the Na-Fe-F system.

Table 5-1 Summary of selected works on FeF_3 and $NaFeF_3$ positive electrodes for sodium-ion batteries.

Year	Existent form	Preparation method	Initial discharge capacity	Crystallographic and electrochemical properties
2009 [11]	Trigonal FeF_3 (S.G. $R\bar{3}c$)	Commercial reagent	145 mAh g^{-1} at 1.5 V (A rate of 0.2 mA cm^{-2})	Reversible Fe^{3+}/Fe^{2+} redox reaction
2011 [32]	Orthorhombic $NaFeF_3$ (S.G. *Pnma*)	Liquid-phase synthesis	153 mAh g^{-1} between 1.5−4.5 V (19.7 mA g^{-1})	None
2012 [33]	Orthorhombic $NaFeF_3$ (S.G. *Pnma*)	Solid-state method	126 mAh g^{-1} between 1.5−4.0 V (A rate of 0.076 mA cm^{-2})	The extraction/insertion of sodium by the reversible lattice vibration
2013 [34]	Orthorhombic $NaFeF_3$ (S.G. *Pnma*)	Solid-state method	225 mAh g^{-1} between 1.5−4.5 V (7.5 mA g^{-1})	$NaFeF_3$ → Charged state $FeF_3 + Na^+ + e^-$ (Reversible Na^+ reinsertion)
2013 [13]	Orthorhombic $FeF_3{\cdot}0.33H_2O$ (S.G. *Cmcm*)	Solid-solid breakdown method	130 mAh g^{-1} at 1.2 V (23.7 mA g^{-1})	None
2014 [20]	In situ generated FeF_3 from FeF_2–RGO	Electrochemical activation	150 mAh g^{-1} at 1.5 V (50 mA g^{-1})	$FeF_3 + Na^+ \rightleftarrows NaFeF_3$
2014 [21]	Orthorhombic $NaFeF_3$ (S.G. *Pnma*)	First-principle density functional theory calculations	None	Orthorhombic $NaFeF_3$ → Orthorhombic $Na_{0.5}FeF_3 + 0.5\ Na^+ + 0.5\ e^-$ → Orthorhombic $FeF_3 + 0.5\ Na^+ + 0.5\ e^-$
2017 [16]	Trigonal FeF_3 (S.G. $R\bar{3}c$)	Single-source molecular precursors	160 mAh g^{-1} at 1.6 V (200 mA g^{-1})	Assume a similar mechanism with the work [20]
2017 [22]	Orthorhombic $NaFeF_3$ (S.G. *Pnma*)	Ball milling; density functional calculation	169 mAh g^{-1} at 2 V (A rate of 0.1 mA cm^{-2})	$FeF_3 + Na^+ \rightarrow Na_{0.5}FeF_3 + 0.5\ Na^+ \rightarrow NaFeF_3$
2018 [17]	Orthorhombic $FeF_3{\cdot}0.33H_2O$ (S.G. *Cmcm*)	Hydrothermal method	244 mAh g^{-1} at 1 V (20 mA g^{-1})	$FeF_3 + Na^+ \rightarrow NaFeF_3$ (4−1.2 V); $NaFeF_3 + 2\ Na^+ \rightarrow 3\ NaF + Fe$ (1.2−1.0 V)
2018 [23]	Orthorhombic $NaFeF_3$ (S.G. *Pnma*)	Microwave-assisted solution synthesis	150 mAh g^{-1} between 2.0−4.0 V (19.7 mA g^{-1})	$NaFeF_3 \rightleftarrows$ Cubic FeF_3 (S.G. $Pm\bar{3}m$) + $Na^+ + e^-$ (Insertion/deinsertion mechanism)

Table 5-2 Crystallographic parameters of the tetragonal phases for Pattern 1, Pattern 2, Pattern 3, Pattern 4, Pattern 5 and Pattern 6 in Figure 5-6 obtained by Rietveld refinement.

Refinement results for the sodiated tetragonal-1 Na_xFeF_3 phase in Pattern 1[a] (S.G. $P4_2/mnm$)
R_p = 2.93%, R_{wp} = 3.87%

a = 4.8267(6) Å		c = 9.572(2) Å			V = 223.00(6) Å^3	
Atom	Wyckoff symbol	x	y	z	Biso / Å^2	Occup.
Na	2a	0	0	0	0.5	0.6016
Fe	2a	0	0	0	0.5	0.2235
Fe	4e	0	0	0.3184(7)	0.5	0.8883
F1	4f	0.327(1)	0.327(1)	0	0.5	1
F2	8j	0.2728(9)	0.2728(9)	0.3585(8)	0.5	1

Refinement results for the sodiated tetragonal-1 Na_xFeF_3 phase in Pattern 2[b] (S.G. $P4_2/mnm$)
R_p = 3.12%, R_{wp} = 3.94%

a = 4.846(1) Å		c = 9.596(5) Å			V = 225.4(1) Å^3	
Atom	Wyckoff symbol	x	y	z	Biso / Å^2	Occup.
Na	2a	0	0	0	0.5	0.6493
Fe	2a	0	0	0	0.5	0.2815
Fe	4e	0	0	0.316(2)	0.5	0.8592
F1	4f	0.316(4)	0.316(4)	0	0.5	1
F2	8j	0.247(3)	0.247(3)	0.366(2)	0.5	1

Refinement results for the tetragonal-2 FeF_3 phase in Pattern 3[c] (S.G. $P4_2/mnm$)
R_p = 4.46%, R_{wp} = 5.99%

a = 4.713(1) Å		c = 9.450(2) Å			V = 209.87(9) Å^3	
Atom	Wyckoff symbol	x	y	z	Biso / Å^2	Occup.
Fe	2a	0	0	0	0.5	0.4357
Fe	4e	0	0	0.3176(7)	0.5	0.7822
F1	4f	0.324(1)	0.324(1)	0	0.5	1
F2	8j	0.2796(9)	0.2796(9)	0.3652(6)	0.5	1

Refinement results for the sodiated tetragonal-1 Na_xFeF_3 phase in Pattern 4[d] (S.G. $P4_2/mnm$)
R_p = 3.45%, R_{wp} = 4.28%

a = 4.843(1) Å		c = 9.600(6) Å			V = 225.1(1) Å^3	
Atom	Wyckoff symbol	x	y	z	Biso / Å^2	Occup.
Na	2a	0	0	0	0.5	0.6535
Fe	2a	0	0	0	0.5	0.3011
Fe	4e	0	0	0.345(2)	0.5	0.8495
F1	4f	0.301(5)	0.301(5)	0	0.5	1
F2	8j	0.261(4)	0.261(4)	0.297(2)	0.5	1

Refinement results for the tetragonal-3 FeF_3 phase in Pattern 5[e] (S.G. $P4_2/mnm$)
R_p = 4.28%, R_{wp} = 5.70%

a = 4.7018(9) Å		c = 9.760(3) Å			V = 215.8(1) Å^3	
Atom	Wyckoff symbol	x	y	z	Biso / Å^2	Occup.
Fe	2a	0	0	0	0.5	0.5013
Fe	4e	0	0	0.3209(9)	0.5	0.7493
F1	4f	0.231(2)	0.231(2)	0	0.5	1
F2	8j	0.332(1)	0.332(1)	0.2987(9)	0.5	1

Refinement results for the sodiated tetragonal-3 Na_xFeF_3 phase in Pattern 6[f] (S.G. $P4_2/mnm$)
R_p = 2.88%, R_{wp} = 4.03%

a = 4.720(1) Å		c = 9.866 (5) Å			V = 219.8(1) Å^3	
Atom	Wyckoff symbol	x	y	z	Biso / Å^2	Occup.
Na	2a	0	0	0	0.5	0.4034
Fe	2a	0	0	0	0.5	0.4415
Fe	4e	0	0	0.336(2)	0.5	0.7793
F1	4f	0.227(3)	0.227(3)	0	0.5	1
F2	8j	0.294(2)	0.294(2)	0.373(1)	0.5	1

[a]The rutile FeF_2 ($P4_2/mnm$) is considered to be impurity phase. [b]The rutile FeF_2 ($P4_2/mnm$) and orthorhombic $NaFeF_3$ ($Pnma$) are considered to be impurity phases. [c]The rutile FeF_2 ($P4_2/mnm$) and trigonal FeF_3 ($R\bar{3}c$) are considered to be impurity phases. [d]The rutile FeF_2 ($P4_2/mnm$) and orthorhombic $NaFeF_3$ ($Pnma$) are considered to be impurity phases. [e]The cubic FeF_3 ($Pm\bar{3}m$) and rutile FeF_2 ($P4_2/mnm$) are considered to be impurity phases. [f]The orthorhombic $NaFeF_3$ ($Pnma$) and rutile FeF_2 ($P4_2/mnm$) are considered to be impurity phases.

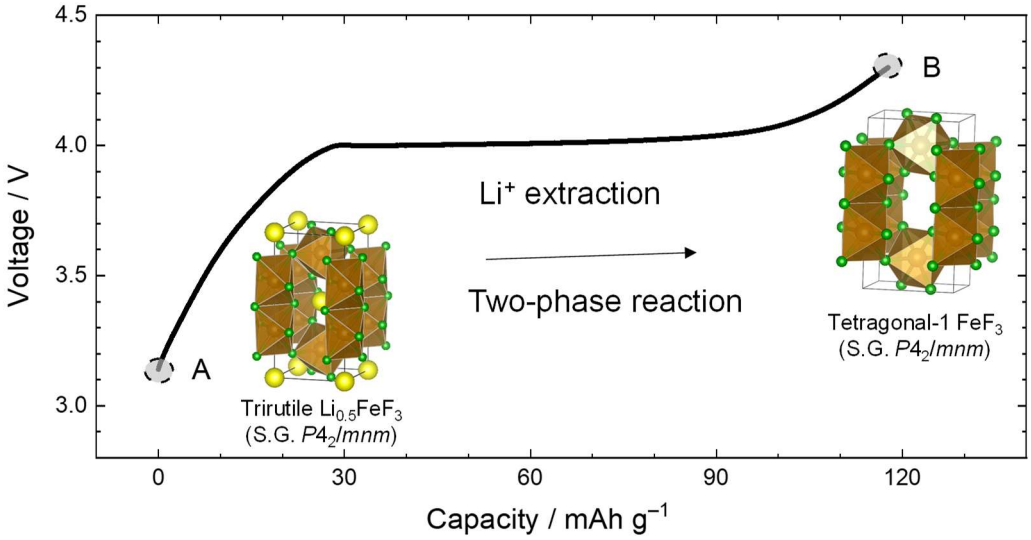

Figure 5-1 Schematic illustration of preparing tetragonal-1 FeF_3 electrode.

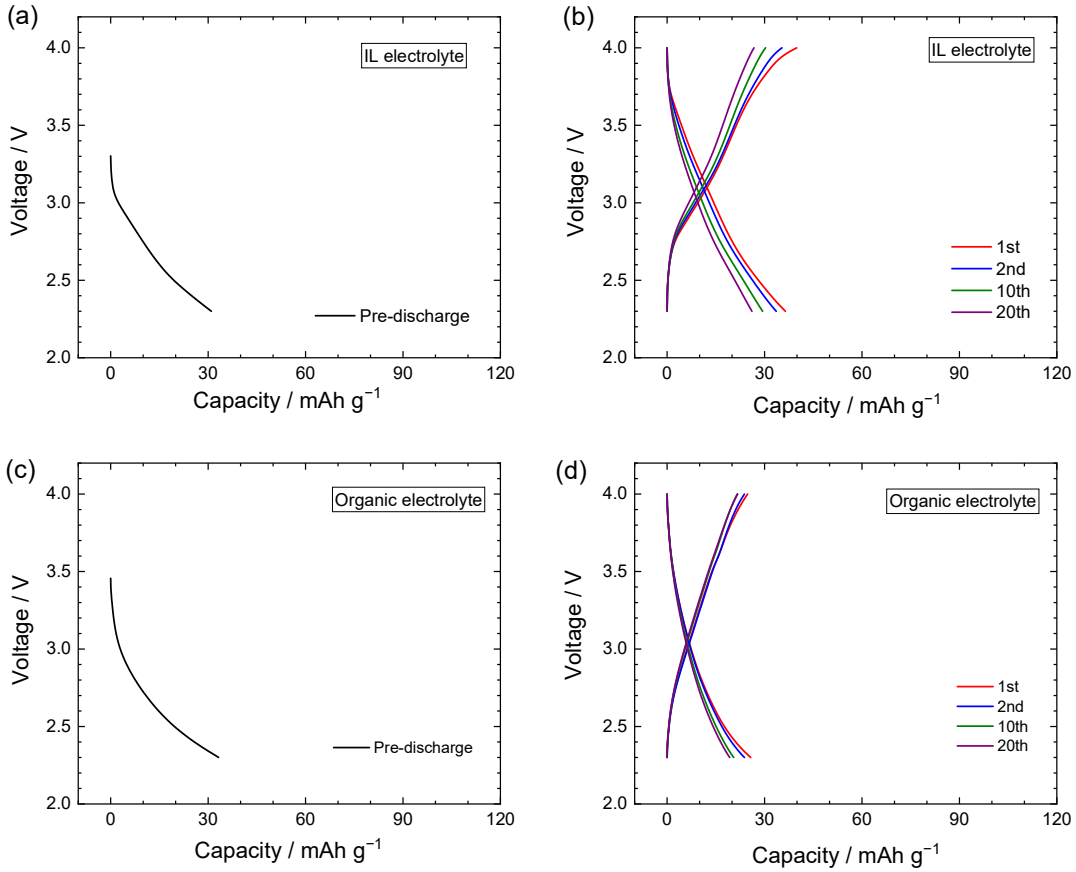

Figure 5-2 Charge-discharge curves of the Na/tetragonal-1 FeF_3 cell at 25 °C. (a) The pre-discharge curve and (b) the subsequent charge-discharge curves for the 1st, 2nd, 10th and 20th cycles in Na[FSA]-[C_2C_1im][FSA] (30:70 in mol) IL electrolyte. (c) The pre-discharge curve and (d) the subsequent charge-discharge curves for the 1st, 2nd, 10th and 20th cycles in 1 M $NaPF_6$/EC:DMC. Current density: 21.4 mA g^{-1}. Cut-off voltage: 2.3−4.0 V.

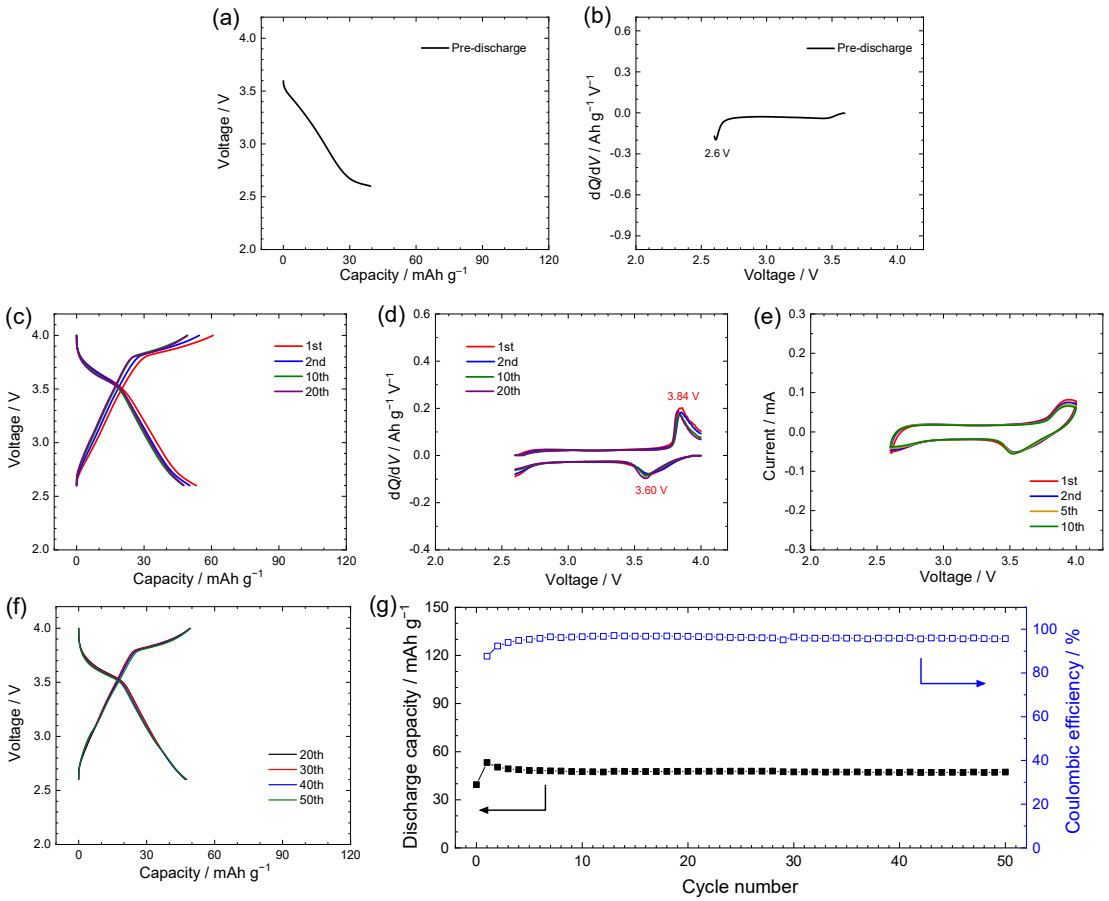

Figure 5-3 Electrochemical properties of the Na/tetragonal-1 FeF_3 cell in the cut-off voltage of 2.6–4.0 V. (a) The pre-discharge curve to 2.6 V. (b) The dQ/dV plots corresponding to the pre-discharge curve in (a). (c) Charge-discharge curves of 1st, 2nd, 10th and 20th cycles. (d) The corresponding dQ/dV plots of the charge-discharge curves in (c). (e) CV at a scan rate of 0.1 mV s^{-1}. (f) Charge-discharge curves of the Na/tetragonal-1 FeF_3 cell at the 20th, 30th, 40th, and 50th cycles. (g) the corresponding cycling performance for 50 cycles. Electrolyte: Na[FSA]-[C_2C_1im][FSA] (30:70 in mol) IL. Temperature: 90 °C. Current density for charge-discharge test: 21.4 mA g^{-1}.

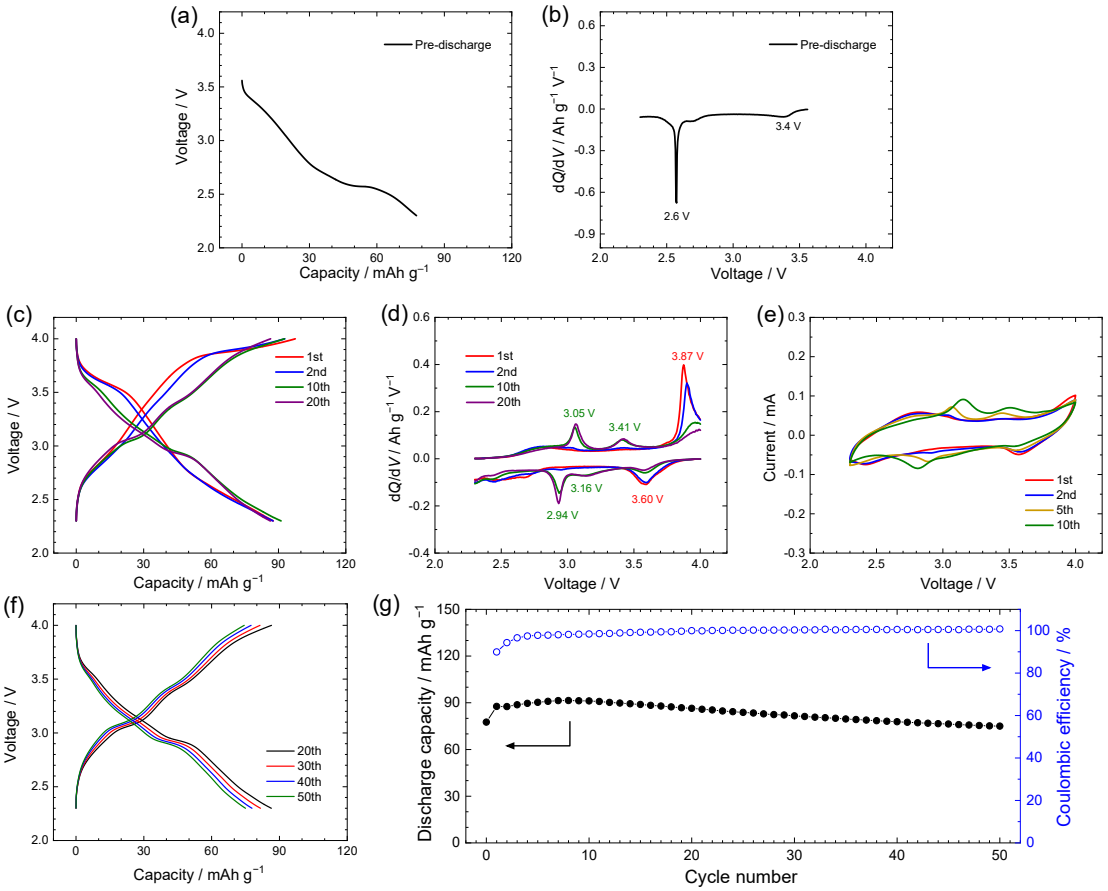

Figure 5-4 Electrochemical properties of the Na/tetragonal-1 FeF_3 cell in the cut-off voltage of 2.3−4.0 V. (a) The pre-discharge curve to 2.3 V. (b) The dQ/dV plots corresponding to the pre-discharge curve in (a). (c) Charge-discharge curves of 1st, 2nd, 10th and 20th cycles. (d) The corresponding dQ/dV plots of the charge-discharge curves in (c). (e) CV at a scan rate of 0.1 mV s^{-1}. (f) Charge-discharge curves of the Na/tetragonal-1 FeF_3 cell at the 20th, 30th, 40th, and 50th cycles. (g) the corresponding cycling performance for 50 cycles. Electrolyte: Na[FSA]-[C_2C_1im][FSA] (30:70 in mol) IL. Temperature: 90 °C. Current density for charge-discharge test: 21.4 mA g^{-1}.

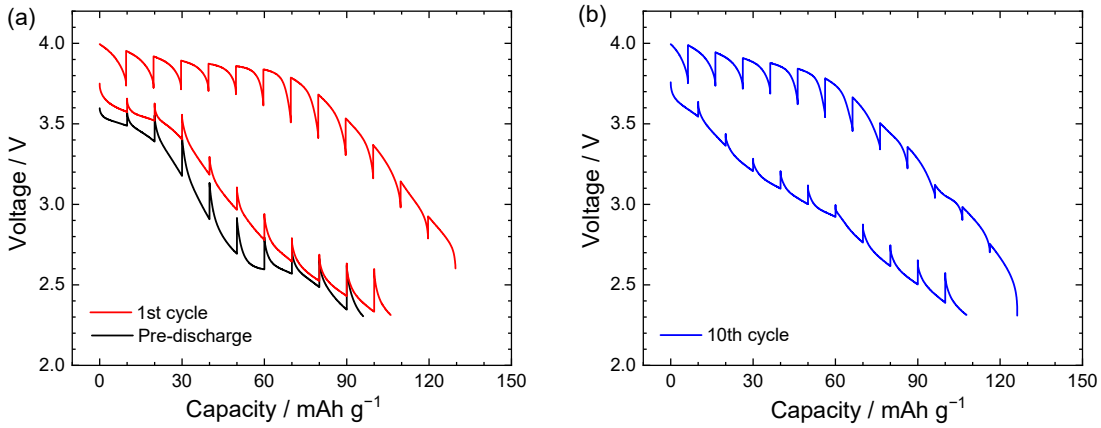

Figure 5-5 The GITT profile of the Na/tetragonal-1 FeF_3 cell in the cut-off voltage of 2.3−4.0 V. (a) Pre-discharge and 1st cycle. (b) 10th cycle after 9 cycles of galvanostatic charge-discharge at 21.4 mA g^{-1}. Electrolyte: Na[FSA]-[C_2C_1im][FSA] (30:70 in mol). Temperature: 90 °C.

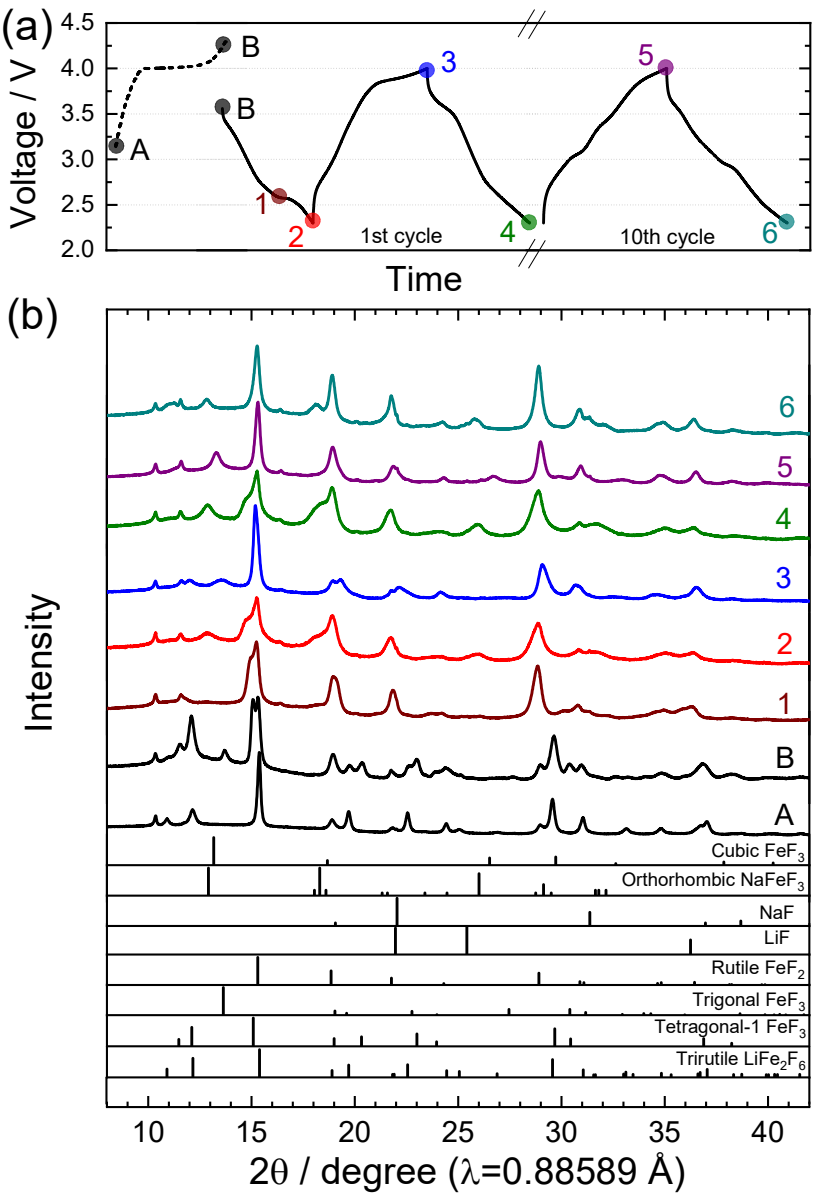

Figure 5-6 (a) A voltage-time profile of the XRD samples at different SOCs. (b) Synchrotron XRD patterns of the tetragonal-1 FeF_3 at different SOCs in comparison with the initial trirutile $LiFe_2F_6$. (1) Pre-discharged state at 2.6 V, (2) pre-discharged state at 2.3 V, (3) initial charged state at 4.0 V, (4) initial discharged state at 2.3 V, (5) 10th cycle charged state at 4.0 V and (6) 10th cycle discharged state at 2.3 V. Dashed line in (a) indicates the charge-discharge curve of the trirutile $LiFe_2F_6$ in the Li system. Solid line in (a) indicates the charge-discharge curve(s) of the tetragonal-1 FeF_3 in the Na system.

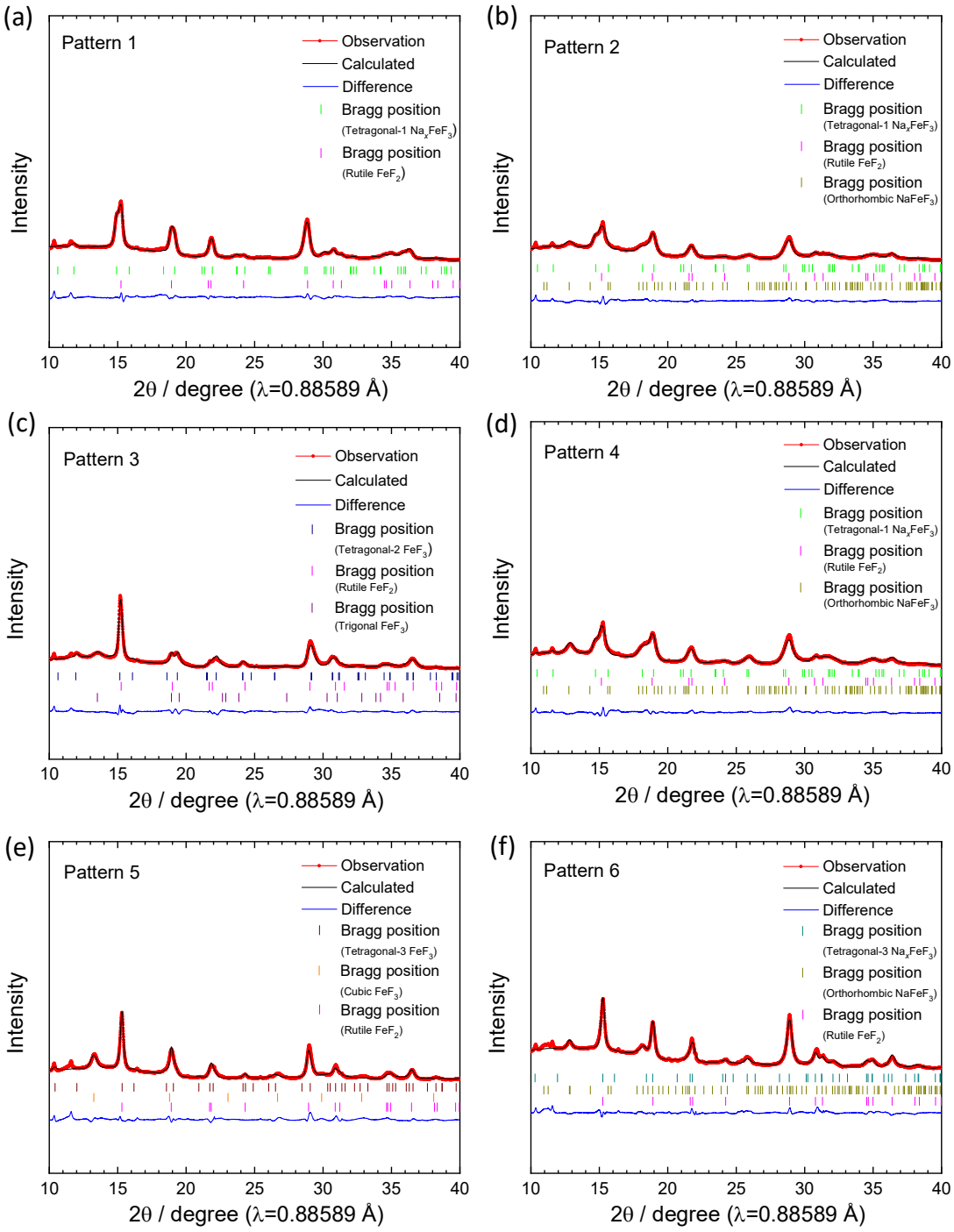

Figure 5-7 The Rietveld refinement results of tetragonal phases in (a) Pattern 1, (b) Pattern 2, (c) Pattern 3, (d) Pattern 4, (e) Pattern 5 and (f) Pattern 6 in Figure 5-6.

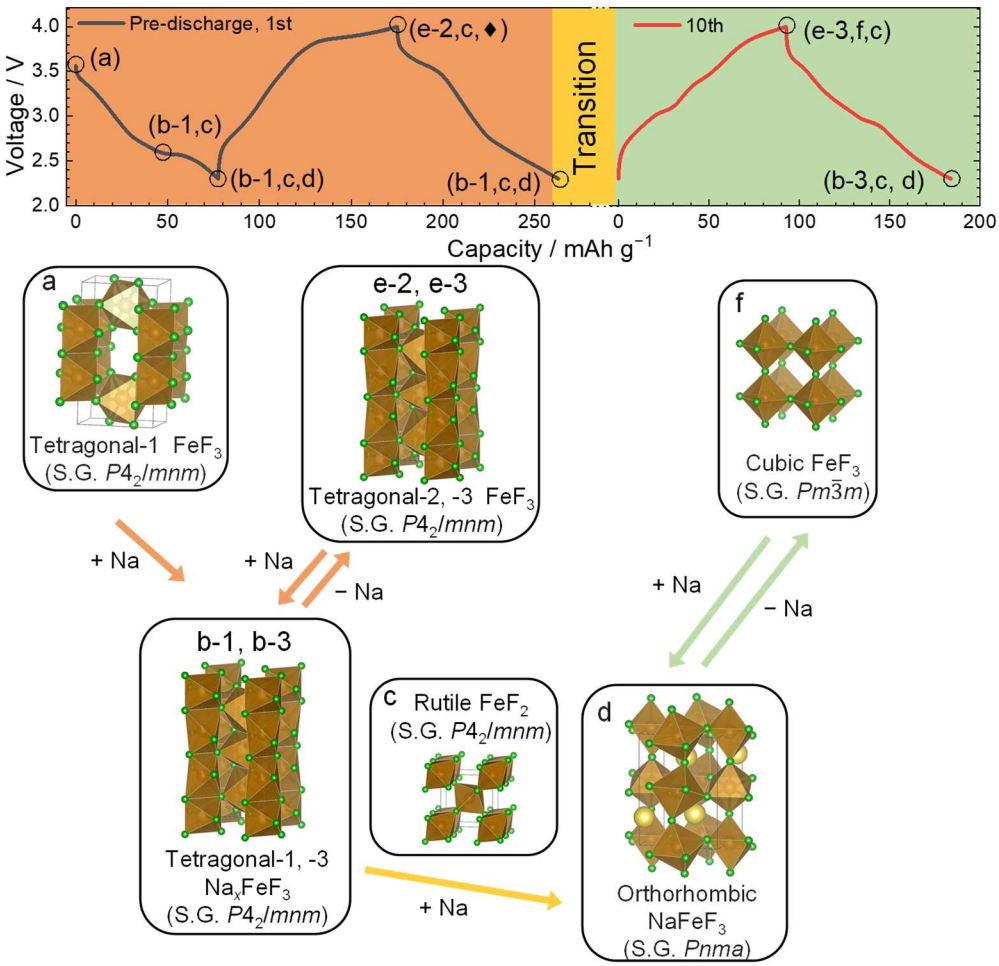

Figure 5-8 A schematic illustration of the reaction mechanisms of the tetragonal-1 FeF_3 during the sodiation-desodiation and the concomitant structural transition to the cubic FeF_3 phase. The b-1 and b-3 correspond to tetragonal-1 and -3 Na_xFeF_3 phases, respectively. The e-2 and e-3 correspond to tetragonal-2 and -3 FeF_3 phases, respectively. Desodiation from orthorhombic $NaFeF_3$ to tetragonal Na_xFeF_3 is limited, as orthorhombic $NaFeF_3$ tends to be desodiated into the cubic FeF_3. The formation of trigonal FeF_3, designated by ♦ in the figure, is a one-time occurrence.

References

[1] D. Larcher, J.M. Tarascon, Nat. Chem., 7 (2015) 19−29.

[2] C.P. Grey, J.M. Tarascon, Nat. Mater., 16 (2016) 45−56.

[3] P.K. Nayak, L. Yang, W. Brehm, P. Adelhelm, Angew. Chem. Int. Ed. Engl., 57 (2018) 102−120.

[4] F. Badway, N. Pereira, F. Cosandey, G.G. Amatucci, J. Electrochem. Soc., 150 (2003) A1209−A1218.

[5] R.E. Doe, K.A. Persson, Y.S. Meng, G. Ceder, Chem. Mater., 20 (2008) 5274–5283.

[6] N. Yamakawa, M. Jiang, B. Key, C.P. Grey, J. Am. Chem. Soc., 131 (2009) 10525−10536.

[7] N. Yabuuchi, M. Sugano, Y. Yamakawa, I. Nakai, K. Sakamoto, H. Muramatsu, S. Komaba, J. Mater. Chem., 21 (2011) 10035.

[8] L. Li, R. Jacobs, P. Gao, L. Gan, F. Wang, D. Morgan, S. Jin, J. Am. Chem. Soc., 138 (2016) 2838–2848.

[9] X. Hua, A.S. Eggeman, E. Castillo-Martinez, R. Robert, H.S. Geddes, Z. Lu, C.J. Pickard, W. Meng, K.M. Wiaderek, N. Pereira, G.G. Amatucci, P.A. Midgley, K.W. Chapman, U. Steiner, A.L. Goodwin, C.P. Grey, Nature Mater., (2021) 841–850.

[10] V. Murugesan, J.S. Cho, N. Govind, A. Andersen, M.J. Olszta, K.S. Han, G. Li, H. Lee, D.M. Reed, V.L. Sprenkle, S. Cho, S.K. Nune, D. Choi, ACS Appl. Energy Mater. , 2 (2019) 1832−1843.

[11] M. Nishijima, I.D. Gocheva, S. Okada, T. Doi, J.-i. Yamaki, T. Nishida, J. Power

Sources, 190 (2009) 558–562.

[12] C. Li, C. Yin, L. Gu, R.E. Dinnebier, X. Mu, P.A. van Aken, J. Maier, J. Am. Chem. Soc., 135 (2013) 11425−11428.

[13] C. Li, C. Yin, X. Mu, J. Maier, Chem. Mater., 25 (2013) 962–969.

[14] Y. Shen, X. Wang, H. Hu, M. Jiang, X. Yang, H. Shu, J. Power Sources, 283 (2015) 204−210.

[15] S. Wei, X. Wang, M. Jiang, R. Zhang, Y. Shen, H. Hu, J. Alloys Compd., 689 (2016) 945−951.

[16] C.P. Guntlin, T. Zünd, K.V. Kravchyk, M. Wörle, M.I. Bodnarchuk, M.V. Kovalenko, J. Mater. Chem. A, 5 (2017) 7383−7393.

[17] R. Zhang, X. Wang, X. Wang, M. Liu, S. Wei, Y. Wang, H. Hu, J. Electrochem. Soc., 165 (2018) A89−A96.

[18] M. Liu, L. Liu, M. Li, B. Chen, H. Lei, H. Hu, X. Wang, J. Alloys Compd., 829 (2020) 1−10.

[19] Z. Sun, W. Fu, M.Z. Liu, P. Lu, E. Zhao, A. Magasinski, M. Liu, S. Luo, J. McDaniel, G. Yushin, J. Mater. Chem. A, 8 (2020) 4091−4098.

[20] D.-l. Ma, H.-g. Wang, Y. Li, D. Xu, S. Yuan, X.-l. Huang, X.-b. Zhang, Y. Zhang, Nano Energy, 10 (2014) 295–304.

[21] S. Yu, P. Zhang, S.Q. Wu, A.Y. Li, Z.Z. Zhu, Y. Yang, J. Solid State Electrochem., 18 (2014) 2071–2075.

[22] A. Kitajou, Y. Ishado, T. Yamashita, H. Momida, T. Oguchi, S. Okada, Electrochim.

Acta, 245 (2017) 424−429.

[23] A. Martin, M.-L. Doublet, E. Kemnitz, N. Pinna, Adv. Funct. Mater., 28 (2018) 1−7.

[24] A. Martin, E.S. Santiago, E. Kemnitz, N. Pinna, ACS Appl. Mater. Interfaces, 11 (2019) 33132−33139.

[25] B.H. Toby, J. Appl. Cryst., 34 (2001) 210−213.

[26] K. Momma, F. Izumi, J. Appl. Crystallogr., 44 (2011) 1272−1276.

[27] K. Matsumoto, E. Nishiwaki, T. Hosokawa, S. Tawa, T. Nohira, R. Hagiwara, J. Phys. Chem. C, 121 (2017) 9209–9219.

[28] K. Matsumoto, T. Hosokawa, T. Nohira, R. Hagiwara, A. Fukunaga, K. Numata, E. Itani, S. Sakai, K. Nitta, S. Inazawa, J. Power Sources, 265 (2014) 36–39.

[29] J. Hwang, K. Matsumoto, R. Hagiwara, Adv. Sustainable Syst., 2 (2018) 1700171.

[30] K. Matsumoto, J. Hwang, S. Kaushik, C.-Y. Chen, R. Hagiwara, Energy Environ. Sci., 12 (2019) 3247–3287.

[31] S. Tawa, Y. Sato, Y. Orikasa, K. Matsumoto, R. Hagiwara, J. Power Sources, 412 (2019) 180–188.

[32] Y. Yamada, T. Doi, I. Tanaka, S. Okada, J.-i. Yamaki, J. Power Sources, 196 (2011) 4837–4841.

[33] A. Kitajou, H. Komatsu, K. Chihara, I.D. Gocheva, S. Okada, J.-i. Yamaki, J. Power Sources, 198 (2012) 389–392.

[34] N. Dimov, A. Nishimura, K. Chihara, A. Kitajou, I.D. Gocheva, S. Okada,

Electrochim. Acta, 110 (2013) 214−220.

Chapter 6

Phase Transformation of Orthorhombic $NaFeF_3$ in Na-ion Batteries

6.1 Introduction

The phase evolution in the Li-Fe-F system has been long-discussed to explore the lithiation mechanism of trigonal FeF_3 ($R\bar{3}c$). The initial lithium insertion was reported to lead to a phase transition to trirutile $Li_{0.5}FeF_3$ ($P4_2/mnm$) structure in which the FeF_6 octahedra share corners and edges. Further lithiation into the trirutile $Li_{0.5}FeF_3$ phase results in conversion to LiF and FeF_2 *via* complicated displacement reaction mechanisms [1-3], and the reversible conversion reaction from the LiF/FeF_2 mixture to FeF_3 during the delithiation is also confirmed [4]. For deep lithiation, FeF_2 reacts with two Li^+ ions to trigger the conversion reaction from FeF_2 to zero-valent Fe and LiF [3, 5].

In contrast to the status of the research progress in the Li-Fe-F system, the phase evolution in the Na-Fe-F system is poorly understood [6-15]. According to the density functional theory (DFT) calculations on the desodiation properties of orthorhombic $NaFeF_3$, the orthorhombic $Na_{0.5}FeF_3$ (*Pnma*) phase is only the energetically stable intermediate phase during one-electron reaction between the orthorhombic $NaFeF_3$ (*Pnma*) and fully desodiated orthorhombic FeF_3 (*Pnma*) [16, 17]. A previous study reported the desodiation from orthorhombic $NaFeF_3$ nanoparticles turns into a cubic FeF_3

($Pm\bar{3}m$) with a framework of corner-shared FeF_6 octahedra [18]. Other works employing FeF_3 as the starting material reported the transformation from FeF_3 to $NaFeF_3$, but could not prove the phase structure and the existence of any intermediate Na_xFeF_3 phase during the sodiation process [13, 19]. Although the research on the Na-Fe-F system has increased in recent years, the intermediate $Na_{0.5}FeF_3$ phase was not firmly detected and discussed in previous experimental works. Employing orthorhombic $NaFeF_3$ as the starting material is considered to be a reasonable research scheme to get a better understanding on the detailed phase evolution in the Na-Fe-F system because its electrochemical activity was confirmed as described above.

This study employs the orthorhombic $NaFeF_3$ as the positive electrode for SIBs. Its electrochemical properties are investigated at an elevated temperature to facilitate (de)sodiation process for revealing phase evolution in thermally and chemically stable IL electrolytes. Previous works revealed a range of IL electrolytes are useful in applications of SIBs in a wide temperature range by forming stable solid-electrolyte interphase [20-28]. The detailed phase evolution including the formation of the intermediate $Na_{0.5}FeF_3$ phase was determined through GITT and XRD measurements. The inherent performance of $NaFeF_3$ is discussed in details based on the data obtained in order to provide a material-design platform for fundamental studies and further understanding of the Na-Fe-F system.

6.2 Experimental

Orthorhombic $NaFeF_3$ was prepared in the following manner (see Figure 6-1a for the schematic of this procedure). Equimolar amounts for NaF and FeF_2 were weighed and loaded in an airtight bowl with a zirconia inner wall under the dry Ar atmosphere. The mixture around 1 g was then ball-milled in a planetary ball mill at 600 rpm for 6 h with zirconia balls. After the ball milling process, the bowl was opened in the glovebox, and the sample (Pre-$NaFeF_3$) was transferred into a nickel boat. The nickel boat was sealed in a stainless-steel pipe with a valve in the glovebox, and the entire pipe was connected to a vacuum line. The Pre-$NaFeF_3$ was heated under vacuum at 600 °C for 24 h. After the heating, the target sample of orthorhombic $NaFeF_3$ (H-$NaFeF_3$) was collected in the glovebox. The H-$NaFeF_3$ was then ball-milled with AB (75:25 in weight) in order to enhance electronic conductivity for electrochemical measurements ($NaFeF_3$@C).

The PTFE binder was thoroughly mixed with $NaFeF_3$@C ($NaFeF_3$@C:PTFE = 95:5 in weight) using an agate mortar and a pestle to form a homogeneous electrode sheet. The sheet was pressed onto Al mesh (13 mm in diameter) to prepare the test electrode with a loading mass of ~ 3 mg cm^{-2}. Coin cells (2032-type) were assembled in the Ar-filled glovebox with the $NaFeF_3$ working electrode, the Na[FSA]-[C_2C_1im][FSA] (20:80 in mol) IL electrolyte [22], and the Na metal disk counter electrode pressed on Al plate current collector. The glass microfiber separator was immersed in the IL electrolyte under vacuum at 90 °C for 12 h prior to cell assembling.

All the electrochemical data were obtained by an HJ-SD8 charge−discharge

system. The charge−discharge curves and cycling performance of the working electrode were measured by galvanostatic charge−discharge tests. In this study, the capacity of the positive electrode is shown as a value per weight (in grams) of $NaFeF_3$. The overpotentials of the electrode was assessed by GITT where the voltage relaxation was repeatedly monitored in the open-circuit state immediately after charging or discharging to a certain voltage. Symmetric cells (2032 coin-type) were assembled for EIS measurements employing the charged electrodes (SOC: 50%) obtained in half-cells using the IL electrolyte at 25 °C and 90 °C, respectively. The EIS spectra during cycling were measured in half-cell at 3.2 V during the charging step of the *n*th cycle (n = 0, 1, 10, 20, 50, and 100) when the half-cells were cycled at a rate of 100 mA g^{-1}. The EIS measurements were performed using a VSP potentiostat at the corresponding temperature over a frequency range from 10 mHz–100 kHz with a perturbation amplitude of 10 mV.

The XRD patterns of $NaFeF_3$ at different synthetic stages were recorded in the Bragg−Brentano geometry using a Rigaku MiniFlex diffractometer with Ni-filtered Cu-*K*α radiation (30 kV and 10 mA) and a Si-strip high-speed detector at a scan rate of 1 deg min^{-1}. The morphology of the prepared $NaFeF_3$ powder was identified *via* field-emission SEM. Elemental distribution over the $NaFeF_3$ electrode was obtained by EDX mapping. Detailed structural parameters of the $NaFeF_3$ electrodes at different SOCs were obtained by synchrotron XRD analysis at the BL5S2 of the Aichi Synchrotron Radiation Center equipped with a PILATUS 100 K two-dimensional detector with a wavelength of 0.88603

Å. The electrode powders washed with THF and vacuum-dried at room temperature were sealed in Lindeman glass capillaries. Structural parameters were refined with the Rietveld refinement by curve-fitting using the GSAS data analysis software [29]. The crystal structure was visualized by the VESTA program [30].

6.3 Results and discussion

The preparative method of orthorhombic $NaFeF_3$ is summarized in Figure 6-1a. The comparison of the XRD patterns of the samples obtained during the preparation process is shown in Figure 6-1b. Several broad peaks assigned to orthorhombic $NaFeF_3$, FeF_2, and NaF are observed after ball-milling of NaF and FeF_2 (Figure 6-1b (1)), suggesting the ball milling process does not complete the formation of orthorhombic $NaFeF_3$ (this sample is called Pre-$NaFeF_3$). Upon heat treatment at 600 °C for 24 h (Figure 6-1b (2)), the diffraction peaks of orthorhombic $NaFeF_3$ become significantly sharper and the peaks assigned to FeF_2 and NaF disappear, confirming the pure orthorhombic $NaFeF_3$ phase (this sample is called H-$NaFeF_3$). Rietveld refinement was employed for further analyzing the lattice parameters of the obtained H-$NaFeF_3$. The refinement results are shown in Figure 6-2a and the corresponding crystallographic parameters are summarized in Table 6-1. The XRD pattern is well-fitted with the perovskite-related $NaFeF_3$ in the *Pnma* space group. Further ball-milling of H-$NaFeF_3$ with AB to enhance electronic conduction for electrochemical tests results in peak broadening (Figure 6-1b (3)) (this sample is called

$NaFeF_3$@C). Nevertheless, Rietveld refinement (Figure 6-2b) confirmed $NaFeF_3$@C preserves an orthorhombic structure. Compared with H-$NaFeF_3$, the lattice parameters of the $NaFeF_3$@C change slightly by ball-milling, but the change is tiny (Figure 6-2c and Table 6-1). It demonstrates that the ball-milling process for carbon coating does not destroy the crystal structure of the pristine orthorhombic $NaFeF_3$ and simply reduces the particle size. Figure 6-2d exhibits the crystal structure of the orthorhombic $NaFeF_3$, in which the structure is characterized by corner-sharing among each FeF_6 octahedron unit with Na^+ occupying the large spaces in the center coordinated by eight octahedron units. This structure creates paths for Na^+ diffusion along the [010] channels and in the [101] and [−101] diagonals of the *ac*-plane [18, 31, 32]. Particle size and morphology of H-$NaFeF_3$ were confirmed by SEM observation. As shown in Figure 6-2e, H-$NaFeF_3$ has clear crystal faces with particle sizes between 200 nm to 1 μm. The SEM images of the $NaFeF_3$@C reveal that particle size is reduced to about 100 nm or less due to the break of the particles by ball-milling (Figure 6-2f). Elemental mapping by EDX employed during the SEM operation designated that Na, Fe, F and C are homogeneously distributed within the $NaFeF_3$@C particle (Figure 6-2f).

The galvanostatic charge-discharge tests were performed in a Na/$NaFeF_3$@C half-cell configuration with a Na metal counter electrode and the Na[FSA]-[C_2C_1im][FSA] (20:80 in mol) IL electrolyte. The charge-discharge curves of the initial two cycles, the corresponding dQ/dV plots, and the GITT curves during the first two cycles (voltage

range of 2.2−4.1 V) are shown in Figure 6-3. The first two cycles of $NaFeF_3$@C measured at a rate of 10 mA g^{-1} at 90 °C deliver a discharge capacity of 177 mAh g^{-1}, corresponding to the 0.9 Na^+ extraction/insertion based on the theoretical capacity of 197 mAh g^{-1} (Figure 6-3a-I). These first two charge-discharge curves are characterized by two pairs of distinct plateaus around 3.0 V and 3.2 V, respectively. The corresponding dQ/dV plots shown in Figure 6-3a-II provide specific voltage values for two plateaus, where two pairs of redox peaks at 3.04/2.97 V and 3.36/3.12 V are observed. A peak around 4.0 V observed at the end of the first charge is due to the decomposition of the electrolyte at the high voltage [33, 34]. Results of the GITT test with a stepwise polarization at 10 mA g^{-1} for 1 h followed by monitoring the open-circuit voltage for 12 h are shown in Figure 6-3a-III. The potential after relaxation gradually increases and then remains virtually unchanged with small overvoltage during the initial charge process, representing a plateau around 3.1 V. A two-phase coexistence reaction is suggested in this stage. As the voltage keeps rising, the other plateau in which the open circuit voltage is relatively constant is also observed around 3.4 V. The open circuit voltage above 3.4 V shows a sloping shape, suggesting that a single-phase reaction occurs in this region. Although the difference in voltage is less distinct, the discharge process also has two plateaus (3.2 and 3.0 V) with a larger solid-solution region at the lower voltage (< 3.0 V).

The electrochemical properties of $NaFeF_3$@C were also measured at 25 °C to discern the effects of temperature on electrode behavior (Figure 6-3b). The galvanostatic

charge-discharge tests in the same voltage range were performed by employing a Na/$NaFeF_3$@C cell with a Na[FSA]-[C_2C_1im][FSA] IL electrolyte (Figure 6-3b-I). The first two cycles measured at 25 °C show a limited discharge capacity of 99.5 mAh g^{-1} at a current density of 10 mA g^{-1} with two pairs of small plateaus between the voltage range of 2.2−4.1 V. Two pairs of broad peaks shown in the dQ/dV plots (Figure 6-3b-II) offer the specific voltages, where the plateau at the higher voltage during discharge is ambiguous. The GITT test conducted at 25 °C under the same conditions as those at 90 °C are shown in Figure 6-3b-III and the first two cycles do not show distinct plateaus. All these results demonstrate the limited activity of $NaFeF_3$@C at 25 °C and the absence of two-phase reaction. In order to elucidate the reasons for the increase in capacity caused by the elevation of operating temperature, the EIS measurement was carried out by employing a $NaFeF_3$@C/$NaFeF_3$@C symmetric cell at 25 and 90 °C, respectively (Figure 6-4a). The two electrodes used in this symmetric cell was obtained by charging the Na/$NaFeF_3$@C half cells to SOC = 50% at 25 and 90 °C, respectively. The Nyquist plots consist of two semicircles and were fitted by using the equivalent circuit shown in the inset of Figure 6-4b). As a result of fitting (Table 6-2), all resistances decrease as the temperature increases from 25 °C to 90 °C, which indicates the higher ion diffusion, thereby resulting in an increase in the activity of $NaFeF_3$@C at an elevated temperature [28, 35-40]. In more details, the decrease in bulk resistance (R_{bulk}) indicates the higher ionic conductivity of electrolyte at 90 °C [22, 25, 29, 37]. The resistance corresponding

to the semicircle at the higher frequency region (R_1) decreases slightly as the temperature increased from 25 to 90 °C, resulting in the fast migration of Na^+ ions through the CEI layer [41-43]. An increase in temperature also leads to an obvious reduction of the resistance in the lower frequency region (R_2), which provides evidence for the improvement of the interfacial phenomena at 90 °C [39, 40, 43, 44]. The EIS data indicate that the interfacial resistance is the dominant factor to determine the limited capacity at 25 °C.

The phase transformation and reaction mechanisms of the orthorhombic $NaFeF_3$ are verified through synchrotron XRD measurement (Figure 6-5a) combined with Rietveld refinement (see Figure 6-6 for the refinement results and Table 6-3 for the refined parameters). The test electrodes at different SOCs were obtained in a Na/$NaFeF_3$@C half-cell at 90 °C in the potential-time profile (Figure 6-5b). All the XRD patterns contain a peak assigned to PTFE binder at $2\theta = 10.36°$ [45]. Rietveld refinement confirms that the diffraction peaks of the pristine $NaFeF_3$@C electrode (Pattern 1) are indexed as orthorhombic $NaFeF_3$ (Figure 6-6a) with almost the same lattice parameters as those of H-$NaFeF_3$ and $NaFeF_3$@C (Figure 6-2a,b and Table 6-1). After the half-charge to 3.2 V (Pattern 2), the diffraction peaks become broader compared to Pattern 1. The results of Rietveld refinement confirm the obtained XRD diffraction peaks can be indexed as an orthorhombic phase with a Na occupancy of 0.5 (Figure 6-6b) with an impurity phase of the unreacted $NaFeF_3$. Formation of $Na_{0.5}FeF_3$ agrees with the previous

theoretical works [16, 17]. After full-charge to 4.1 V (Pattern 3), all diffraction peaks shift to the higher angles, indicating that a new phase appears in the state of the full desodiation. The Rietveld refinement confirms that the new phase is indexed to the cubic FeF_3 with the lattice parameter of a = 3.8561(7) Å (Figure 6-6c). Although the phase transformation from orthorhombic $NaFeF_3$ to cubic FeF_3 during desodiation was reported for nano-sized orthorhombic $NaFeF_3$ [18], orthorhombic $Na_{0.5}FeF_3$ as an intermediate phase is experimentally confirmed in this work operating at 90 °C for the first time. Pattern 4 is the XRD pattern of the discharged electrode to 3.1 V, in which the diffraction peaks shift to the lower angle than those in Pattern 3. The fitting results shown in Figure 6-6d indicate that the phase transformation from cubic FeF_3 back to orthorhombic $Na_{0.5}FeF_3$ after discharging to 3.1 V. However, the orthorhombic $Na_{0.5}FeF_3$ obtained during sodiation possess of cubic FeF_3 shows smaller lattice parameters than those formed during the initial desodiation. The recovery of orthorhombic $NaFeF_3$ is confirmed by the diffraction peaks which shift back to their original positions at 2.2 V (Pattern 5). The fitting results obtained by Rietveld refinement identify the recovered orthorhombic $NaFeF_3$ phase show the lattice parameters of a = 5.6551(3) Å, b = 7.8806(5) Å, and c = 5.4849(3) Å (Figure 6-6e) which are close to those of the pristine $NaFeF_3$, suggesting the good reversibility of the phase transformation from orthorhombic $NaFeF_3$ to cubic FeF_3 during the desodiation and sodiation processes although two orthorhombic $Na_{0.5}FeF_3$ with different lattice parameters are formed as intermediate phase.

The cycle performance of the Na/$NaFeF_3$@C half-cell was investigated by continuous charging and discharging tests at a rate of 100 mA g^{-1} in the voltage range of 2.2–4.0 V. The obtained data is shown in Figure 6-7a in the form of the discharge capacity and coulombic efficiency as a function of cycle number. As shown in Figure 6-7a, the $NaFeF_3$@C electrode exhibits an initial discharge capacity of 152 mAh g^{-1} and a long-term stability up to 400 cycles. During cycling, the discharge capacity gradually decreases with the capacity retention of 82, 75, 64, 56, and 50% at the 50, 100, 200, 300 and 400th cycles, respectively. The corresponding charge-discharge curves, and their dQ/dV plots are shown in Figure 6-7b,c. The charge-discharge curve with two plateaus (Figure 6-7b) is preserved, although the voltages of oxidation and reduction peaks increase and decrease during cycling (Figure 6-7c). These results indicate that the multi-phase transition as observed above is maintained during cycling, but polarization gradually increases, which is presumably due to the large volume change (volume ratio: orthorhombic $NaFeF_3$ / cubic FeF_3 = 1.00 / 0.94) caused by the phase transformation between the orthorhombic $NaFeF_3$ and cubic FeF_3 during the charge and discharge process. In order to further explore the causes behind the capacity decay during cycling, EIS measurements were conducted on the Na/$NaFeF_3$@C half-cell during cycling in the IL electrolyte at 90 °C. In order to quantify the impedance contributions of each circuit element, the Nyquist plots at the 1st and 100th cycles are compared in Figure 6-7d and fitted with an equivalent circuit provided in Figure 6-7e. From the fitting results shown in Figure 6-7f and Table 6-4, all

the resistances are small after the 1st charge-discharge cycle and increase after the 100th cycle, which indicates the degradation of Na^+ kinetics in the cell. In particular, R_2 shows a significant increase relative to the increase of R_{bulk} and R_1, which suggests that the interfacial phenomenon restricts the cycle performance [39, 40]. The influence of a half-cell configuration in which the behavior of Na metal counter electrode affects the impedance spectroscopy is not likely conceivable because of the stable deposition-dissolution behavior of Na metal at 90 °C [22].

6.4 Conclusions

In this study, orthorhombic $NaFeF_3$ was prepared by high-energy ball milling combined with heat treatment. Its electrochemical properties and mechanisms were investigated at 90 °C with the aid of the thermally stable Na[FSA]-[C_2C_1im][FSA] IL electrolyte. The $NaFeF_3$@C electrode showed a reversible capacity of 177 mAh g^{-1} at a rate of 10 mA g^{-1} in a cutoff voltage of 2.2−4.1 V, along with two pair of plateaus. Orthorhombic $NaFeF_3$ exhibits a long-term cycle stability at a current density of 100 mA g^{-1}. Combination of the GITT tests and synchrotron XRD analyses revealed that the two pair of plateaus in charge-discharge curves correspond to multi-phase reaction between orthorhombic $NaFeF_3$ and cubic FeF_3 through the intermediate orthorhombic $Na_{0.5}FeF_3$ phase.

The Na-Fe-F system is tremendously important to design high energy density SIBs. This study explored the reaction mechanisms of orthorhombic $NaFeF_3$ in details

and provided insights for understating this system. The high electrochemical activity at elevated temperatures and long-term cycling stability bring promises for the practical application of composite $NaFeF_3$ in large-scale instruments. However, its performance still has space for improvement by enhancing the reversibility of the multi-phase transformation during sodiation and desodiation. Moreover, this work introduces the intermediate phase, orthorhombic $Na_{0.5}FeF_3$, on the basis of experimental data for the first time, but Na^+ extraction/insertion path from/into orthorhombic $NaFeF_3$/cubic FeF_3 is still uncertain. Although orthorhombic $NaFeF_3$ is recovered at the end of sodiation in one cycle, the formation processes of two orthorhombic $Na_{0.5}FeF_3$ with different lattice parameters are worth exploring for a deeper understanding on the Na-Fe-F system and better electrochemical performance.

Table 6-1 Crystallographic parameters of the orthorhombic $NaFeF_3$ phase obtained by Rietveld refinement.

Refinement results for the H-$NaFeF_3$ in Figure 6-2a (S.G. *Pnma*) R_p = 1.33%, R_{wp} = 1.82%						
a = 5.6577(2) Å		*b* = 7.8860(2) Å		*c* = 5.4937(2) Å	*V* = 245.11(2) Å^3	
Atom	Wyckoff symbol	*x*	*y*	*z*	*B*iso / Å^2	Occup.
Fe	4*a*	0	0	0	0.5	1
Na	4*c*	0.4483(7)	0.25	0.013(1)	0.5	1
F1	4*c*	0.548(1)	0.25	0.6085(9)	0.5	1
F2	8*d*	0.1978(7)	0.0628(5)	0.3068(9)	0.5	1
Refinement results for the $NaFeF_3$@C in Figure 6-2b (S.G. *Pnma*) R_p = 1.16%, R_{wp} = 1.49%						
a = 5.665(3) Å		*b* = 7.877(5) Å		*c* = 5.485(3) Å	*V* = 244.8(4) Å^3	
Atom	Wyckoff symbol	*x*	*y*	*z*	*B*iso / Å^2	Occup.
Fe	4*a*	0	0	0	0.5	1
Na	4*c*	0.449(1)	0.25	0.010(3)	0.5	1
F1	4*c*	0.538(3)	0.25	0.650(2)	0.5	1
F2	8*d*	0.202(2)	0.051(1)	0.301(2)	0.5	1

Table 6-2 EIS fitting parameters for the Nyquist plots of the $NaFeF_3$@C/$NaFeF_3$@C symmetric cells at 25 and 90 °C as shown in Figure 6-4.

T / °C	Resistance / Ω			CPE* × 10^{-5} / F $s^{(a-1)}$			
	R_{bulk}	R_1	R_2	CPE_1	a	CPE_2	a
25	6.9	7.0	67.5	9.0	0.61	1.6	0.82
90	4.7	5.2	32.1	0.8	1.00	8.9	0.70

*CPE: constant phase element.

Table 6-3 Crystallographic parameters of the phases appearing during charge-discharge of orthorhombic $NaFeF_3$ (Patterns 1, 2, 3, 4, and 5 in Figure 6-5a) by Rietveld refinement.

Refinement results for the orthorhombic $NaFeF_3$ phase in Pattern 1[a] (S.G. *Pnma*)
R_p = 1.67%, R_{wp} = 2.00%

a = 5.6553(5) Å		*b* = 7.8858(7) Å		*c* = 5.4826(4) Å	*V* = 244.50(4) Å^3	
Atom	Wyckoff symbol	*x*	*y*	*z*	*B*iso / Å^2	Occup.
Fe	4*a*	0	0	0	0.5	1
Na	4*c*	0.4448(3)	0.25	0.0117(9)	0.5	1
F1	4*c*	0.5675(8)	0.25	0.6018(8)	0.5	1
F2	8*d*	0.1919(6)	0.0575(4)	0.3011(6)	0.5	1

Refinement results for the orthorhombic $Na_{0.5}FeF_3$ phase in Pattern 2[b] (S.G. *Pnma*)
R_p = 2.79%, R_{wp} = 3.87%

a = 5.669(1) Å		*b* = 7.876(2) Å		*c* = 5.488(1) Å	*V* = 245.03(9) Å^3	
Atom	Wyckoff symbol	*x*	*y*	*z*	*B*iso / Å^2	Occup.
Fe	4*a*	0	0	0	0.5	1
Na	4*c*	0.461(3)	0.25	0.028(4)	0.5	0.5
F1	4*c*	0.501(4)	0.25	0.568(2)	0.5	1
F2	8*d*	0.197(1)	0.101(1)	0.307(2)	0.5	1

Refinement results for the cubic FeF_3 phase in Pattern 3[c] (S.G. $Pm\bar{3}m$)
R_p = 7.88%, R_{wp} = 10.29%

a = 3.8561(7) Å				*V* = 57.34(3) Å^3		
Atom	Wyckoff symbol	*x*	*y*	*z*	*B*iso / Å^2	Occup.
Fe	1*a*	0	0	0	0.5	1
F	3*d*	0	0	0.5	0.5	1

Refinement results for the orthorhombic $Na_{0.5}FeF_3$ phase in Pattern 4[d] (S.G. *Pnma*)
R_p = 2.78%, R_{wp} = 3.82%

a = 5.5537(7) Å		*b* = 7.7910(9) Å		*c* = 5.4362(7) Å	*V* = 235.22(5) Å^3	
Atom	Wyckoff symbol	*x*	*y*	*z*	*B*iso / Å^2	Occup.
Fe	4*a*	0	0	0	0.5	1
Na	4*c*	0.462(1)	0.25	-0.015(3)	0.5	0.5
F1	4*c*	0.534(2)	0.25	0.572(1)	0.5	1
F2	8*d*	0.1981(8)	0.0512(7)	0.2889(9)	0.5	1

Refinement results for the orthorhombic $NaFeF_3$ phase in Pattern 5[e] (S.G. *Pnma*)
R_p = 2.79%, R_{wp} = 3.51%

a = 5.6551(3) Å		*b* = 7.8806(5) Å		*c* = 5.4849(3) Å	*V* = 244.44(3) Å^3	
Atom	Wyckoff symbol	*x*	*y*	*z*	*B*iso / Å^2	Occup.
Fe	4*a*	0	0	0	0.5	1
Na	4*c*	0.4464(3)	0.25	0.0158(6)	0.5	1
F1	4*c*	0.5495(6)	0.25	0.5998(6)	0.5	1
F2	8*d*	0.1972(4)	0.0582(3)	0.3027(4)	0.5	1

[a]There is no impurity phase. [b]The orthorhombic $NaFeF_3$ phase is considered to be impurity phase (28 wt%). [c] There is no impurity phase. [d]There is no impurity phase. [e]There is no impurity phase.

Table 6-4 EIS fitting parameters for Nyquist plots of Na/Na[FSA]-[C_2C_1im][FSA]/$NaFeF_3$@C half-cell shown in Figure 6-7d-f.

Cycle number	Resistance / Ω			CPE × 10^{-5} / F $s^{(a-1)}$			
	R_{bulk}	R_1	R_2	CPE_1	a	CPE_2	a
1st	2.62	5.33	33.45	0.16	1	8.22	0.71
100th	12.57	23.82	339.2	0.29	0.87	2.53	0.77

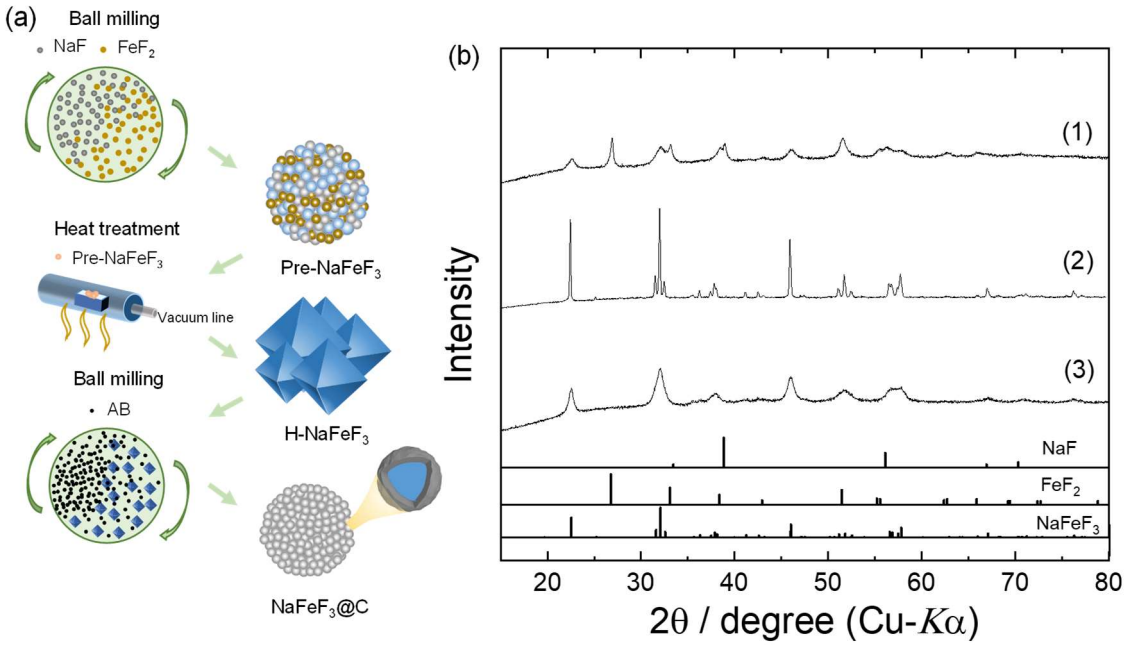

Figure 6-1 (a) Schematic illustration on the preparation of orthorhombic $NaFeF_3$. Step 1: ball-milling of NaF and FeF_2 (Pre-$NaFeF_3$). Step 2: heat treatment of Pre-$NaFeF_3$ at 600 °C under vacuum (H-$NaFeF_3$). Step 3: ball-milling of H-$NaFeF_3$ and AB ($NaFeF_3$-@C). (b) The corresponding XRD patterns of (1) Pre-$NaFeF_3$, (2) H-$NaFeF_3$ and (3) $NaFeF_3$@C.

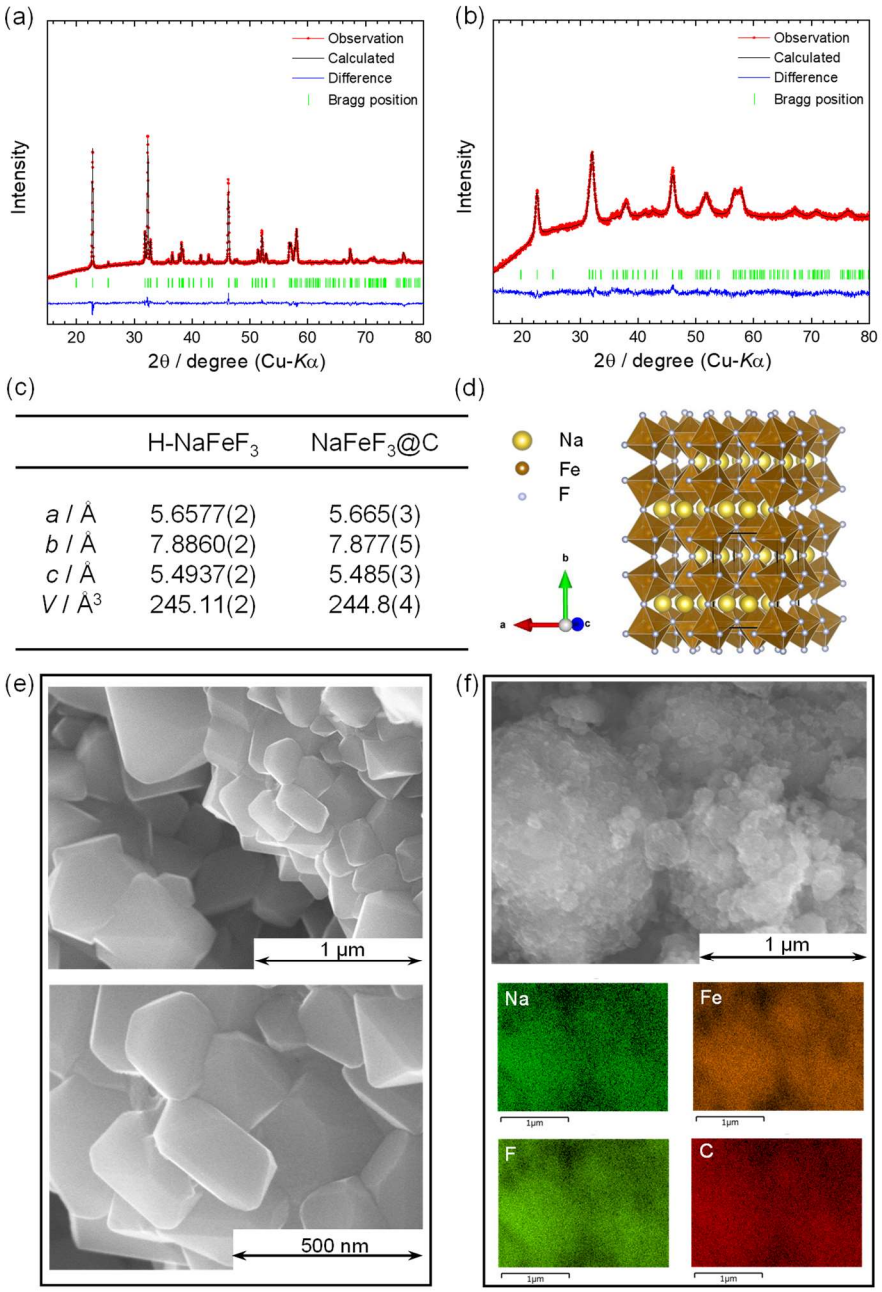

	H-$NaFeF_3$	$NaFeF_3$@C
a / Å	5.6577(2)	5.665(3)
b / Å	7.8860(2)	7.877(5)
c / Å	5.4937(2)	5.485(3)
V / Å^3	245.11(2)	244.8(4)

Figure 6-2 (a) XRD pattern and Rietveld refinement result of H-$NaFeF_3$ (see Figure 6-1b as well). (b) XRD pattern and Rietveld refinement result of $NaFeF_3$@C (see Figure 6-1c as well). (c) The lattice parameters of H-$NaFeF_3$ and $NaFeF_3$@C determined by Rietveld refinement (see Table 6-1 for the crystallographic data). (d) The refined crystal structure of orthorhombic $NaFeF_3$ (black lines indicate the unit cell). (e) The corresponding SEM morphology for H-$NaFeF_3$. Bottom image is the magnification of the top one. (f) The corresponding morphology and EDX mappings of Na, Fe, F, and C for $NaFeF_3$@C.

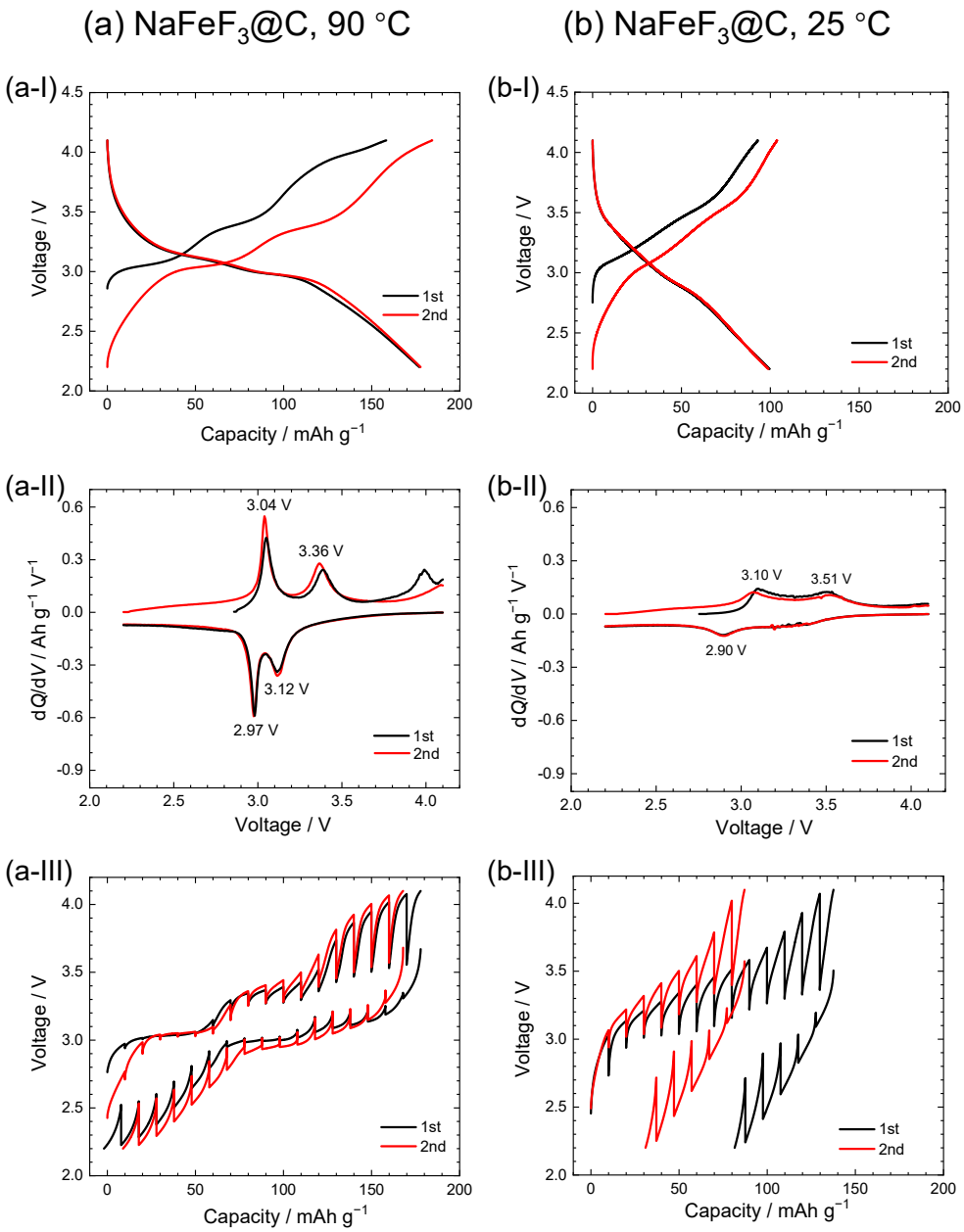

Figure 6-3 Electrochemical data of (a) $NaFeF_3$@C at 90 °C, and (b) $NaFeF_3$@C at 25 °C using the Na[FSA]-[C_2C_1im][FSA] (20:80 in mol) IL electrolyte in the voltage range of 2.2−4.1 V. (I) Charge-discharge curves of the initial two cycles at 10 mA g^{-1}, (II) the corresponding dQ/dV plots of the charge-discharge curves in (I), and (III) the GITT curves conducted via a stepwise polarization at 10 mA g^{-1} for 1 h followed by monitoring the open-circuit voltage for 12 h.

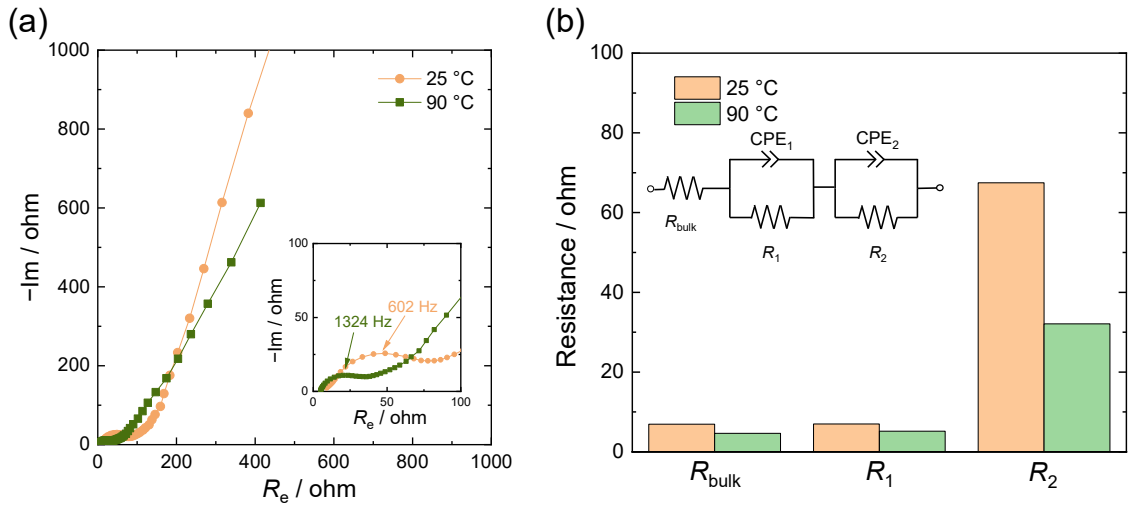

Figure 6-4 (a) Nyquist plots for the $NaFeF_3$@C/$NaFeF_3$@C symmetric cell using the Na[FSA]-[C_2C_1im][FSA] (20:80 in mol) IL electrolyte at 25 and 90 °C. AC perturbation: 10 mV. Frequency range: 10 mHz–100 kHz. Inset is the magnification of the top one. (b) R_{bulk}, R_1, and R_2 obtained from EIS fitted plots. Inset is an equivalent circuit to fit the Nyquist plots in (a), where R_{bulk} denotes the bulk resistance in the high frequency. R_1 and R_2 represent the corresponding respective resistance of two semicircles in the high and low frequency ranges, corresponding to Na^+ diffusion within the cathode-electrolyte interface layer (CEI) and the interfacial resistance, respectively. The symbol CPE denotes the constant phase element. See Table 6-2 for the fitting parameters of the impedance spectra.

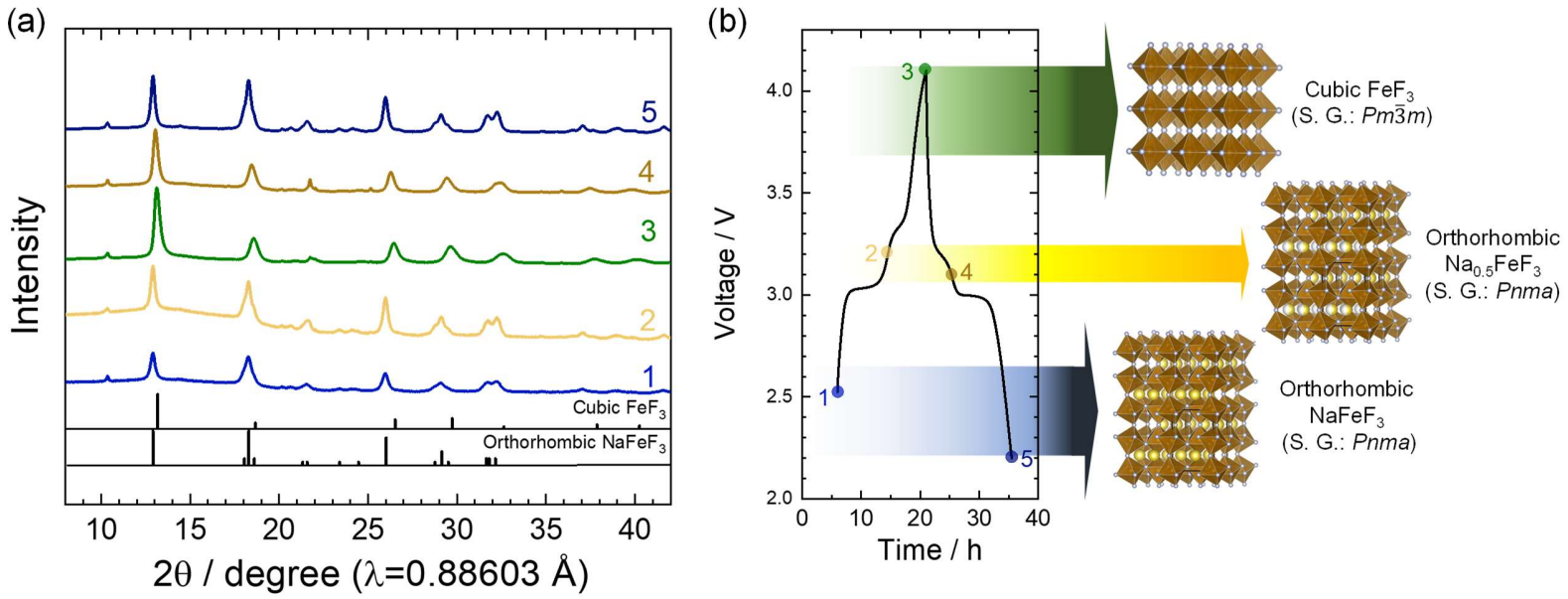

Figure 6-5 (a) Synchrotron XRD patterns (λ = 0.88603 Å) of the charged and discharged samples for the $NaFeF_3$@C electrode and (b) the corresponding initial charge and discharge voltage profiles at a current density of 10 mA g^{-1} in the Na[FSA]-[C_2C_1im][FSA] (20:80 in mol) IL electrolyte at 90 °C: (1) Pristine, (2) charged to 3.2 V, (3) charged to 4.1 V, (4) discharged to 3.1 V, and (5) discharged to 2.2 V.

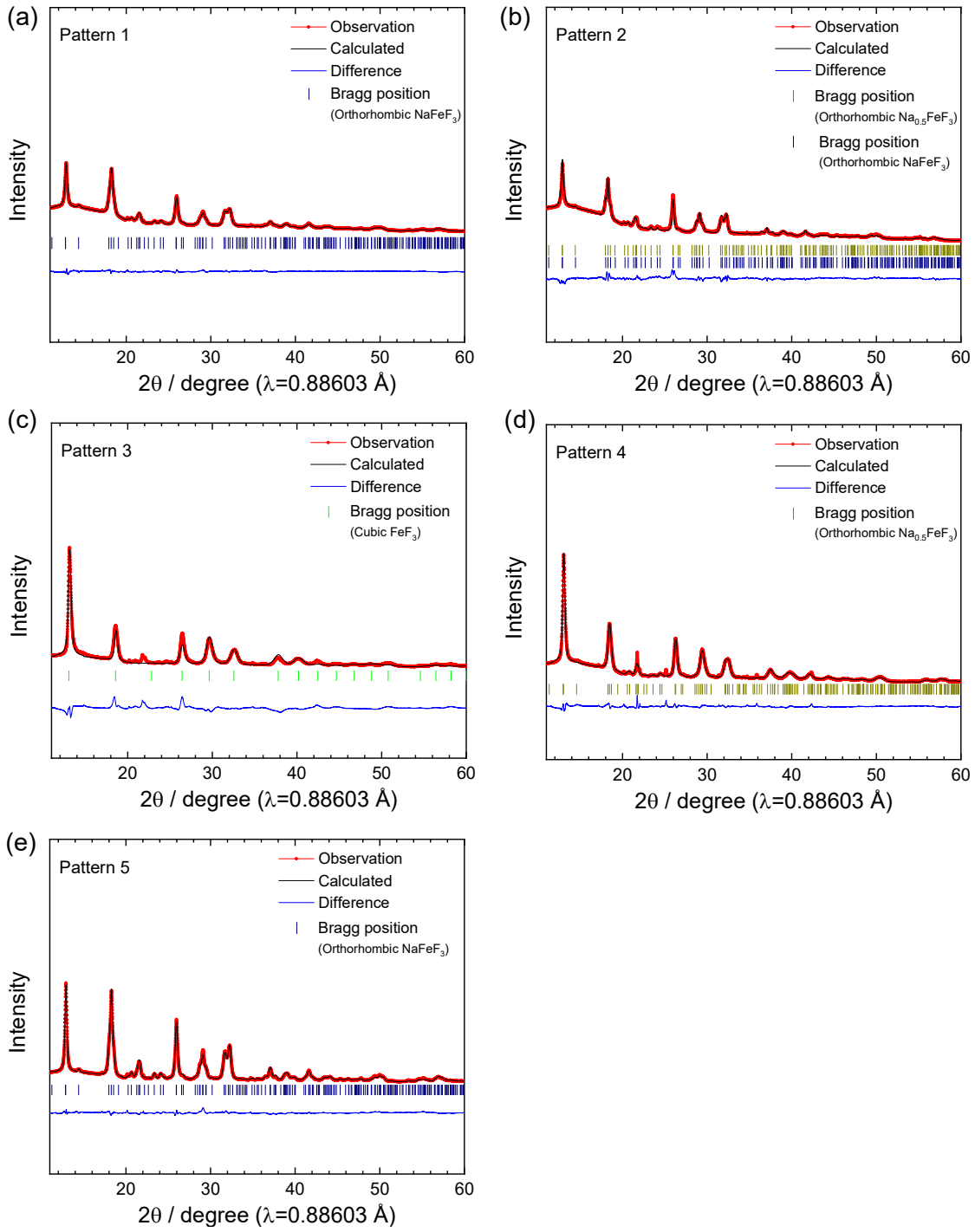

Figure 6-6 Synchrotron XRD patterns and the results of Rietveld refinement for the $NaFeF_3$@C electrodes at different charging and discharging states. (a) Pattern 1, (b) Pattern 2, (c) Pattern 3, (d) Pattern 4, and (e) Pattern 5 corresponding to Figure 6-5a. See Table 6-3 for detailed parameters.

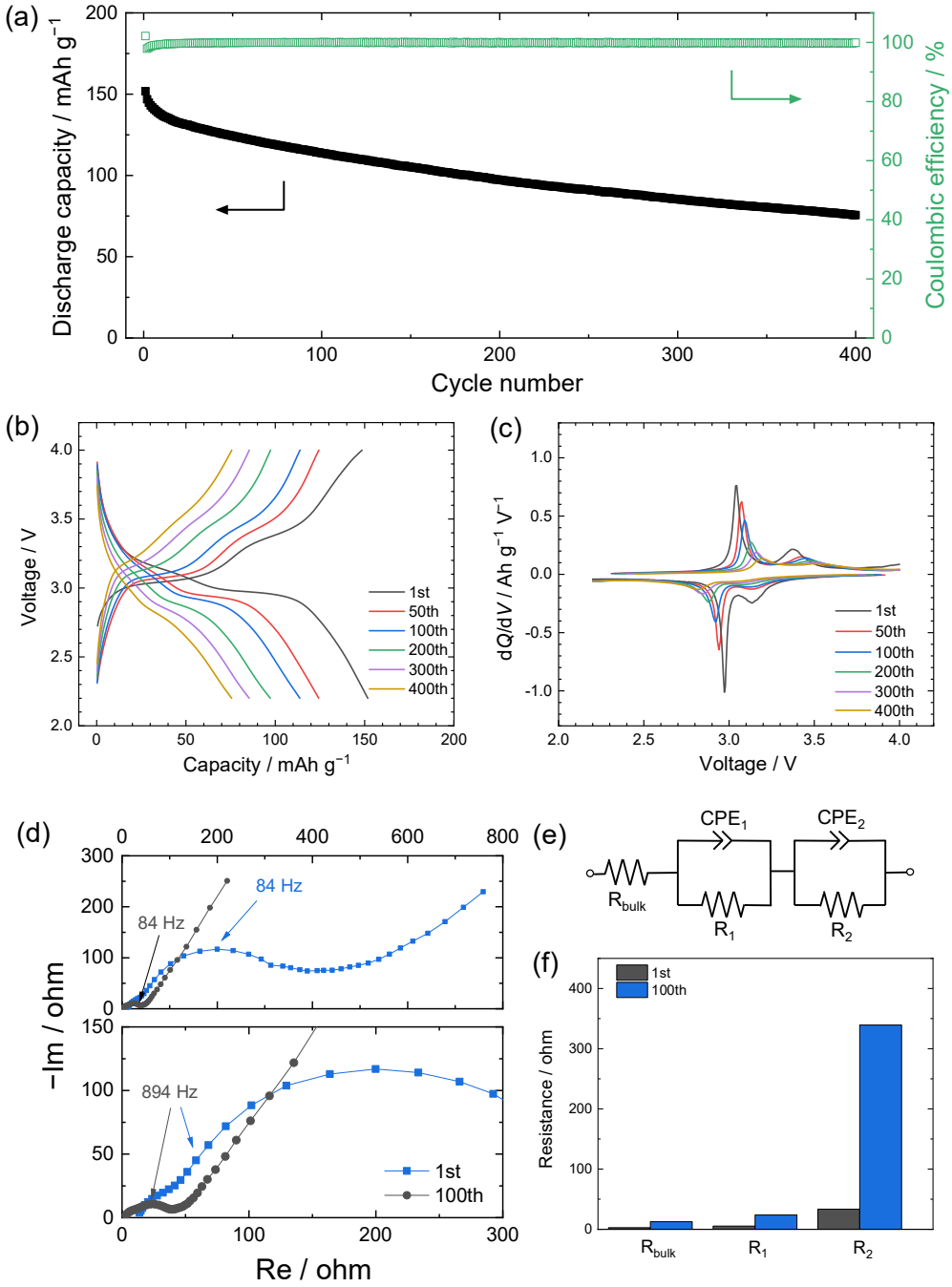

Figure 6-7 The electrochemical properties of the $NaFeF_3$@C electrode in the voltage range of 2.2−4.0 V using the Na[FSA]-[C_2C_1im][FSA] (20:80 in mol) IL electrolyte at 90 °C. (a) The corresponding cycling performance during 400 cycles. (b) The charge-discharge curves at the 1st, 100th, 200th, and 400th at a rate of 100 mA g^{-1}. (c) the corresponding dQ/dV plots of the charge-discharge curves in (b). (d) Nyquist plots for the Na/$NaFeF_3$ half-cell after the 1st and 100th cycles. AC perturbation: 10 mV. Frequency range: 10 mHz–100 kHz. The bottom plot is the magnification of the top one. (e) The equivalent circuit used for the fitting of the Nyquist plots in (d). (f) R_{bulk}, R_1, and R_2 obtained by fitting the Nyquist plots in (d) (see Table 6-4 for the fitting parameters).

References

[1] R.E. Doe, K.A. Persson, Y.S. Meng, G. Ceder, Chem. Mater., 20 (2008) 5274–5283.

[2] N. Yamakawa, M. Jiang, B. Key, C.P. Grey, J. Am. Chem. Soc., 131 (2009) 10525−10536.

[3] L. Li, R. Jacobs, P. Gao, L. Gan, F. Wang, D. Morgan, S. Jin, J. Am. Chem. Soc., 138 (2016) 2838–2848.

[4] S. Tawa, Y. Sato, Y. Orikasa, K. Matsumoto, R. Hagiwara, J. Power Sources, 412 (2019) 180–188.

[5] A.W. Xiao, H.J. Lee, I. Capone, A. Robertson, T.U. Wi, J. Fawdon, S. Wheeler, H.W. Lee, N. Grobert, M. Pasta, Nature Mater., 19 (2020) 644–654.

[6] M. Nishijima, I.D. Gocheva, S. Okada, T. Doi, J.-i. Yamaki, T. Nishida, J. Power Sources, 190 (2009) 558–562.

[7] C. Li, C. Yin, L. Gu, R.E. Dinnebier, X. Mu, P.A. van Aken, J. Maier, J. Am. Chem. Soc., 135 (2013) 11425−11428.

[8] C. Li, C. Yin, X. Mu, J. Maier, Chem. Mater., 25 (2013) 962–969.

[9] L. Liu, H. Guo, M. Zhou, Q. Wei, Z. Yang, H. Shu, X. Yang, J. Tan, Z. Yan, X. Wang, Journal of Power Sources, 238 (2013) 501–515.

[10] Y. Shen, X. Wang, H. Hu, M. Jiang, X. Yang, H. Shu, J. Power Sources, 283 (2015) 204−210.

[11] S. Wei, X. Wang, M. Jiang, R. Zhang, Y. Shen, H. Hu, J. Alloys Compd., 689 (2016) 945−951.

[12] C.P. Guntlin, T. Zünd, K.V. Kravchyk, M. Wörle, M.I. Bodnarchuk, M.V. Kovalenko, J. Mater. Chem. A, 5 (2017) 7383−7393.

[13] R. Zhang, X. Wang, X. Wang, M. Liu, S. Wei, Y. Wang, H. Hu, J. Electrochem. Soc., 165 (2018) A89−A96.

[14] M. Liu, L. Liu, M. Li, B. Chen, H. Lei, H. Hu, X. Wang, J. Alloys Compd., 829 (2020) 1−10.

[15] Z. Sun, W. Fu, M.Z. Liu, P. Lu, E. Zhao, A. Magasinski, M. Liu, S. Luo, J. McDaniel, G. Yushin, J. Mater. Chem. A, 8 (2020) 4091−4098.

[16] S. Yu, P. Zhang, S.Q. Wu, A.Y. Li, Z.Z. Zhu, Y. Yang, J. Solid State Electrochem., 18 (2014) 2071–2075.

[17] A. Kitajou, Y. Ishado, T. Yamashita, H. Momida, T. Oguchi, S. Okada, Electrochim. Acta, 245 (2017) 424–429.

[18] A. Martin, M.-L. Doublet, E. Kemnitz, N. Pinna, Adv. Funct. Mater., 28 (2018) 1802057.

[19] D.-l. Ma, H.-g. Wang, Y. Li, D. Xu, S. Yuan, X.-l. Huang, X.-b. Zhang, Y. Zhang, Nano Energy, 10 (2014) 295–304.

[20] T. Torimoto, T. Tsuda, K. Okazaki, S. Kuwabata, Adv. Mater., 22 (2010) 1196−1221.

[21] D.R. MacFarlane, N. Tachikawa, M. Forsyth, J.M. Pringle, P.C. Howlett, G.D. Elliott, J.H. Davis, M. Watanabe, P. Simon, C.A. Angell, Energy Environ. Sci., 7 (2014) 232−250.

[22] K. Matsumoto, T. Hosokawa, T. Nohira, R. Hagiwara, A. Fukunaga, K. Numata, E. Itani, S. Sakai, K. Nitta, S. Inazawa, J. Power Sources, 265 (2014) 36–39.

[23] K. Matsumoto, Y. Okamoto, T. Nohira, R. Hagiwara, J. Phys. Chem. C, 119 (2015) 7648–7655.

[24] J. Hwang, K. Matsumoto, R. Hagiwara, Adv. Sustainable Syst., 2 (2018) 1700171.

[25] J. Hwang, K. Matsumoto, R. Hagiwara, J. Phys. Chem. C 122 (2018) 26857−26864.

[26] R. Hagiwara, K. Matsumoto, J. Hwang, T. Nohira, Chem. Rec., 19 (2018) 758–770.

[27] K. Matsumoto, J. Hwang, S. Kaushik, C.-Y. Chen, R. Hagiwara, Energy Environ. Sci., 12 (2019) 3247–3287.

[28] J. Hwang, K. Matsumoto, R. Hagiwara, Adv. Energy Mater. , 10 (2020) 2001880.

[29] B.H. Toby, J. Appl. Cryst., 34 (2001) 210−213.

[30] K. Momma, F. Izumi, J. Appl. Cryst. , 44 (2011) 1272−1276.

[31] A. Martin, E.S. Santiago, E. Kemnitz, N. Pinna, ACS Appl. Mater. Interfaces, 11 (2019) 33132−33139.

[32] F.L.M. Bernal, B. Gonano, F. Lundvall, D.S. Wragg, H. Fjellvåg, Phys. Rev. Materials 4(2020) 1−9.

[33] Y. Jin, Y. Xu, P.M.L. Le, T.D. Vo, Q. Zhou, X. Qi, M.H. Engelhard, B.E. Matthews, H. Jia, Z. Nie, C. Niu, C. Wang, Y. Hu, H. Pan, J.-G. Zhang, ACS Energy Lett. , 5 (2020) 3212−3220.

[34] I. Moeez, D. Susanto, W. Chang, H.-D. Lim, K.Y. Chung, Chem. Eng. J., 425 (2021) 130547.

[35] M.D. Levi, D. Aurbach, J. Phys. Chem. B, 101 (1997) 4630−4640.

[36] Y.-L. Shi, M.-F. Shen, S.-D. Xu, X.-Y. Qiu, L. Jiang, Y.-H. Qiang, Q.-C. Zhuang, S.-G. Sun, Int. J. Electrochem. Sci., 6 (2011) 3399−3415.

[37] F. Wohde, M. Balabajew, B. Roling, J. Electrochem. Soc., 163 (2016) A714−A721.

[38] W. Zhang, F.H. Richter, S.P. Culver, T. Leichtweiss, J.G. Lozano, C. Dietrich, P.G. Bruce, W.G. Zeier, J. Janek, ACS Appl. Mater. Interfaces, 10 (2018) 22226−22236.

[39] A.R.C. Bredar, A.L. Chown, A.R. Burton, B.H. Farnum, ACS Appl. Energy Mater. , 3 (2020) 66−98.

[40] Y. Charles-Blin, K. Nemoto, N. Zettsu, K. Teshima, J. Mater. Chem. A, 8 (2020) 20979−20986.

[41] C.H. Chen, J. Liu, K. Amine, J. Power Sources, 96 (2001) 321−328.

[42] D. Andre, M. Meiler, K. Steiner, C. Wimmer, T. Soczka-Guth, D.U. Sauer, J. Power Sources, 196 (2011) 5334−5341.

[43] W. Choi, H.-C. Shin, J.M. Kim, J.-Y. Choi, W.-S. Yoon, J. Electrochem. Sci. Technol., 11 (2020) 1−13.

[44] D. Qu, G. Wang, J. Kafle, J. Harris, L. Crain, Z. Jin, D. Zheng, Small Methods, 2 (2018) 1−27.

[45] M. Kim, S. Lee, B. Kang, Adv. Sci., 3 (2016) 1500366.

Chapter 7

General Conclusions

Among the secondary batteries, LIBs have been considered to be the most promising batteries due to their excellent lifetime and energy/power densities. SIBs, as the most potent alternatives to LIBs in large-scale energy storage applications, have also received widespread attention. For the future application of LIBs and SIBs, it is necessary to consolidate the two major requirements of high performance and safe operation simultaneously. The introduction of ILs as electrolytes enables the batteries to operate safely and achieve high-power applications with their low flammability, volatility, and high ionic conductivity. Iron fluorides, which is a kind of material characterized by low toxicity, abundant iron resources, high redox potential, and large theoretical capacity, are expected to be promising candidates of the positive electrodes for cost-effective and high-energy-density applications. However, the inadequate understanding of their electrochemical capabilities and limitations have hindered their application as energy-dense positive electrode materials for batteries. From this point of view, this thesis described the comprehensive electrochemical behavior of several iron fluoride-based materials in IL electrolytes for a better understanding of the reaction mechanism in the Li-Fe-F and Na-Fe-F systems.

In Chapter 3, the ordered trirutile $LiFe_2F_6$ was prepared for the first time by high-energy ball milling combined with heat treatment as a positive electrode material for LIBs.

Its improved electrochemical behavior was realized by introducing the elevated temperature of 90 °C with the aid of Li[FSA]-[C_2C_1im][FSA] IL (30:70 in molar ratio). Synchrotron XRD and XAFS data revealed that a reversible topotactic Li^+ extraction/insertion from/into the trirutile structure occurs through a two-phase reaction with a subtle volume change (1.09% between $LiFe_2F_6$ and $Li_{0.22}Fe_2F_6$) in the voltage range of 3.2−4.3 V. The extension of lower cut-off voltage from 3.2 to 2.5 V led a conversion reaction from the trirutile $LiFe_2F_6$ to LiF and rutile FeF_2 during discharging. The subsequent charge triggerred the formation of the Li/Fe disordered trirutile structure at 4.3 V without showing the reconversion from LiF and rutile FeF_2 to the ordered trirutile $LiFe_2F_6$ or FeF_3.

In Chapter 4, a carbon-coated $Li_{1.2}MnFe_{1.2}F_{6.8}$ with a cation-disordered rutile structure was presented for the first time as a positive electrode material for LIBs. The composite electrode was investigated at 90 °C using a thermally stable IL electrolyte to withdraw electrochemical activity. The synchrotron XRD and XPS techniques were used to reveal the charge-discharge mechanisms of this material. In the 2.5–4.5 V voltage range, Fe(III)/Fe(II) and Mn(III)/Mn(II) redox reactions occurred based on the reversible Li extraction/insertion from/into the $Li_{1.2}MnFe_{1.2}F_{6.8}/Li_{1.2-x}MnFe_{1.2}F_{6.8}$ and partial conversion reaction forming LiF, rutile FeF_2, and rutile MnF_2. Deep discharge to 2.0 V involved a full conversion reaction to LiF and metallic Fe and Mn.

In Chapter 5, trirutile-derived FeF_3 prepared through electrochemical delithiation of trirutile $LiFe_2F_6$ was examined for SIBs at 90 °C to shed light on the structural

evolutions occurring during sodiation-desodiation for the first time. The synchrotron XRD followed by Rietveld refinement revealed that the reversible topotactic 0.2 Na^+ extraction/insertion proceeded through a two-phase reaction between tetragonal Na_xFeF_3 and tetragonal FeF_3 during cycling in 2.6−4.0 V. In a lower cutoff voltage of 2.3−4.0 V, the consecutive cycle partially induced a new phase transformation between the orthorhombic $NaFeF_3$ and the cubic FeF_3, where the topotactic Na^+ extraction/insertion in the tetragonal structure also remained.

In Chapter 6, the details about phase transformation of the orthorhombic $NaFeF_3$ was investigated with IL electrolyte at 90 °C. The reduced particle size, carbon coating and elevated operating temperature were confirmed to be the prerequisite condition for full utilization of orthorhombic $NaFeF_3$. The GITT and synchrotron XRD measurements revealed a multi-phase transformation and the existence of an intermediate phase of the orthorhombic $Na_{0.5}FeF_3$ during the Na^+ extraction/insertion process. Further investigation on the electrochemical properties of the orthorhombic $NaFeF_3$ exhibited long-term cycle stability up to 400 cycles.

In this study, iron fluoride-based positive electrode materials were confirmed to be good candidates for LIBs and SIBs to expand the information space of the reaction mechanisms in the Li−Fe−F and Na−Fe−F systems. In the Li case, the Li^+ insertion/extraction at a higher cut-off voltage and the conversion reaction at a lower cut-off voltage reveal an underlying principle that may serve as a reference model for a wider range of isomorphic iron fluoride-based compounds. In the Na case, the formation of

tetragonal Na_xFeF_3 ($x \sim 0.2$) and orthorhombic $NaFeF_3$ at the discharged state, instead of the conversion reaction to NaF and FeF_2, demonstrates that the electrochemical responses of the Na system are different from that of the Li system. These results will inspire researchers to explore the electrochemical behavior of iron fluoride-based materials for potassium ion batteries. In addition, their high operating voltages and high electrochemical activities at elevated temperatures imply the feasibility of iron fluoride-based positive electrode materials for high-energy-density applications in near future, and the prospect of the ILs as electrolytes for large-scale applications in a wide temperature range.

List of Publications

Chapter 3

Yayun Zheng, Shinya Tawa, Jinkwang Hwang, Yuki Orikasa, Kazuhiko Matsumoto, Rika Hagiwara

Chemistry of Materials, 33 (2021) 868-880.

"Phase Evolution of Trirutile $Li_{0.5}FeF_3$ for Lithium-Ion Batteries"

Chapter 4

Yayun Zheng, Jinkwang Hwang, Kazuhiko Matsumoto, Rika Hagiwara

Electrochimica Acta, 405 (2022) 139627.

"Charge-discharge Properties and Reaction Mechanism of Cation-disordered Rutile-type $Li_{1.2}MnFe_{1.2}F_{6.8}$"

Chapter 5

Yayun Zheng, Jinkwang Hwang, Kazuhiko Matsumoto, Rika Hagiwara

ACS Applied Energy Materials, in press (DOI: 10.1021/acsaem.1c03756).

"Electrochemical and Structural Behavior of Trirutile-derived FeF_3 during Sodiation and Desodiation"

Chapter 6

Yayun Zheng, Shunta Jitto, Jinkwang Hwang, Kazuhiko Matsumoto, Rika Hagiwara

Journal of Power Sources, under review.

"Multi-phase Transformation of $NaFeF_3$ During Desodiation and Sodiation"

Acknowledgements

First of all, I take this opportunity to express my sincere gratitude to my supervisor, Professor Rika Hagiwara, who gave me the opportunity to carry out my Ph.D. at Kyoto University. His guidance and support allowed me to conduct my work in the best conditions. My wholehearted thanks also go to Associate Professor Kazuhiko Matsumoto. His enlightening instructions, fruitful discussions, and rigorous revisions promoted this thesis and all related papers to their present heights. My warmest thanks go to Assistant Professor Jinkwang Hwang. His valuable comments, insights, and enthusiasm for research deeply shaped my work and me. My heartfelt thanks go to Professor Yuki Orikasa for XAFS measurement and valuable comments on the paper.

I would like to convey my thanks to everyone in Hagiwara Lab. Special thank to Mr. Shinya Tawa for teaching me battery experiments, to Dr. Shubham Kaushik for helping me solve a lot of problems, to Ms. Naoko Sakamoto for her various help and care, to Ms. Shaoning Zhang for her companionship and care. I would also like to thank other group members Mr. Di Wang, Mr. Shunta Jitto, Mr. Jingyuan Zhang, and Ms. Nana Matsumoto who I met along the way.

I would like to thank the supporter in my life. My sincere thank goes to China Scholarship Council for the financial support. Many thanks to my friends Yayun Yang and Yuqian Lin for every happy time. Finally, I would like to express my thanks to my family, my father Guangchen Zheng, my mother Cuimei Dang, my sister Caiyun Zheng,

my brother-in-law Xudong Zhao, and my niece Yuqing Zhao, who encouraged me, understood me, and supported me with unconditional love all along this period of my life.

Studying and living in Japan were huge challenges for me. Fortunately, I met so many kind people who made my stay very enjoyable. Not all acknowledgments are described here. I am sincerely thankful to all those who are related to this study.

Yayun Zheng

March 2022